Magnetically Suspended Reaction Sphere with One-axis Hysteresis Drive

by

Lei Zhou

B.S., Tsinghua University (2012)

Submitted to the Department of Mechanical Engineering
in partial fulfillment of the requirements for the degree of

Master of Science in Mechanical Engineering

at the

MASSACHUSETTS INSTITUTE OF TECHNOLOGY

June 2014

Author .....
Department of Mechanical Engineering
May 9, 2014

Certified by .....
David L. Trumper
Professor of Mechanical Engineering
Thesis Supervisor

Accepted by .....
David E. Hardt
Chairman, Department Committee on Graduate Thesis

Magnetically Suspended Reaction Sphere with One-axis Hysteresis Drive

by

Lei Zhou

Submitted to the Department of Mechanical Engineering
on May 9, 2014, in partial fulfillment of the
requirements for the degree of
Master of Science in Mechanical Engineering

Abstract

This thesis presents the design, modeling, implementation, and control of a magnetically suspended reaction sphere with one-axis hysteresis drive (1D-MSRS). The goal of this project is two fold: (a) exploring the design for a reaction sphere in 3D for spacecraft's attitude control, and (b) studying the performance of the hysteresis motor in reaction wheel applications.

The 1D-MSRS is a motor with a spherical rotor with its rotor magnetically suspended in all translational directions, and is driven about the vertical axis by hysteresis drive. The magnetic suspension of the sphere is realized by arranging one electromagnet on top of the sphere, and a bearingless motor on the equator of the sphere. In this thesis, a complete mathematical model for the sphere's magnetic suspension, in both vertical and lateral directions, is derived. There is a good match between the calculated and measured system dynamics, which verified our modeling. The feedback control for the sphere's magnetic suspension in all translation degrees of freedom are studied in this thesis as well.

The hysteresis drive is chosen for the 1D-MSRS because its advantages of simple structure, moderate self-starting toque, and vibration-free operation. The hysteresis motor in 1D-MSRS consists of a conventional stator arranged on the sphere's equator and a spherical rotor of magnetically hard steel. In this thesis, an equivalent circuit model of the hysteresis motor based on an elliptical hysteresis model is used to analyze the motor's dynamic behavior. Good agreement between computed and measured sphere speed data validated the motor model. Experimental data shows that a starting torque of 8.15 mNm is achieved at 0.7 A peak excitation current. Under this excitation, the sphere arrives synchronous speed of 1,800 rpm within 6 s. The sphere can reach 12,000 rpm in lab, with the existence of air drag.

In order to suppress the hunting dynamics of the hysteresis motor, a feedback control loop on the sphere's rotational speed is implemented on the 1D-MSRS. A control scheme is designed for this nonlinear system, and its effectiveness is validated by both simulation and experiment. Through this speed feedback control, the 1D-MSRS can reach a minimum speed rise time while satisfying the constraints on its

excitation amplitude, showing lower power consumption during steady state, and the hunting dynamics of the motor are effectively suppressed. As a result, when the motor is operating in steady state with a speed of 1,800 rpm, the power consumption of the 1D-MSRS hardware is 3.44 W.

In this thesis, we also explored the design concepts for a magnetically suspended reaction sphere in 3D. A study of 3D spherical motors are presented in this thesis. We also demonstrated our understanding on the driving principle selection for spherical motors, and presented several magnetic design concepts for a 3D spherical motor design.

Thesis Supervisor: David L. Trumper
Title: Professor of Mechanical Engineering

Acknowledgments

First I would like to express my greatest appreciation to Professor David L. Trumper for his guidance, encouragement, and help to me. He gave me this chance to work in the Precision Motion Control Lab, introduced me into the fascinating field of mechatronics, and helped me to build up the knowledge and experimental skills. He is a great researcher and teacher, always patient, caring and enthusiastic. With his intelligence, enthusiasm and love for teaching, he has set a good example for me to learn from. I am so thankful for all his help and guidance, and am very happy that I can continue to learn from him in the following years during my PhD studies.

I would also like to thank Dr. Mohammad Imani Nejad. He helped me with almost everything on my research project, and this thesis will not be possible without him. He introduced me to the hysteresis motors, patiently explained his thesis to me, helped me set up the experimental bench, and helped me with everything in building the system. His energy and knowledge is always an inspiration to me. He is also a great friend, always patient and shares his experience with me.

During this two years study at MIT, many professors have offered me great help. I would like to thank Professor Markus Zahn who taught me important concepts in electromagnetism, which helped me to establish the foundation for my thesis work. I appreciate Professor Neville Hogan and Professor Jean-Jacque Slotine very much. They have not only taught me very important knowledge for research, but also offered me many inspiring ideas through discussions.

I would like to thank MIT Lincoln Laboratory for their collaboration and financial support. I would like to thank Andrew Stimac and Frederick Knight for their valuable input on the project.

My dear labmates created a very friendly atmosphere in our lab and offered me their help. Darya Amin Shahidi was my instructor in 2.737, and I also got a chance to learn more about building mechatronic systems by helping him in setting up the labs. He is always ready to answer my questions patiently. I enjoyed working with Minkyun Noh and Joseph Church together as teaching assistants for 2.14/2.140. Discussing

with them helped a lot in enhancing my understanding of the materials. Zhen Sun is a great friend in our lab, and offered me valuable suggestions on my research. Ian MacKenzie and Jun young Yoon are great labmates and always kind and patient to all my questions.

I would also like to thank Laura Zaganjori for her efficient and helpful administrative support. I would also like to thank the mechanical department office staffs, especially Leslie Regan.

I would thank my dear roommates Qifang Bao, Di Wu and Yi Huang, with whom I shared all my joy and disappointment, and shared many important moments in life. They have made my life a lot more interesting and enjoyable.

I am so thankful to my parents for their boundless support and love throughout my life and up until now. It was under their influence that I decided to study engineering. Being a single child in my family, I understand how they have missed me when we live on the two ends of the earth. I am really indebted to them for cannot accompany them around. I am also very thankful to Xiangyao Yu, my husband. His enthusiasm has always inspired me. He is a great friend and has helped me in every step of my way. I thank him for being extremely patient, supportive and understanding.

This work was supported by MIT Lincoln Laboratory via Advanced Concept Committee.

Contents

List of Figures

List of Tables

Chapter 1

Introduction

1.1 Motivation

In a spacecraft's flight control, the Attitude and Orbit Control System (AOCS) of the spacecraft is responsible for the high precision of control in orbit. When the spacecraft is maneuvering, it requires an external force, or torque, which is often provided by thrusters. As an alternative for torque inputs, a minimum of three reaction wheels (often 4-5 wheels are used for optimization and redundancy [1]) can be used. By accelerating the appropriate wheels, the system can produce a zero-mean torque about any axis to the spacecraft without the consumption of precious fuel, and momentum can be stored as well [2]. Such wheels are often used for both spacecraft attitude control [3] and large angle slewing maneuvers [4]. Other applications include vibration compensation and orientation control of solar arrays [5], as well as energy storage.

As an alternative to a combination of several reaction wheels, in this project we propose to use a magnetically levitated reaction sphere (MSRS) for small satellite attitude control. Our vision is that the sphere can be angularly accelerated about any axis by a three dimensional (3D) spherical motor, making the attitude of the spacecraft in all axes controllable by a single device.

A MSRS is attractive for its many obvious advantages. Due to its symmetry, a sphere always gives the same inertia, independent of its rotational axis. Also, because

only one rotor (although spherical) is appearing in this attitude control actuator, we envision that using a reaction sphere can yield a smaller total size and mass compared with using three reaction wheels. Also, magnetic suspension can eliminate imbalance, therefore the vibrations emitted by the reaction wheel that degrade the performance of precision instruments in space are reduced. Mechanical friction is also eliminated by the magnetic bearing, and thus low steady-state power consumption may be possible. This also enables the suspension to operate without lubrication and can be expected to have a longer maintenance-free lifespan. Furthermore, the rotation of a sphere has no gyroscopic coupling between the rotations about the three axes, which potentially enables simpler control possibilities.

Among many motor driving principles, the hysteresis motor is receiving increasing attention due to its advantages of simple structure, vibration-free operation, self-starting and constant torque production in starting. Another distinct feature of this motor is that its rotor can be made out of a single piece of hard and strong steel, which allows the rotor to stand large stresses and makes this motor concept attractive for high-speed applications. In the PhD thesis by Dr. Imani Nejad [6], several hysteresis motors of different scales are designed, built, and tested, and the results make us believe that this kind of motor concept may demonstrate good performance in reaction wheels.

To the best of our knowledge, the hysteresis motor has not been introduced to the development of reaction wheels until now. To our understanding, this is mainly due to the relatively low torque generation ability, nonlinearity in torque production and its speed hunting behavior. According to our studies, there is no reported evaluation of hysteresis motor's performance on reaction wheels yet.

Aiming at the dual goal of exploring the design for a magnetically suspended reaction sphere and evaluating hysteresis motor performance for reaction wheels application, we decide to focus this project on the development of a magnetically suspended reaction sphere with one-axis hysteresis drive (1D-MSRS). The hardware demonstrates a motor with a spherical rotor driven by hysteresis motor, and is magnetically suspended in all translation directions.

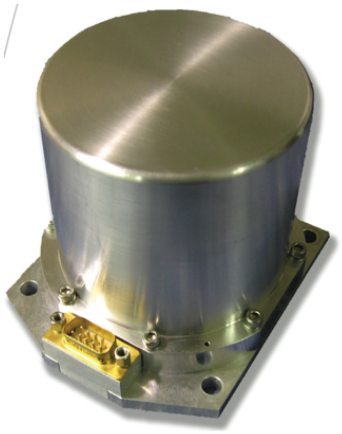

Figure 1-1: MicroWheel 200 (MW200) Reaction Wheel from Microsat Systems Canada Inc. Figure taken from [7]

Table 1.1: Specifications for MicroWheel 200 (MW200) Reaction Wheel from Microsat Systems Canada Inc.

Size	$100 \times 90 \times 90$ mm
Mass	1.0 kg
Imbalance	Static: $< 0.2mg.m$ Dynamic: $< 0.03mg.m^2$
Torque capacity	30 mNm
Angular momentum capacity	0.18 Nms
Power consumption	0 RPM: 3.0 W; Average: 7 W

In order to evaluate the performance of hysteresis motors for reaction wheels, a baseline that demonstrates the target specifications is needed. Since our goal is to design a reaction sphere for small satellite applications, a commercial reaction wheel assembly for typical small satellites is chosen as a benchmark. Figure 1-1 shows a MicroWheel 200 (MW200) Reaction Wheel from Microsat Systems Canada Inc. This is a commercially available reaction wheel that has flown in more than 10 satellites since 2001 [7]. Table 1.1 shows the specifications for a single MW200 reaction wheel. At the end of this thesis, we would like to demonstrate a comparison in performance between this reaction wheel and the 1D-MSRS that we developed.

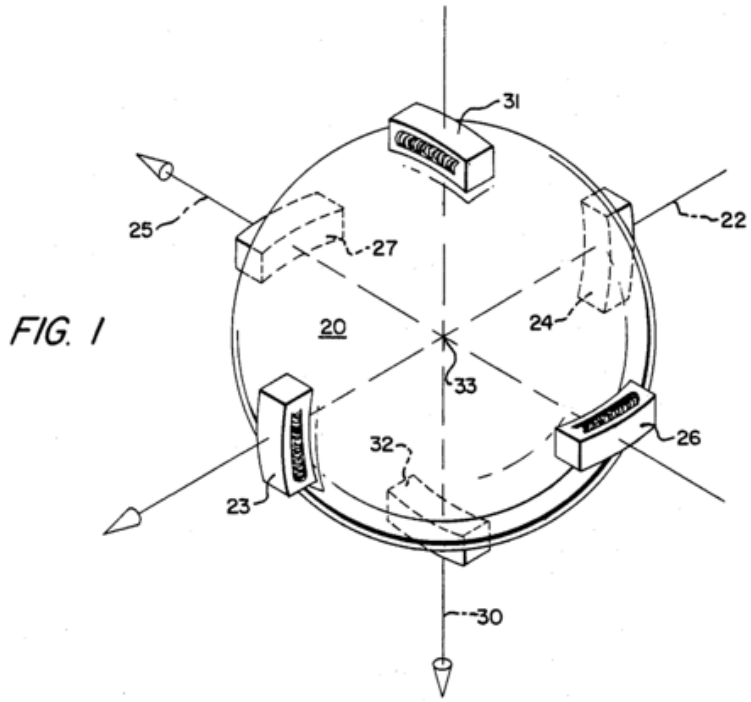

Figure 1-2: Reaction sphere design concept shown in patent from Honeywell Inc., taken from [8].

In the next section, a study of prior works in the design and development of reaction spheres are presented. More literature reviews on general spherical motor design for other applications are presented in Chapter 7.

1.2 Prior art in reaction spheres

The idea of a reaction sphere was proposed more than two decades ago by Honeywell Inc. in reference [8]. Figure 1-2 shows the design in this patent. However, in this design the stator segments are only covering a very small portion of the rotor's surface area, which reduces the system's efficiency. Other major challenges for building such a spherical actuator include (a) sensing of the angular position/velocity of the rotor sphere without adding additional inertia or friction, and (b) field coupling between the motor and bearing functions. There is no report on development and performance of such a reaction sphere design.

Several spherical motors for other applications have been developed [9] [10] [11]

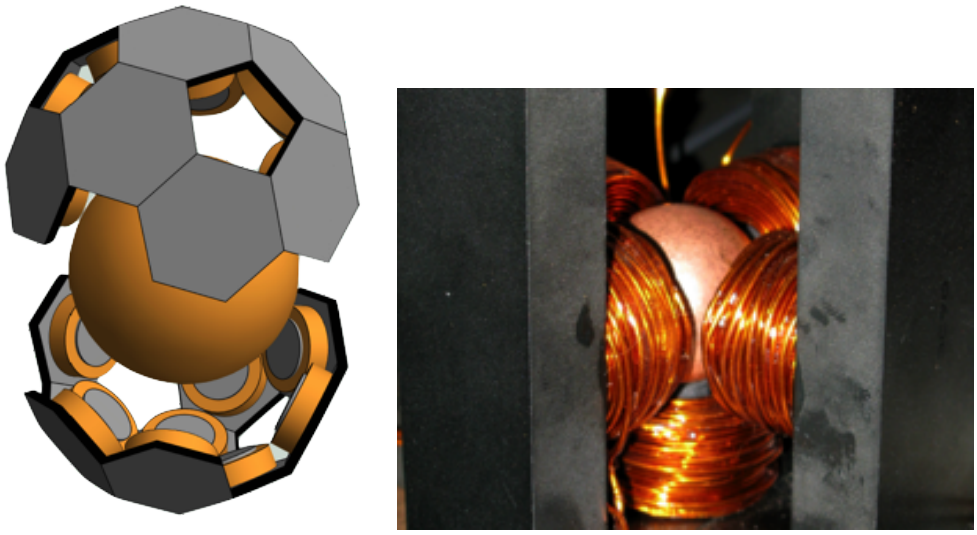

(a) Design concept. (b) Prototype.

Figure 1-3: The induction type reaction sphere design by Noqsi Aerospace, Ltd. Figure taken from [13].

[12]. More details about these spherical motor designs are presented in Chapter 7. Although these designs cannot directly be used for an all degree-of-freedom actuator for attitude control, they still lays a good foundation for the exploration of 3D spherical motor design for reaction sphere application.

One induction drive based reaction sphere assisted with magnetic bearings is proposed by Noqsi Aerospace, Ltd. in [13]. However, the development of such a reaction sphere hardware is not reported. Figure 1-3 shows the design concept and its initial prototype.

Another reaction sphere design, also magnetically suspended, is the ESA reaction sphere that is presented in [14]. This is a permanent-magnet-motor-based reaction sphere, as is shown in Figure 1-4. The performance of this sphere is also reported in reference [14]: with a reaction sphere mass of 14.1 kg spinning at 6000 rpm, a torque of 0.2 N.m and an angular momentum of 23 Nms is achieved. This design successfully solved the problem of sphere's angular position sensing and the coupling between bearing and motor functions, which makes it a good actuator about all axes. But the complexity of its magnetic structure may prevent it from being suitable for small satellites application, and the strength of the rotor with glued on magnets limits

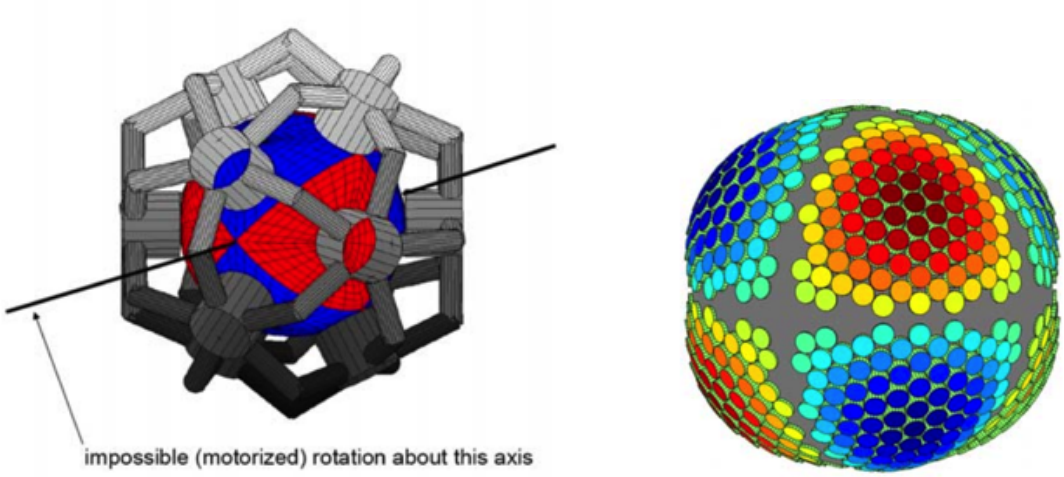

(a)Stator design. (b) Rotor design.

Figure 1-4: Reaction sphere designed presented by Onillon et al. Figure taken from [14].

its maximum rotational speed, which may limit the performance of the actuator.

Despite its promising performance and many attempts, to the best of our knowledge, there is no ready-for-commercialization technology developed for such a reaction sphere. As mentioned before, to our understanding, this is mainly due to the difficulties of 3D angular position/velocity sensing for spherical rotor, the complexity due to coupling of fields by stator segments and between bearing and motor functions, and the challenge in magnetic design to reach a good efficiency and torque ability.

1.3 Thesis overview

This thesis takes initial steps to study the performance of a high-speed magnetically suspended reaction sphere (MSRS) for small satellites application. At the same time, this project also evaluates the performance of hysteresis motors for this application. The major efforts and a summery of key results in this thesis are briefly presented in this section.

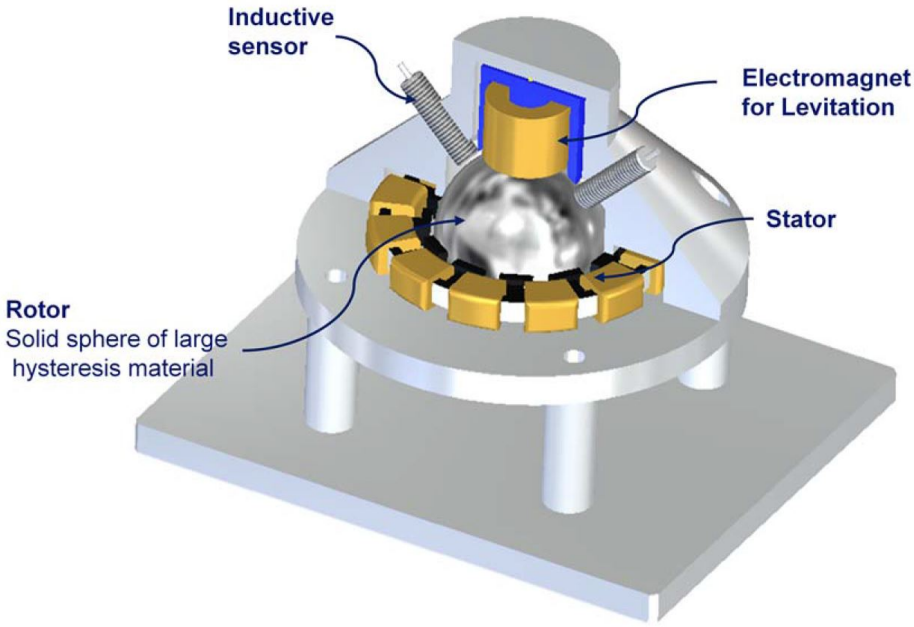

Figure 1-5: CAD design of 1D-MSRS.

1.3.1 1D-MSRS design, development and testing

We designed, built and tested a magnetically suspended reaction sphere with one-axis hysteresis drive (1D-MSRS), which is a one-axis demonstration of the reaction sphere to test the performance of hysteresis motor's performance.

Figure 1-5 shows the CAD design of 1D-MSRS. The rotor is a 54 mm diameter sphere of hardened D2 steel. Four induction position sensors are placed around the rotor to measure the sphere's position in three translational degrees of freedom. The sensors are arranged 45^o from the vertical axis and are separate by 90^o in the azimuthal coordinate. The rotor sphere is magnetically levitated in the vertical direction by a reluctance actuator placed at the north pole. The stator is arranged around the sphere's equator line, and serves both for levitating the sphere in the horizontal plane and for generating torque about vertical-axis simultaneously with a bearingless motor configuration. A reflective optical tachometer is used for speed detection of the reaction sphere. A photograph of the device is presented in Figure 1-6.

For the motor operation of the 1D-MSRS, the magnetic hysteresis of the rotor material is used for torque production. In the design of 1D-MSRS, D2 steel is selected for

(a) (b)

Figure 1-6: Photograph of 1D-MSRS.
(a) Structure; (b) stator and rotor.

the rotor. D2 steel is a high carbon, high chromium type tool steel. Figure 1-7 shows the B-H curve measured by Dr. Mohammad Imani-Negad under different excitation frequencies, and the original data and its measuring procedures are presented in [6].

The stator for the 1D-MSRS is a custom-made stator with 24 slots and a height of 9.50 mm, which is made by stacking 12 layers of motor stator laminations cut from AWG 24 non-oriented electrical steel. Since the stator needs to work as a magnetic bearing and motor stator simultaneously, the multiple winding approach of a bearingless motor is used, with its 4-pole winding being used for rotation and 2-pole winding for sphere's lateral suspension. Figure 1-8 shows a diagram of the winding pattern for 1D-MSRS, and Figure 1-9 shows the picture of the stator for the 1D-MSRS, where (a) shows the stator laminations without winding, and (b) shows the wound stator.

We integrated the 1D-MSRS and tested the motor performances of the sphere. The sphere is magnetically suspended in all translational directions, and is spinning about the vertical axis as driven by the rotational stator magnetic field. Figure 1-

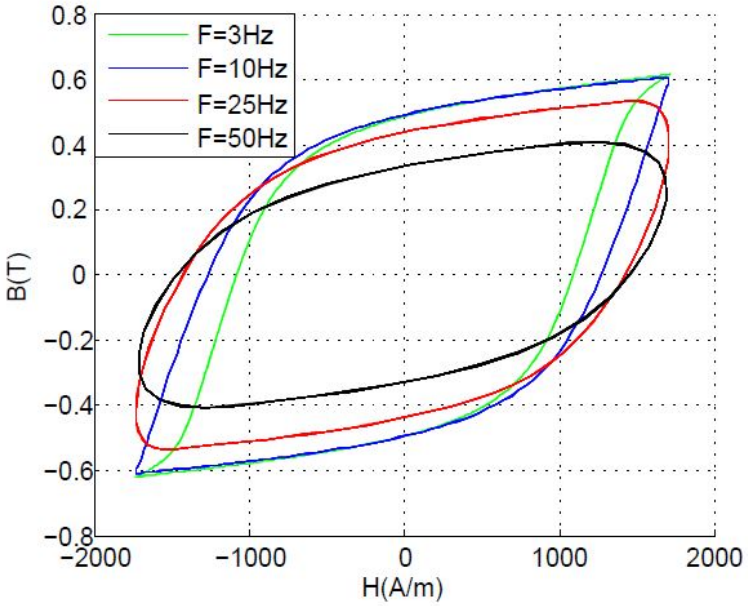

Figure 1-7: Measured B-H loop for D2 steel under different excitation measured by Dr. Imani Nejad. Figure taken from [6].

10 presents the acceleration curves of the 1D-MSRS under different amplitudes of excitation current. The data also shows that with an excitation current of 0.7 A zero-to-peak value, the sphere can reach the synchronous speed of 30 Hz (1800 rpm) within 6 seconds. The starting torque under this excitation is 8.15×10^{-3} Nm.

Speed feedback control is implemented to the 1D-MSRS system. Experiments shows that in steady state running a current amplitude of 0.2 A is required, which leads to a steady state power consumption of 3.44 W.

1.3.2 Single-DOF magnetic suspension modeling and control

In this thesis the working working principles and control of the of the 1D MSRS's vertical suspension are analyzed, which provides a building block for multi-degrees-of-freedom magnetic suspension system analysis. Figure 1-11 shows the picture of the sphere being magnetically suspended in the vertical direction.

In order to reduce the DC current in the actuator coil for sphere's weight compensation, a thin-disk shape permanent magnetic is placed in the magnetic path of

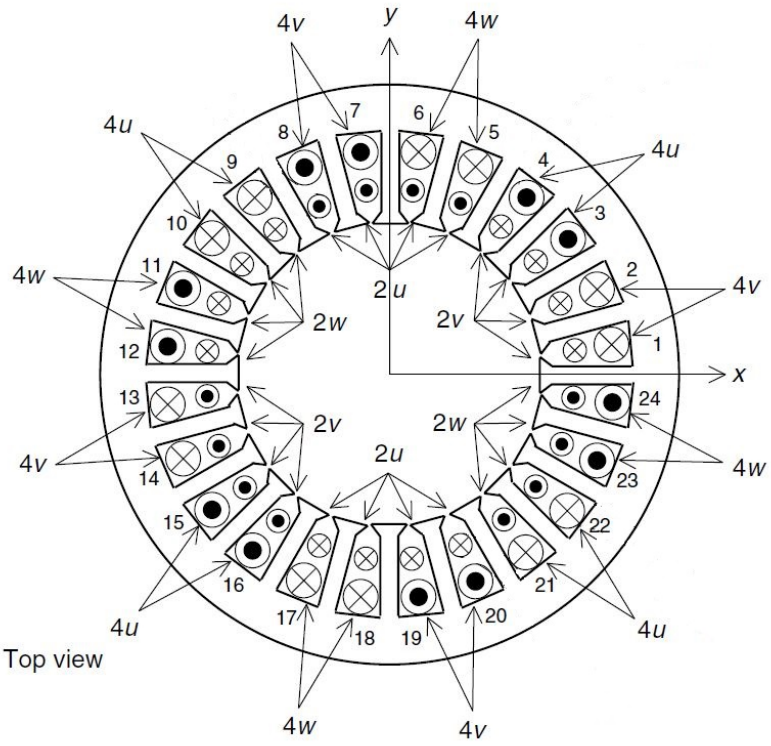

Figure 1-8: Multiple winding diagram for bearingless motor in 1D-MSRS. Winding 4u, 4v and 4w represents the 4-pole windings, and 2u, 2v and 2w represents the 2-pole windings. The two sets of windings are configured to be electrically orthogonal.

(a) (b)

Figure 1-9: Stator for the 1D-MSRS without and with winding.

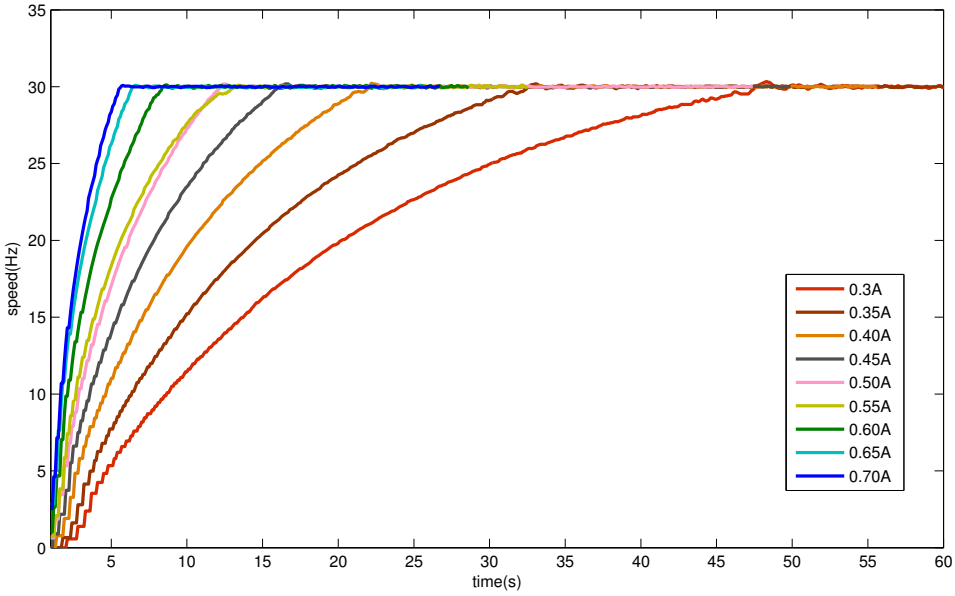

Figure 1-10: Acceleration curves of 1D MSRS under different excitation current amplitudes.

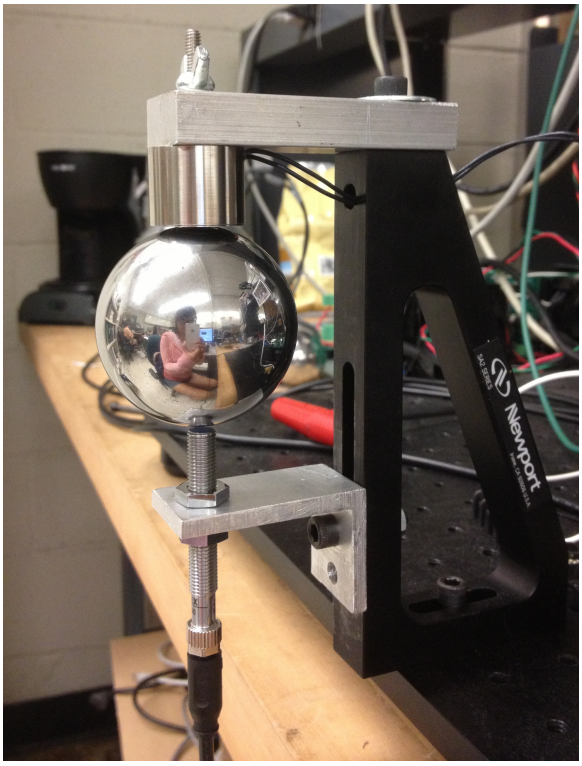

Figure 1-11: Single DOF levitation of sphere by reluctance actuator with permanent magnet.

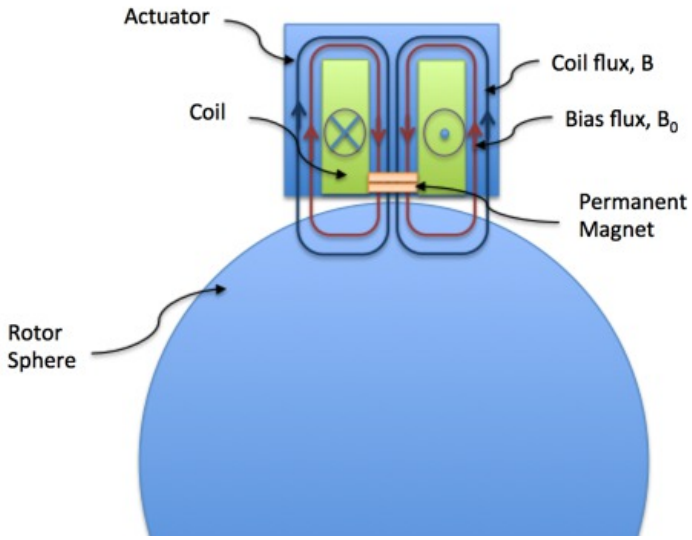

Figure 1-12: A cross section of the biased levitation actuation system

the suspension actuate system to add a bias DC flux. Figure 1-12 depicts the system for the sphere's vertical suspension. In this thesis we call the actuator a flux-biased electromagnet, recognizing the bias flus from the permanent magnet.

A complete mathematical model for this flux-biased magnetic suspension system is derived by means of the magnetic circuit method. The details of the derivation are presented in Chapter 3. A linearizion of the sphere's dynamic equation yields the transfer function from the coil current to sphere's vertical displacement. Figure 1-13 shows the Bode plot of the derived transfer function and the measured transfer function. The good match of the two Bode plots verified our derivation. Feedback control of the sphere's magnetic suspension is addressed using a loop-shaping point of view. For this control loop, a crossover frequency of 300 rad/s and a phase margin of 37^o are achieved.

1.3.3 Bearingless motor modeling and control

The lateral suspension of the sphere in 1D-MSRS is realized by means of a bearingless motor. The bearingless motor is implemented by arranging two sets of windings on a single stator. By correctly configuring and controlling the current in these windings,

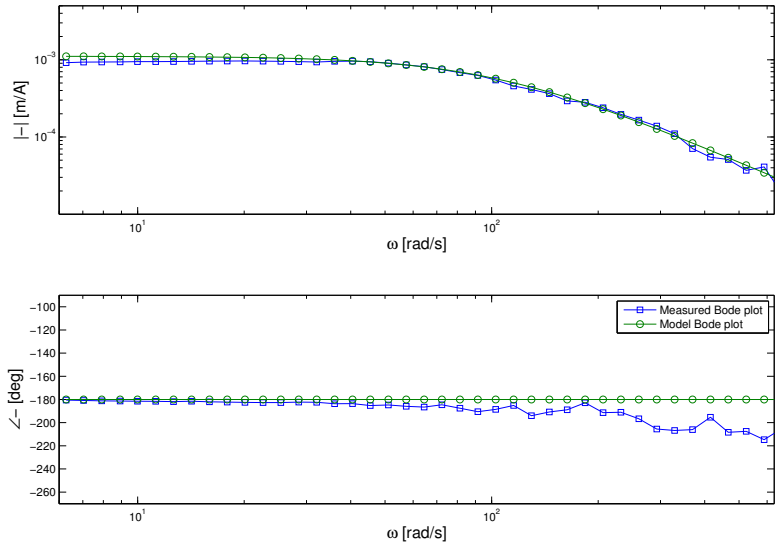

Figure 1-13: Bode plot of the sphere magnetic levitation system from coil current i to the sphere's vertical position output x. Blue: experimental measured data; green: model.

the machine can generate radial force for suspension as well as a rotational magnetic field for spinning with only one stator assembly.

One major contribution of this thesis is that we derived a complete dynamic model for the suspension function in a bearingless motor system. This model can be generalized for analysis of the bearing function for other electrical motors. The derived transfer function from the suspension winding current to the rotor's radial displacement is

$$\frac{X(s)}{I_{2a}(s)} = \frac{K_i}{ms^2 - K_s}. \tag{1.1}$$

Here the value of K_s and K_i are the negative stiffness [N/m] and the force constant [N/A] of the lateral suspension system respectively. They can be calculated by

$$K_s = \frac{2}{\pi}\frac{Rl\mu_0 N_4^2(\sqrt{3}/\sqrt{2}I_m)^2}{g_0^3}[N/m] \tag{1.2a}$$

$$K_i = \frac{\sqrt{3}}{\sqrt{2}}\frac{2\mu_0 RlN_2N_4}{\pi g_0^2}(\frac{\sqrt{3}}{\sqrt{2}}I_m)[N/A]. \tag{1.2b}$$

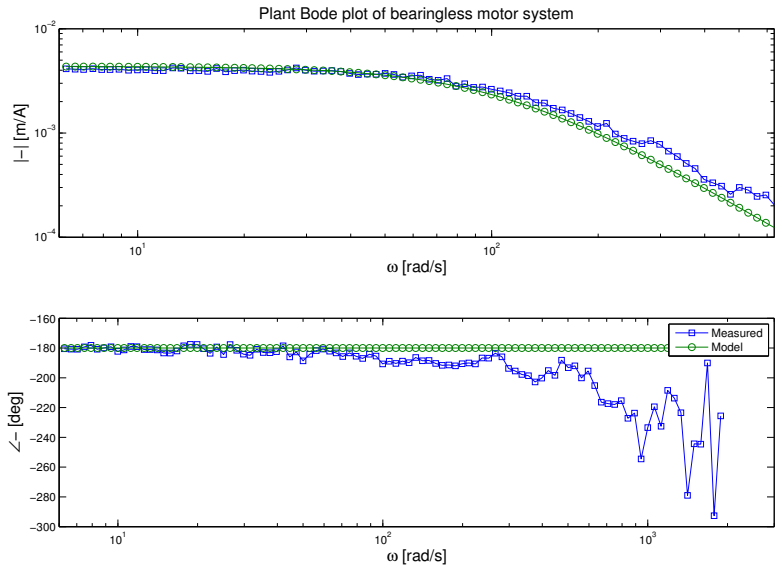

Figure 1-14: Measured and calculated frequency response of the lateral levitation system of 1D MSRS from the 2-pole winding current i_{2a} to the sphere's position in x-direction x. Green line: modeled plant transfer function. Blue: experimental measured plant transfer function. Three phase motor winding current zero-to-peak value is $I_m = 0.5$ A.

Here the value I_m is the zero-to-peak current amplitude of the 3-phase current in the 4-pole motor windings. The meaning of the nomenclatures and the detailed derivations of these results are presented in Chapter 4. Figure 1-14 shows the Bode plot of the derived transfer function for sphere's lateral suspension and a Bode plot that measured from 1D-MSRS. Good match between the two Bode plots verified the our derivation.

The plant dynamics of the sphere's lateral suspension is dependent on the excitation amplitude of the current in the motor winding, which requires us to adjust the controller accordingly. The detailed controller design is shown in Section 4.3. Figure 1-15 shows the measured plant Bode plot of the lateral suspension system under different motor winding excitation amplitudes, and Figure 1-16 gives the Bode plot of the corresponding loop return ratios.

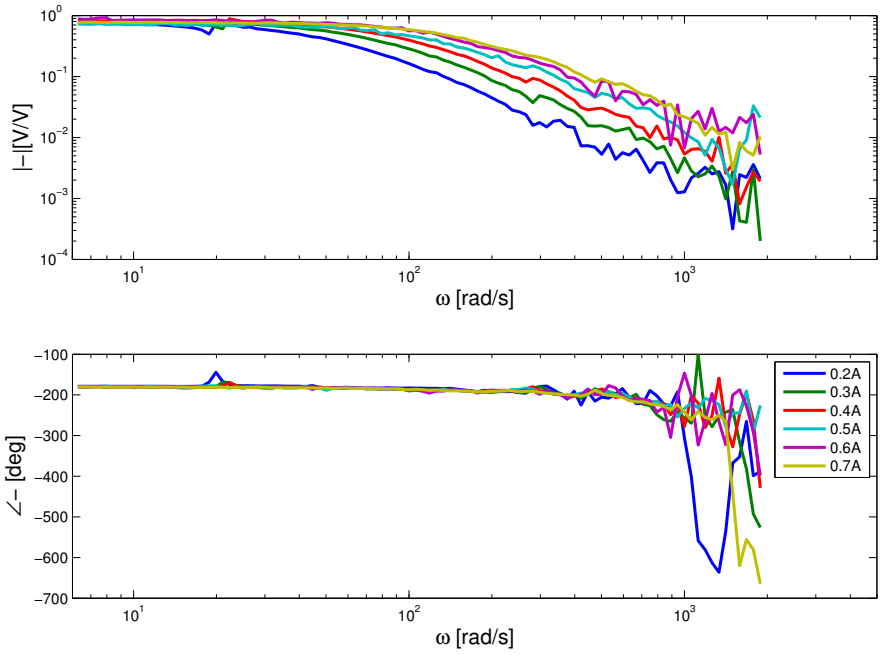

Figure 1-15: Experimentally measured plant frequency response for X direction sphere suspension with different 3-phase-4-pole excitation amplitude I_m (zero-to-peak).

1.3.4 Hysteresis motor modeling

In this thesis an equivalent circuit model for a hysteresis motor as introduced by Miyairi and Kataoka in [15] and later studied in [6] is used to analyze the motor dynamics of the reaction sphere. This motor equivalent circuit model is based on an elliptical approximation of the hysteresis loop. The values of the components in this equivalent circuit are dependent on the motor state. We use this model for steady-state analysis and extend its assumptions to use it to simulate the speed transients of the hysteresis motor. A detailed discussion and derivation of this model are presented in Chapter 5.

Simulation of the 1D-MSRS's motor operation is carried out based on this equivalent circuit model. Figure 1-17 shows the simulated and measured speed step response of the reaction sphere plotted together. Good agreement between the measured motor speed data and the simulation results verified the effectiveness of the simulation, despite violating the sinusoidal steady state assumption of the model.

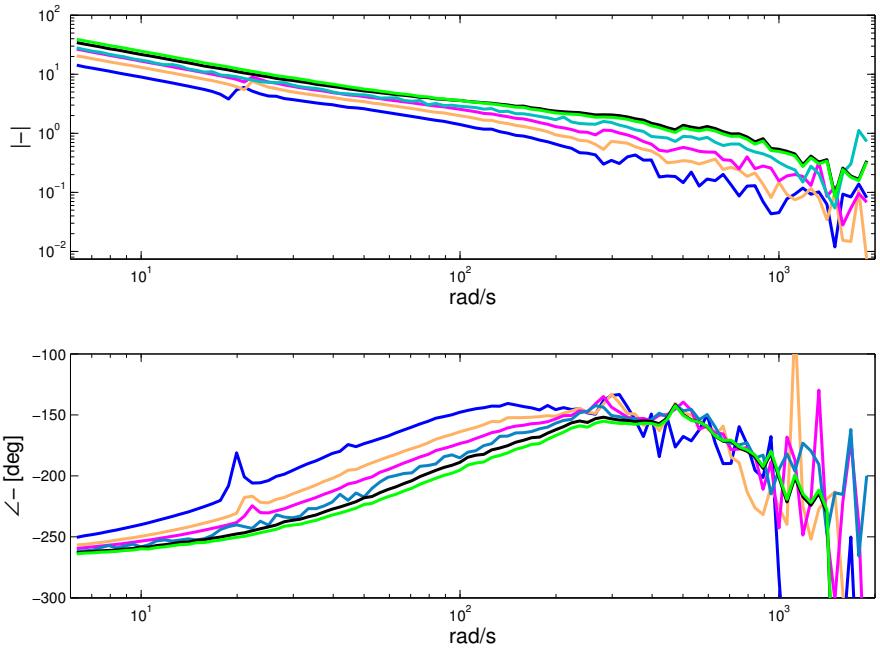

Figure 1-16: The measured Bode plots of loop-return-ratio of the lateral suspension control loop under different 3-phase-4-pole peak current amplitudes. Return ratio is unitless.

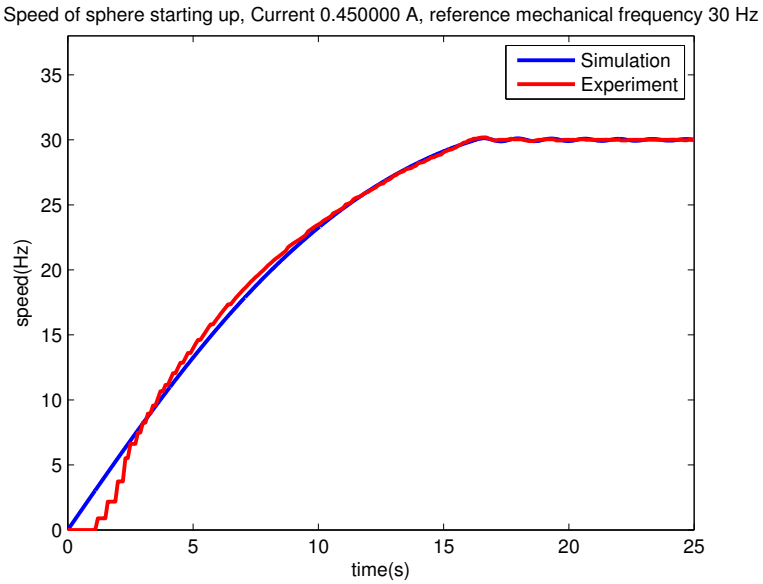

Figure 1-17: Starting angular velocity simulation and experiment speed data under zero-to-peak excitation current of 0.45A.

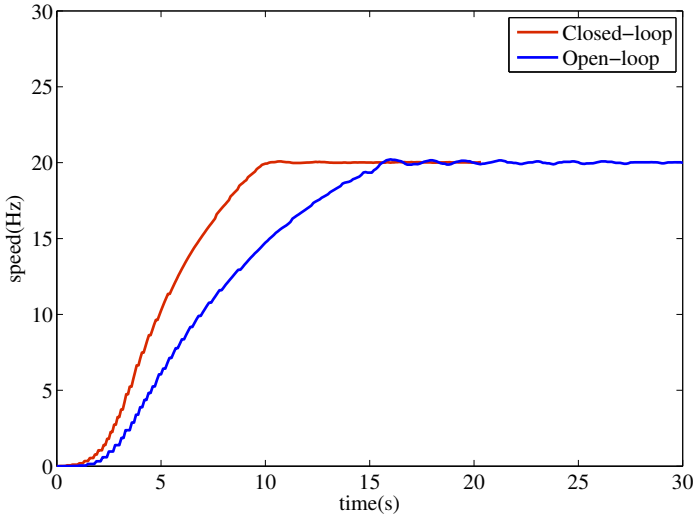

Figure 1-18: A comparison of experimental open-loop step response data and the closed-loop step response data of reaction sphere. The open-loop step response is measured under a peak current value of 0.4 A.

1.3.5 Speed control for hysteresis motor

Hysteresis motors can run asynchonously and generate full torque, and when the torque load drops, they operate as an synchronous motor. Therefore the motor speed will finally reach the reference speed when load torque is smaller than the maximum torque. However, when the motor speed is close to the reference speed, a speed oscillation about the desired synchronous frequency can occur. This motor dynamics is called hunting. It is undesirable when a hysteresis motor is used for the development of a reaction wheel or reaction sphere, as it will introduces vibrations into the spacecraft.

In this thesis, a feedback loop on the sphere's rotational speed is designed to suppress the motor hunting. This speed control also enables the sphere to accelerate with a minimum rise time, and helps reduce the drive current amplitude when the sphere's speed reaches the reference speed. In this control system, the speed signal is measured by an optical tachometer, and the control effort is the current amplitude that we supply to the motor windings. The control design is introduced in Chapter 6 in detail. Figure 1-18 shows the measured step response of the reaction sphere's

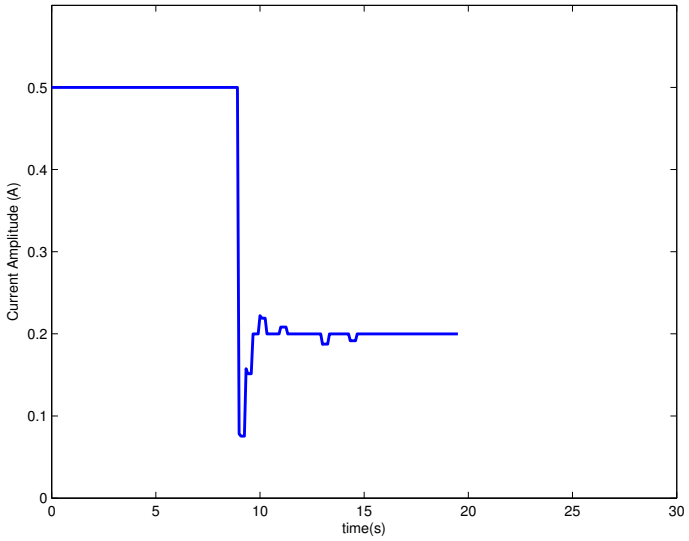

Figure 1-19: Experimental closed-loop control effort data (peak amplitude for motor current) of reaction sphere start up.

rotational speed under open-loop and closed-loop operations, respectively. Note the hunting speed ripple in the open-loop speed data (blue). Figure 1-19 shows the motor winding current peak amplitude measured when motor is operating in closed-loop. The speed control scheme can effectively suppress the hunting, enables faster acceleration, and also significantly reduces the motor current amplitude when the sphere is operating in steady-state.

1.3.6 Spherical motor design concepts

Although only a reaction sphere with one-axis motor drive is demonstrated in this thesis, we expanded our scope to the conceptual design of a 3-axis (3D) version by studying the possible motor driving principles and magnetic design concepts for spherical motors. Chapter 7 of this thesis presents a literature review on the design and development of spherical motors and some discussions about possible motor driving principles and magnetic design concepts for 3D spherical motors.

Chapter 2

Magnetically Suspended Reaction Sphere Design and Hardware Implementation

In this chapter the design and the hardware implementation of the magnetically suspended reaction sphere with one-axis hysteresis drive (1D-MSRS) are presented in detail.

2.1 System Overview

The 1D-MSRS is a motor with a magnetically levitated spherical rotor that can rotate and store momentum about the vertical axis. Figure 2-1 shows the CAD design of the 1D-MSRS. The rotor is a 54 mm diameter sphere of hardened D2 steel. Four inductive position sensors are placed around the rotor to measure the sphere's position in three translational degrees of freedom. The sensors are arranged 45^o from the vertical axis and are separated by 90^o in the angular coordinate. The rotor sphere is magnetically levitated in the vertical direction by a reluctance actuator placed at the north pole. The stator is arranged around the sphere's equator line, and serves both for levitating the sphere in the horizontal plane and for generating torque about z axis simultaneously by a bearingless motor configuration. A reflective

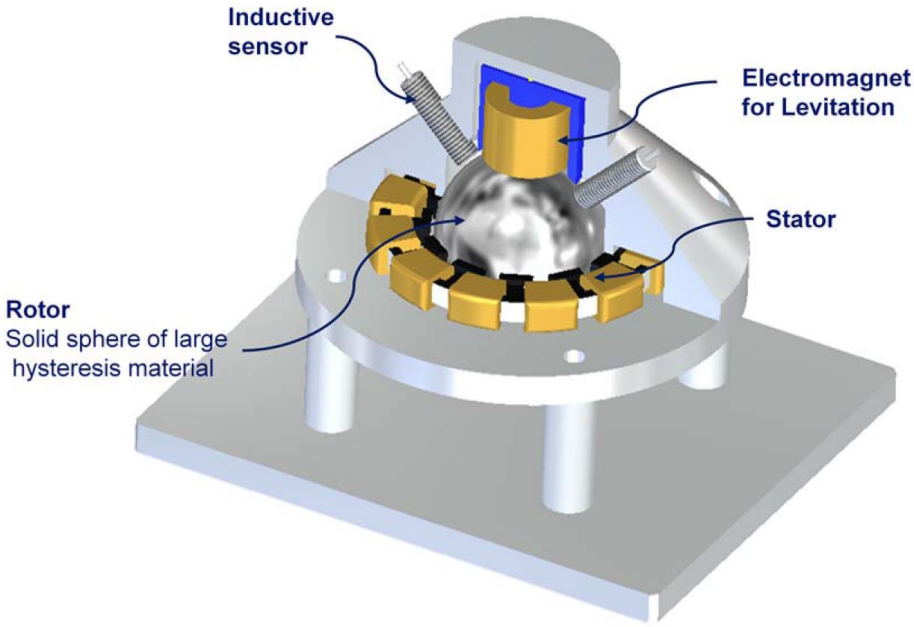

Figure 2-1: CAD design of 1D-MSRS.

optical tachometer is used for speed detection of the reaction sphere. The structure of the device is presented in Figure 2-2.

In the design of the magnetic suspension system in 1D-MSRS, the sphere's motion in the vertical direction and in the horizontal directions are considered to be independent. That is, the motion of the sphere in the vertical direction is solely controlled by the electromagnet above the sphere, while the lateral suspension of the sphere is only determined by the bearingless motor stator. To validate this approximation, finite element method (FEM) is used to find the field coupling between the field generated by the top electromagnet and the field generated by the stator. Figure 2-3 shows the magnetic field distribution in the rotor of 1D-MSRS calculated by 3D FEM. This result shows that the fields generated by the two sources are approximately decoupled. This calculation also shows that by selecting a suspension electromagnet of a smaller diameter can reduce the field coupling effect.

(a) (b)

Figure 2-2: Photograph of the 1D-MSRS.
(a) Structure; (b) stator and rotor.

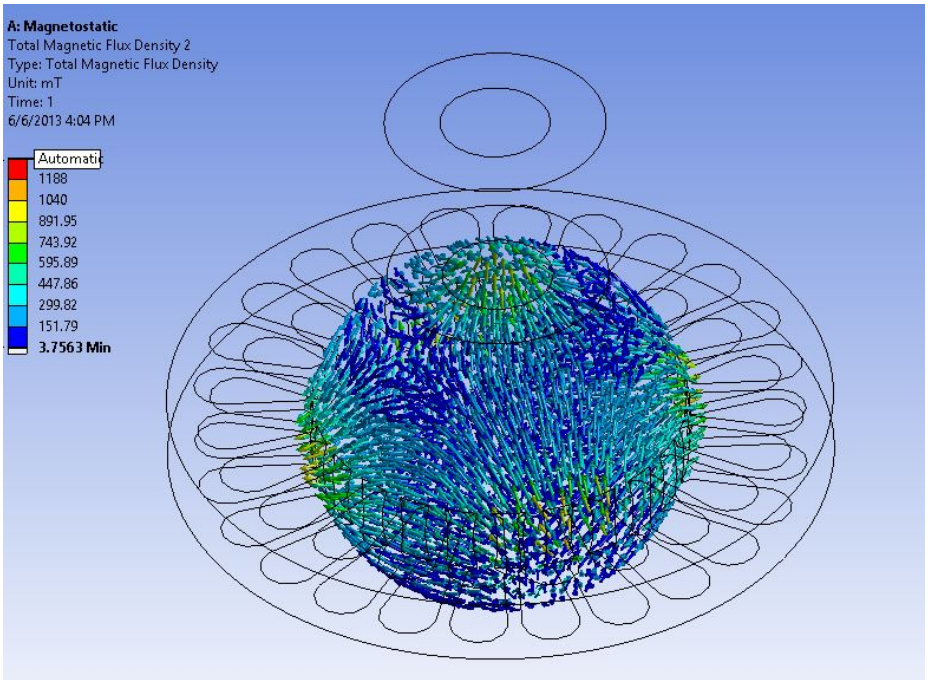

Figure 2-3: Field distribution in the rotor of 1D-MSRS calculated by 3D FEM.

Figure 2-4: Inductive sensors for sphere position sensing and their arrangement as 4 symmetrically locate probes.

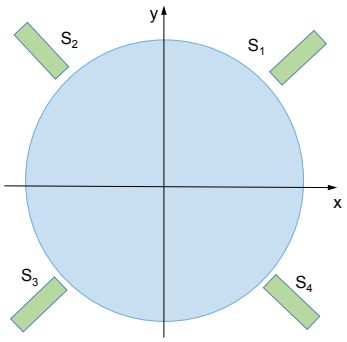

Figure 2-5: The sensor arrangement and coordinate definition.

2.2 Position Sensors

The spherical rotor's displacements in all three translational degrees of freedom are monitored by a redundant set of four position sensors, which are of induction type. The four sensors are arranged 45^o to the vertical axis, and pointing to the center of the sphere. In this configuration the translation of the sphere in 3 directions (two horizontal directions and one vertical direction, also x, y and z) are sensed and noise is mitigated by taking linear combinations of the signals. Figure 2-4 shows the 4 inductive sensors we used to measure the transverse position of the sphere.The range of the sensor is 0-4 mm. The gain of each sensor is 1.25 V/mm.

Figure 2-5 shows a top view figure of the sensor arrangement, and a Cartesian coordinate is defined as shown by the axes. The z axis is pointing out from the

paper. Let us number the four sensors in counter-clock wise direction. Based on the four displacement measurements s_1, s_2, s_3 and s_4, we use the following signals as the rotor's displacements measurements in three translational axes:

$$V_z = \frac{1}{4}(s_1 + s_2 + s_3 + s_4) \tag{2.1a}$$

$$V_x = (s_1 + s_4) - (s_2 + s_3) \tag{2.1b}$$

$$V_y = (s_1 + s_2) - (s_3 + s_4). \tag{2.1c}$$

As a result, the sensor gains in the vertical direction (z-axis) is 1.25 V/mm, while the equivalent sensor gains in the lateral direction (x- and y-axes) is $\sqrt{2} \times 1.25$ V/mm. These sensor gain values are used in the sphere displacement measurements in later chapters.

2.3 Rotor

Figure 2-6 shows the spherical rotor of the 1D-MSRS. The rotor is a 54 mm diameter solid sphere of magnetically hard material. According to the analysis of hysteresis motor torque, the torque is proportional to rotor material's hysteresis loop area [16]. Although materials with better hysteresis properties exists, we selected D2 steel for the rotor of 1D-MSRS for the proof of our design, as this material was readily available. D2 steel is a kind of high Carbon, high Chromium type tool steel. It contains 11 to 15 percent Chromium, which makes it a deep hardening, highly wear resistant and magnetically hard alloy. Figure 2-7 shows the B-H curve measured by Imani-Nejad [6] under different excitation frequencies (original data and its measuring procedures are presented in [6]). Notice that the loop widening effect with frequency can be recognized in the hysteresis data.

Figure 2-6: Rotor sphere for magnetic suspended reaction sphere prototyping.

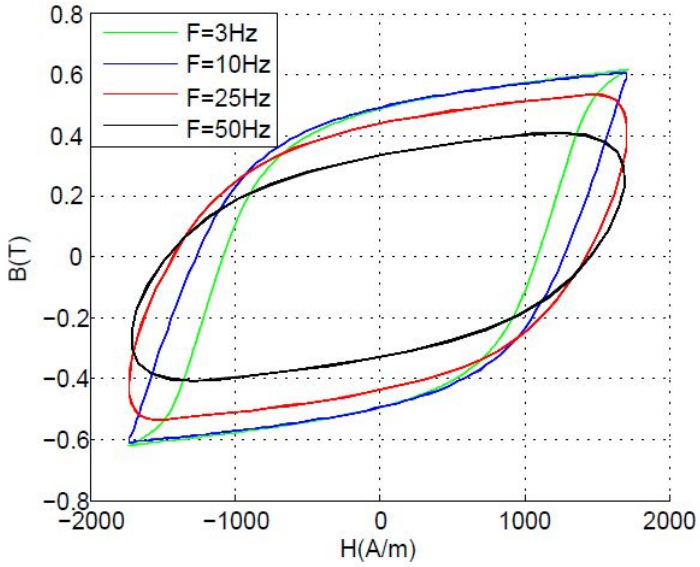

Figure 2-7: Measured B-H loop for D2 steel under different excitation. Measurement is taken by Dr. Imani Nejad. Original data and measurement process are shown in [6].

(a) (b)

Figure 2-8: Stator for the 1D-MSRS without and with winding.

2.4 Stator

The stator for the 1D-MSRS is a custom-made stator with 24 slots and a height of 9.50 mm, which is achieved by stacking 12 layers of motor stator laminations cut from AWG 24 non-oriented electrical steel. We cut the motor laminations from sheet material using a waterjet cutter. Since the stator needs to work as a magnetic bearing and motor stator simultaneously, the multiple winding approach of a bearingless motor is used, with its 4-pole winding for rotation and 2-pole winding for stabilization [17]. Figure 2-8 shows the stator for the reaction sphere, where (a) shows the stator laminations without winding, and (b) shows the wound stator.

2.5 Vertical levitation actuator

An electromagnet actuator is used for the position control of the reaction sphere in the vertical direction. Figure 2-10 shows the rotor sphere being levitated in the vertical direction by this actuator.

To make the system more energy efficient, a permanent magnet thin disk is embedded in the magnetic path of the levitation actuator. With this design, most of the weight is carried by the permanent magnet flux and the required excitation coil

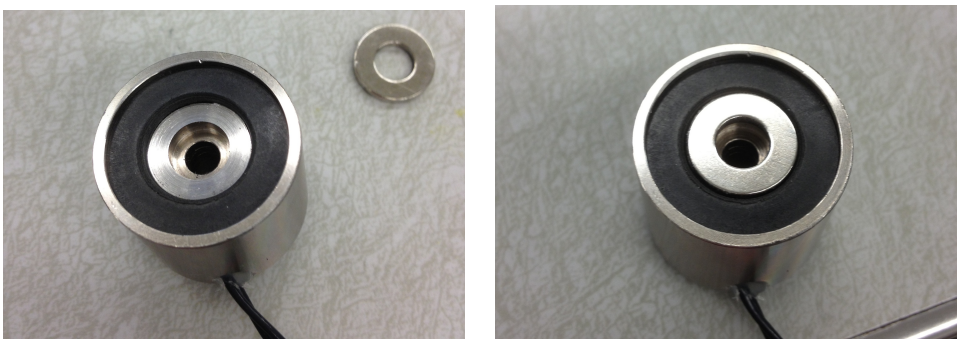

(a)Electromagnet and flux biasing permanent magnet.

(b) Levitating actuator assembly.

Figure 2-9: Electromagnet actuator for magnetic leviation.

current can be greatly reduced. Also, the nonlinearity of the operation characteristic is attenuated by the additional reluctance associated with the permanent magnet. However, these benefits are achieved by sacrificing the dynamic force capability of the coil due to the increased air gap [18].

2.6 Controller

The digital controller is selected as a high speed digital signal processing computer, with the capability of hardware real-time interrupt processing. In the development of the 1D-MSRS prototype, an NI PXI chassis with real-time controller is used and is running at a sampling and processing frequency of 10 kHz. Five A/D and seven D/A converter channels with 14 bits precision are used. The controller's functions are:

- Receive signals for displacement from inductive probes and motor rotational speed from tachometer;
- Receive control commands from the host computer to change parameters of the levitation and self-bearing motor system;
- Generate and send the current control signals for vertical suspension and for 4-pole/2-pole motor according to the control algorithms;
- Generate acceleration trajectory for the sphere's rotation;

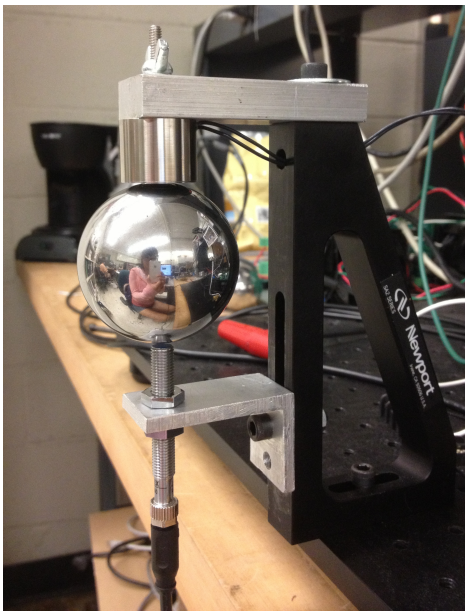

Figure 2-10: Single DOF levitation of sphere by reluctance actuator with permanent magnet.

- Diagnose the state of the elements of the self-bearing motor system and transmit messages to the host computer.

2.7 Power amplifier

In order to directly drive the current in the actuators for the reaction sphere, 7 separate relatively large bandwidth current control amplifiers are used. Though the driving efficiency of a linear amplifier is not as high as a switching amplifier, it can avoid generating high frequency switching waveforms, which can be a source of noise. For research and prototyping purposes we decided to use linear amplifiers to reach a better system performance. In the design of the 1D-MSRS, one current control amplifier is used for the sphere's levitation and its vertical position control, three amplifiers are used for the 4-pole-3-phase winding in the stator for motor driving, and three amplifiers are used for the 2-pole-3-phase winding for horizontal levitation control. Figure 2-11 shows a picture of the PCB of current control amplifier. These amplifiers were designed and built by Dr. Imani Nejad [6].

The current control power amplifier is built around a PA12 amplifier from APEX

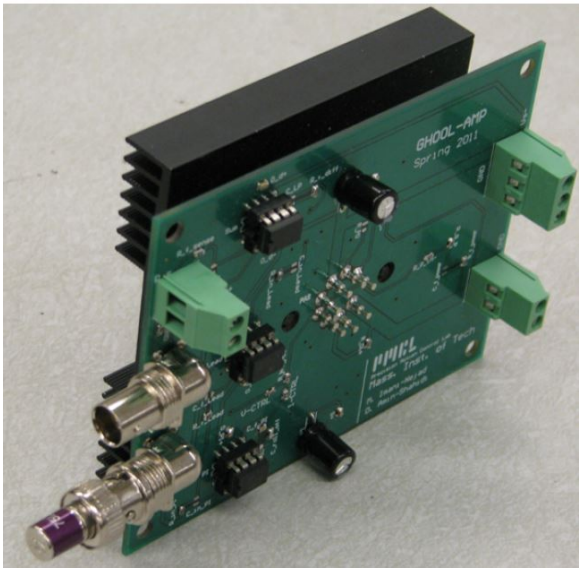

Figure 2-11: Current control amplifier for reaction sphere excitation. Figure taken from [6].

[19]. Usually the power amplifiers can be easily destroyed by inductive flyback effect. When the current changes in the inductor, a reverse voltage is being created. This flyback voltage can damage the power amplifiers. The PA12 we are using has a built-in flyback diode that protects the output from over-voltage due to the flyback effect.

The power amplifier is configured as unity gain. The current that passes through the load is converted to a representative voltage by a sense resistor value of 0.1Ω. This voltage is input to a differential amplifier with a gain of 100. A analog lead-lag controller is designed in the circuit to control the current loop. Figure 2-12 shows the circuit diagram for the current control amplifier. In this diagram, the left-most op-amp is configured as a differential amplifier for the input signal. The other two op-amps are used to implement a lead-lag controller. The design and specifications for the current control amplifiers are described in [6] in detail.

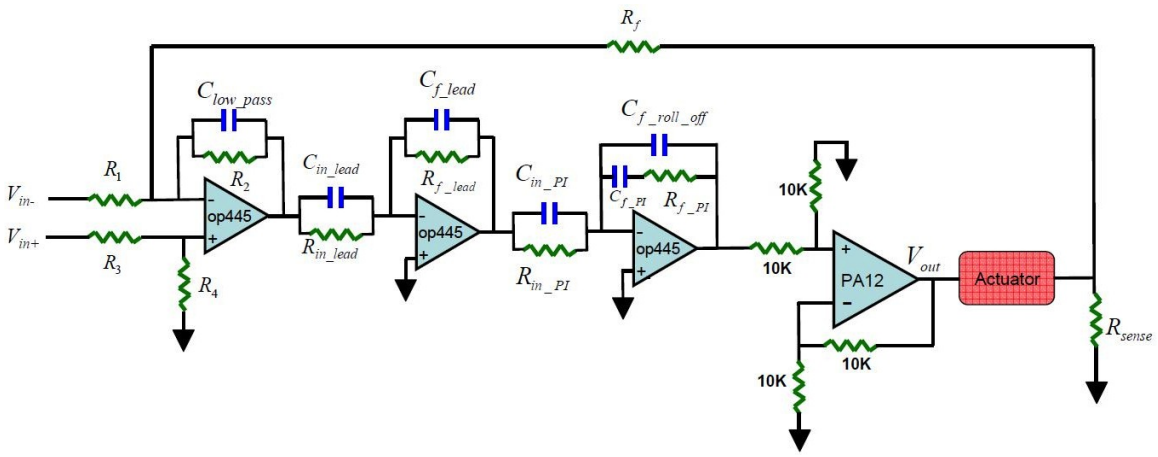

Figure 2-12: The circuit for the current control amplifier for reaction sphere designed by Dr. Imani Nejad.

2.8 Speed sensor

In order to feedback control the rotational speed of the reaction sphere, measurement of the sphere's speed in real-time is necessary. With a black mark on the sphere, the optical tachometers can give a TTL pulse when an edge of mark is detected. The sensing range of this optical tachometer is 1-250,000 RPM.

2.9 Summary

This chapter gives a brief introduction to the hardware of the 1D-MSRS. In the following several chapters, the design details, analysis and test results of the subsystems of the 1D-MSRS are presented. Chapter 3 introduces the sphere's vertical suspension and position control. Chapter 4 introduces the lateral suspension of the sphere. Chapter 5 presents the motor operation of the 1D-MSRS. Chapter 6 demonstrates the speed control for the 1D-MSRS.

Chapter 3

Single DOF Magnetic Suspension of Reaction Sphere

This chapter analyzes the working principles and control of the of the vertical suspension of the spherical rotor in the 1D-MSRS system. Figure 3-1 shows a photograph of the sphere being magnetically suspended. This single degree-of freedom magnetic levitation is the building block for multi-degrees-of-freedom magnetic suspension systems, such as magnetically levitated stages and bearingless motor systems.

Figure 3-2 shows a cross-section diagram of the magnetic suspension of the reaction sphere, which is comprised of the actuator core, the sphere, a permanent magnet, and excitation coil windings. In the design of the 1D-MSRS's vertical suspension actuation system, in order to reduce the DC current amplitude in the actuator coil and thus make the levitation more energy efficient, a disk-shape permanent magnet (PM) is arranged in the magnetic path of the suspension electromagnet to add a DC bias flux for sphere weight compensation. A photograph of the suspension actuator is shown in Figure 2-9. In this thesis let us call it a flux-biased actuator.

Another benefit of this flux-biased actuator design is that it allows a smaller actuator core diameter. As a result, the flux for vertical levitation can have less interaction with the flux generated by the stator around the equator of the sphere, and the vertical suspension and the torque generation can be better decoupled. An earlier larger electromagnet had problem with these effects.

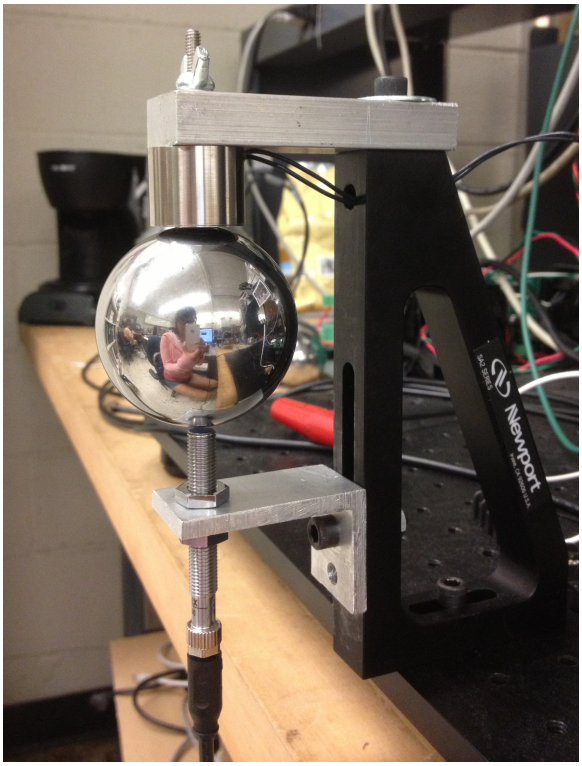

Figure 3-1: Vertical levitation of sphere by reluctance actuator with permanent magnet.

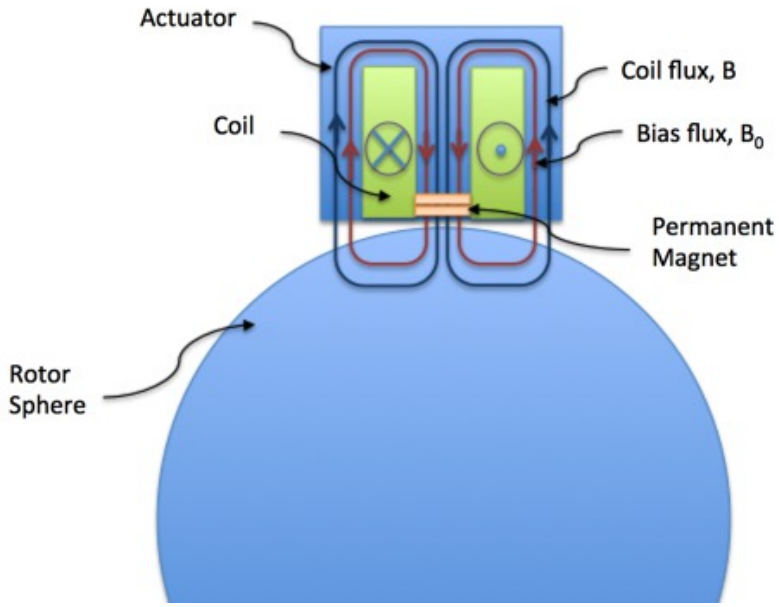

Figure 3-2: A cross section of the permanent-magnet biased vertical levitation actuation system.

In the rest of this chapter, a complete analysis of the levitation system for the reaction sphere is presented. We first calculate the force generated by the permanent magnet by means of a magnetic circuit model (Section 3.1). Then the suspension force from the coil, both DC and AC, is calculated (Section 3.2 and 3.3). What follows is the calculation of the dynamic equation and further the transfer function model for this magnetic levitation system (Section 3.4). Finally the control design to stabilize the magnetic suspension is discussed (Section 3.5).

3.1 Permanent magnet DC flux analysis

In this section the suspension force generated by the bias magnetic flux from the permanent magnet is calculated. Since the suspension of the sphere is using reluctance forces, the electromagnet can only generate attractive force to the sphere. Besides, based on the fact that at moderate size scale, a permanent magnet has much larger flux generation ability compared to a coil, if the sphere touches the actuator, the coil cannot provide sufficient repelling force to separate them. In order to avoid this sticking between the sphere and the actuator from happening, the DC suspension force generated by the permanent magnet need to be smaller than the sphere's weight. To achieve this design goal, the geometry of the permanent magnet and the air gap lengths needed to be carefully chosen based on magnetic force calculations. This was developed as an iterative process. In this thesis, only the calculations based on the final design parameter choice are presented.

Figure 3-3 shows the geometry and the dimension of the levitation actuation system. Here the actuator core's diameter is $D_a = 25.4$ mm. The actuator core height at the center is shorter than that at the periphery by 1 mm. The length of the permanent magnet is $L_{pm} = 0.8$ mm. What is not shown in the figure is that the sphere's radius $R_s = 27$ mm. Let us define the nominal air gap length at center of the actuator as g_{10}, and the nominal air gap length in the periphery of the actuator as g_{20}. Note here the length of the permanent magnet is not considered as a part of the central air gap length. The angle between the vertical axis and the line from

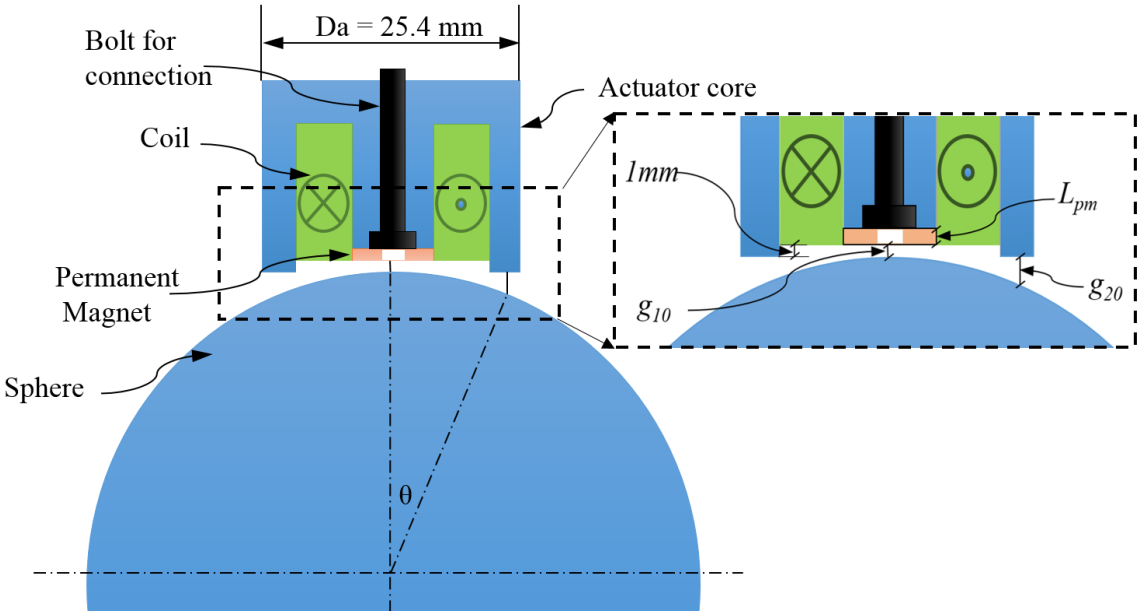

Figure 3-3: Geometry of the magnetic levitation actuation system.

the peripheral air gap to the sphere center is defined as θ. Based on the geometry relationships shown in Figure 3-3, we can have

$$\begin{aligned} \sin\theta &\approx \frac{D_a/2}{R_s}; \\ R_s\cos\theta + g_{20} + 1\text{mm} &= g_{10} + R_s. \end{aligned} \tag{3.1}$$

Based on these relationships, we can find that the air gap lengths g_{10} and g_{20} need to satisfy the following equation:

$$g_{20} = g_{10} + 2.2 \text{ mm}. \tag{3.2}$$

In the final design of the reaction sphere levitation system, the nominal air gap lengths at the center and at the periphery are selected to be $g_{10} = 0.8$ mm and $g_{20} = 3$ mm, respectively. In the below text in this section, the suspension force generated by the DC flux from the PM is calculated based on these selections.

In the calculation of the suspension force generated by the PM, a magnetic circuit model is being used. Because the permeability of the sphere and actuator core is

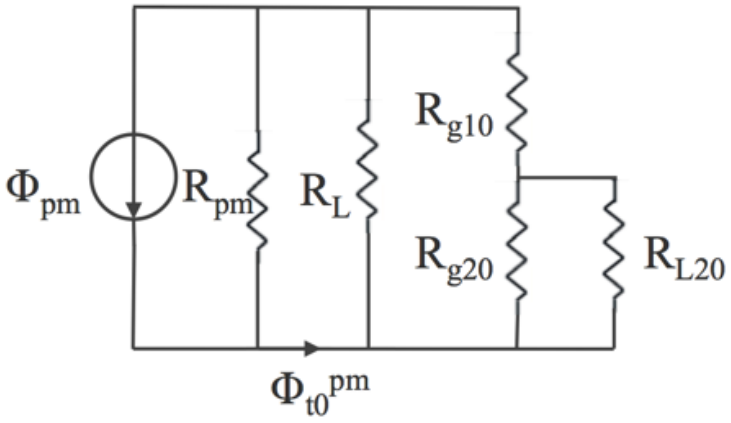

Figure 3-4: Equivalent magnetic circuit model for flux distribution in flux-biased levitation actuator. Φ_{pm} is the remanence flux of the permanent magnet. Φ_{t0}^{pm} is the total flux that flows out from the permanent magnet. R_{g10} and R_{g20} are the magnetic reluctances of air gap in the center and in the periphery, respectively. R_L and R_{L20} are the reluctances for leakage paths.

much larger than that of air, we can assume that the magnetic reluctances in the core and the in the sphere are zero. Based on the design shown in Figure 3-3, a magnetic circuit model shown in Figure 3-4 is built. Reference [20] gives a complete introduction to magnetic circuit modeling.

In the magnetic circuit model shown in Figure 3-4, the permanent magnet is modeled as a constant magnetic flux source Φ_{pm} with an internal reluctance R_{pm}. According to the permanent magnet model we are using (given in detail in Appendix A of [18]), $\Phi_{pm} = A_{pm} \cdot Br$, where A_{pm} is the pole face area of the permanent magnet, and $B_r = \mu_0 M$ is the remanence of the permanent magnet. Here M is the magnetization of the permanent magnet. For neodymium magnets $B_r = 1.2$ T. The total flux that flows into the remaining reluctances defined as Φ_{t0}^{pm}, where the superscript "pm" means they are the fluxes generated by the permanent magnet, and the subscript "0" means they are DC magnetic fluxes. The difference between Φ_{t0}^{pm} and the air gap fluxes goes through the major leakage path, which is modeled as a magnetic reluctance R_L. The two air gaps are modeled as reluctances R_{g10} and R_{g20}. As we have calculated before, the air gap length g_{20} is larger than g_{10} due to

the spherical geometry of the rotor. Therefore there is another leakage path with a reluctance of R_{L20} paralleling the reluctance R_{g20}, meaning some of the flux lines that goes through the air gap in the center does not flow through the air gap on the periphery. For the sake of simplicity, let us assume the cross-section area of the actuator core A_c is a constant along all the magnetic path, and it is also equal to the pole-face area of the permanent magnet A_{pm}, that is, $A_c = A_{pm}$. According to electromagnetic theory, the air gap and magnet reluctances in the magnetic circuit can be calculated as

$$R_{g10} = \frac{g_{10}}{\mu_0 Ac}; \tag{3.3a}$$

$$R_{g20} = \frac{g_{20}}{\mu_0 Ac}; \tag{3.3b}$$

$$R_{pm} = \frac{L_{pm}}{\mu_0 A_c}. \tag{3.3c}$$

Here μ_0 is the vacuum permeability. In the design of the reaction sphere levitation system, the actuator core has cross-section area of $A_c = 1.27 \times 10^{-4}\ m^2$, which is also the pole face area of the permanent magnet A_{pm}. By selecting the air gap lengths to be $g_{10} = 0.8$ mm, $g_{20} = 3$ mm, and the length of magnet to be $L_{pm} = 0.8$ mm, we can calculate the magnetic reluctances as

$$R_{g10} = \frac{g_{10}}{\mu_0 Ac} = \frac{0.8 \times 10^{-3}}{1.27 \times 10^{-4} \times 4\pi \times 10^{-7}} = 5.03 \times 10^6\ \frac{1}{H}; \tag{3.4a}$$

$$R_{g20} = \frac{g_{20}}{\mu_0 Ac} = \frac{3 \times 10^{-3}}{1.27 \times 10^{-4} \times 4\pi \times 10^{-7}} = 1.89 \times 10^7\ \frac{1}{H}; \tag{3.4b}$$

$$R_{pm} = \frac{L_{pm}}{\mu_0 A_{pm}} = \frac{0.8 \times 10^{-3}}{1.27 \times 10^{-4} \times 4\pi \times 10^{-7}} = 5.03 \times 10^6\ \frac{1}{H}. \tag{3.4c}$$

In the calculation of the leakage path reluctances, finite element method (FEM) is used to get an estimation of the ratio of the leakage flux and the flux in the air gaps. Figure 3-5 shows a field plot of the permanent magnet flux by the open source finite element analysis package FEMM [21].

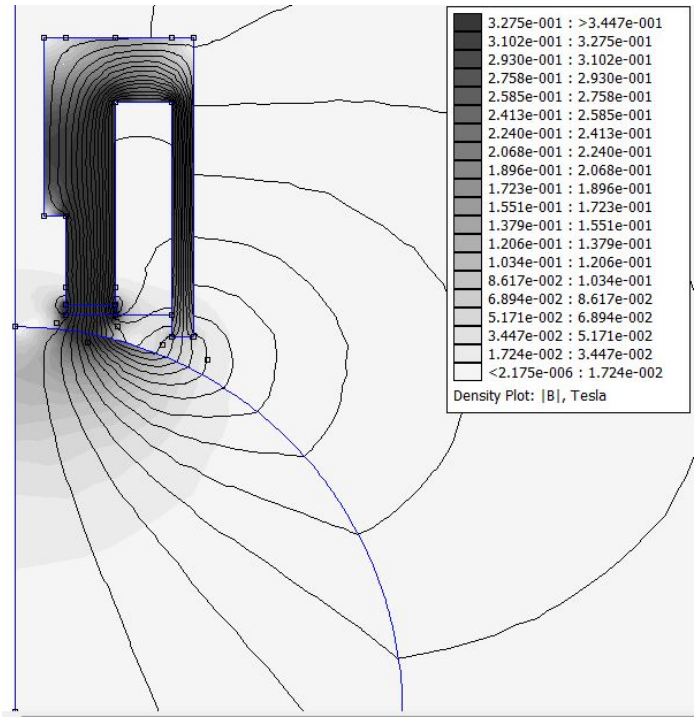

Figure 3-5: FEA solution of permanent magnet generated flux density distribution in levitation actuate system using actual design parameters. The permeability of both the actuator core and sphere material are assumed as $5000\mu_0$.

From the FEM solution shown in Figure 3-5, we can see that the numbers of the flux lines that flow through the two air gaps are not identical. Figure 3-5 shows that the total flux that flows out from the permanent magnet Φ_{t0}^{pm} corresponds to 19 flux lines. The flux that goes into the air gap in the center has 12 flux lines, and the flux goes through the air gap in the periphery only has 4 flux lines. From this estimation, we can calculate the leakage reluctances as

$$\frac{R_{g20}}{R_{L20}} = \frac{12-4}{4} \longrightarrow R_{L20} = \frac{4}{8} R_{g20} = 9.43 \times 10^6 \ \frac{1}{H} \tag{3.5}$$

$$\frac{R_{g10} + R_{g20}//R_{L20}}{R_L} = \frac{19-12}{12} \longrightarrow R_L = \frac{12}{7}(R_{g10} + R_{g20}//R_{L20}) = 1.94 \times 10^7 \ \frac{1}{H}. \tag{3.6}$$

With the cross-section area $A_{pm} = A_c = 1.27 \times 10^{-4}\text{m}^2$ and remanence flux density $B_r = 1.2\text{T}$, the flux source strength Φ_{pm} can be calculated as

$$\Phi_{pm} = B_r A_{pm} = 1.2 \times 1.27 \times 10^{-4} = 1.45 \times 10^{-4} \text{ Wb.} \tag{3.7}$$

With the source strength and all the reluctance values calculated, we can now apply the circuit theory to calculate the flux in the air gaps with the magnetic circuit model in Figure 3-4. The total flux flows out from the permanent magnet Φ_{t0}^{pm} can be calculated as:

$$\Phi_t = \Phi_{pm} \frac{R_{pm}}{R_{pm} + R_L//(R_{g10} + R_{g20}//R_{L0}}) = 6.27 \times 10^{-5} \text{ Wb.} \tag{3.8}$$

Then the flux that goes into the air gap in the center is

$$\Phi_{g10}^{pm} = \Phi_t \frac{R_L}{R_L + (R_{g10} + R_{g20}//R_{L20}}) = 3.96 \times 10^{-5} \text{ Wb.} \tag{3.9}$$

As before, the superscript "pm" means that this is the flux generated by the permanent magnet, and the subscript "0" means this is the DC part of the magnetic flux. Similarly, the flux that flows into the air gap in the periphery is

$$\Phi_{g20}^{pm} = \Phi_{g1} \frac{R_{L20}}{R_{g20} + R_{L20}} = 1.32 \times 10^{-5} \text{ Wb.} \tag{3.10}$$

The flux density in the two air gaps can be calculated by

$$B_{g10}^{pm} = \frac{\Phi_{g10}^{pm}}{Ac} = 0.31 \text{ T;} \tag{3.11a}$$

$$B_{g20}^{pm} = \frac{\Phi_{g20}^{pm}}{Ac} = 0.10 \text{ T.} \tag{3.11b}$$

Then the reluctance force for magnetic levitation is calculated by Maxwell stress tensor method. Since all the fluxes in the air gaps are approximately in the vertical direction, the The total levitation force generated by the permanent magnet can be calculated as

$$f_0^{PM} = A_c \frac{(B_{g10}^{pm})^2}{2\mu_0} + A_c \frac{(B_{g20}^{pm})^2}{2\mu_0} = 5.43 \text{ N.} \tag{3.12}$$

By checking with the force calculation result of 5.35 N given by finite element method, we conclude that the suspension force calculation by the magnetic circuit model has acceptable accuracy.

A comparison between the calculated suspension force and the sphere's weight is needed to show that the sphere will not stick to the actuator. The weight of the rotor sphere is

$$W_{sphere} = g\rho_{steel}\frac{4}{3}\pi R_s^3. \tag{3.13}$$

Here ρ_{steel} is the density of the rotor material, R_s is the rotor sphere's radius, g is the gravitational acceleration. By substituting in $R_s = 27 \times 10^{-3}$ m, $\rho_{steel} = 7.9 \times 10^3$ kg/m^3, and $g = 9.8$ m/s, we can get

$$W_{sphere} = 6.38 \text{ N}. \tag{3.14}$$

Based on these calculation, we can see that that the sphere's weight is greater than the suspension force generated by the permanent magnet, and this bias flux compensated 85% of the sphere's weight. The rest of the sphere's weight is balanced by the levitation force generated by the DC current of the coil, which is calculate in the next section.

3.2 Coil DC flux analysis

In this section the DC part of the coil current and its corresponding suspension force generation are analyzed. The levitation actuator for the sphere's suspension is modified from a commercial electromagnet, therefore the exact number of turns of the coil is unknown. However, an estimation of the number of turns can be achieved by the DC current measurement and the analysis in this section.

Figure 3-6 shows a magnetic circuit model of the levitation actuation system with only the permanent magnet and the DC part of the coil current considered. The total Ni_0 Ampere-turns of the coil is modeled as a voltage source in the magnetic circuit, where N is the number of turns of the coil, and i_0 is the DC coil current

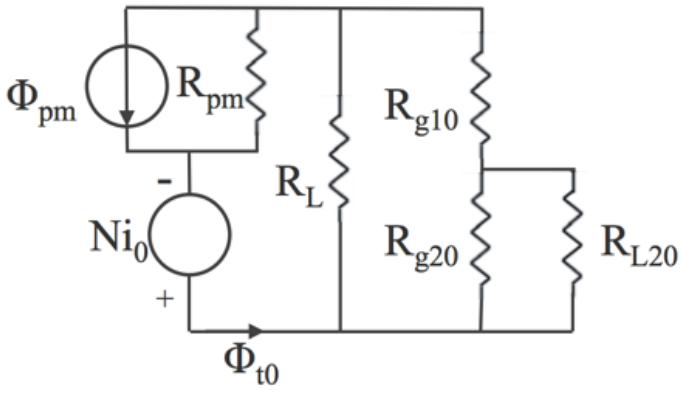

Figure 3-6: Equivalent magnetic circuit model of DC flux distribution in the flux-biased levitation actuator. Φ_{pm} is the remanence flux of the permanent magnet. Ni_0 is the total Ampere-turn of the DC current of the coil. Φ_{t0} is the total DC flux that flows out from the DC flux sources. R_{g10} and R_{g20} are the magnetic reluctances of air gap in the center and in the periphery respectively. R_{pm} is the internal reluctance of the permanent magnet. R_L and R_{L20} are the reluctances for leakage paths.

amplitude. In this model we assume that this voltage source is connected in series with the permanent magnet, which means all the magnetic flux generated by the coil is flowing through the permanent magnet. As a result, all the reluctances are of the same values as in the previous section.

The flux generated by the DC coil current should compensate the weight of the sphere together with the permanent magnet. In the following derivation, we calculate the required flux to compensate the sphere's weight, and thus calculate the needed Ampere-turns of the actuator coil.

Define the total DC flux density in the center and periphery air gaps are B_{g10} and B_{g20} respectively, and the corresponding fluxes are Φ_{g10} and Φ_{g20}. To compensate the total weight of the sphere, the following equation needs to be satisfied:

$$W_{sphere} = A_c \frac{B_{g10}^2}{2\mu_0} + Ac \frac{B_{g20}^2}{2\mu_0}. \tag{3.15}$$

Define the total DC flux that flows into the magnetic circuit is Φ_{t0}, which is also shown in Figure 3-6. From the magnetic circuit model, we can calculate the total DC

air gap fluxes by

$$\Phi_{g10} = \Phi_{t0}\frac{R_L}{R_L + R_{g10} + R_{g20}//R_{L20}}; \tag{3.16a}$$

$$\Phi_{g20} = \Phi_{g10}\frac{R_{L2}}{R_{L20} + R_{g20}}. \tag{3.16b}$$

By substituting in the values of the reluctances, we can get the values of the air gap fluxes as

$$\Phi_{g10} = 0.63 \times \Phi_{t0}; \tag{3.17a}$$

$$\Phi_{g20} = 0.21 \times \Phi_{t0}. \tag{3.17b}$$

With both air gaps having the same area of A_c, the total DC levitation force can be written as

$$\begin{aligned} f_0 &= A_c\frac{B_{g10}^2}{2\mu_0} + A_c\frac{B_{g20}^2}{2\mu_0} \\ &= \frac{\Phi_{g10}^2}{2\mu_0 A_c} + \frac{\Phi_{g20}^2}{2\mu_0 A_c} \\ &= \frac{0.63^2 + 0.21^2}{2\mu_0 A_c}\Phi_{t0}^2. \end{aligned} \tag{3.18}$$

This total DC levitation force should be balanced with the total weight of the sphere, that is

$$f_0 = \frac{0.63^2 + 0.21^2}{2\mu_0 A_c}\Phi_{t0}^2 = W_{sphere}. \tag{3.19}$$

Substitute in the values of A_c, μ_0 and W_{sphere}, we can calculate the value of the total DC flux as

$$\Phi_{t0} = 6.78 \times 10^{-5}\ Wb. \tag{3.20}$$

This is the total needed DC flux for sphere weight compensation. We have calculated in the previous section that the total flux that generated by the permanent magnet is $\Phi_{t0}^{pm} = 6.27 \times 10^{-5}$ Wb. Therefore the total DC flux that generated by the coil's DC current should be

$$\Phi_{t0}^{coil} = \Phi_{t0} - \Phi_{t0}^{pm} = 4.95 \times 10^{-6} \text{ Wb.} \tag{3.21}$$

Then the needed voltage source strength in the magnetic circuit (magnetic potential) Ni_0 can be calculated as

$$Ni_0 = \Phi_{t0}^{coil} \times (R_{pm} + R_L//(R_{g10} + R_{g20}//R_{L20})) = 60.27 \text{ V} \cdot \text{s/m.} \tag{3.22}$$

Since the exact number of turns of the coil is unknown, we can use the calculated result to identify the value of N approximately. When the sphere being levitated, the experimental measured DC coil current value is $i_0 = 0.24$ A. Therefore the number of turns is approximately $N = 250$ turns. This is a reasonable estimation according to the size of the actuator and the wire gauge of the coil. This approximate value will be used in the derivation in the later sections.

3.3 AC flux by coil

Aside from the DC suspension force for sphere's weight compensation, AC suspension force is needed to control the sphere's vertical position. This force is generated by the AC fluxes in the magnetic levitation actuation system.

Figure 3-7 shows a magnetic circuit model of the flux-biased magnetic levitation system with only the components related to the AC flux generation. In Figure 3-7, the coil is excited by the varying current of $\tilde{i}$, so that the total AC voltage source in the magnetic circuit is $N\tilde{i}$ Ampere-turns. The air gap reluctances R_{g1} and R_{g2} become adjustable because the variation of the air gap length is included in the model. This air gap length variation can influence the air gap fluxes for levitation force generation.

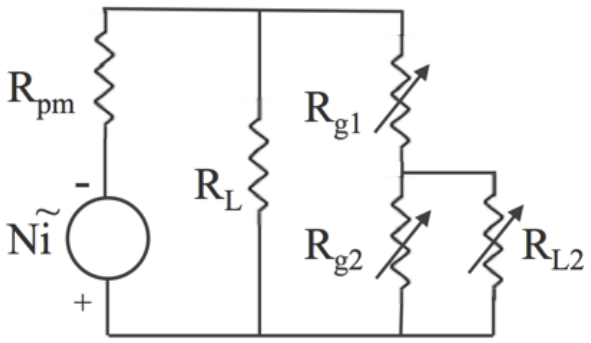

Figure 3-7: Magnetic circuit model of the AC flux in flux-biased levitation actuator. $N\tilde{i}$ is the total Ampere-turns of the AC current of the coil. R_{g1} and R_{g2} are the magnetic reluctances of air gap in the center and in the periphery respectively, with the air gap length variation considered. R_{pm} is the internal reluctance of the permanent magnet. R_L and R_{L2} are the reluctances for leakage paths.

Let us define the air gap lengths at the center and the periphery by

$$g_1 = g_{10} + \tilde{g_1}; \tag{3.23a}$$

$$g_2 = g_{20} + \tilde{g_2}. \tag{3.23b}$$

Here g_{10}, g_{20} are the average air gap length in the center and the periphery respectively, and $\tilde{g_1}$, $\tilde{g_2}$ are the variation of the corresponding air gap length. Since the goal of the sphere's magnetic levitation control is to keep its vertical position a constant, then the air gap variations $\tilde{g_1}$ and $\tilde{g_2}$ should be much smaller than the average air gap lengths. The corresponding reluctances are

$$R_{g1} = \frac{g_{10} + \tilde{g_1}}{\mu_0 Ac} \tag{3.24a}$$

$$R_{g2} = \frac{g_{20} + \tilde{g_1}}{\mu_0 Ac}. \tag{3.24b}$$

In our modeling of the AC flux magnetic circuit, the major leakage reluctance R_L is designed to be a constant, since the major leakage flux that goes through R_L is

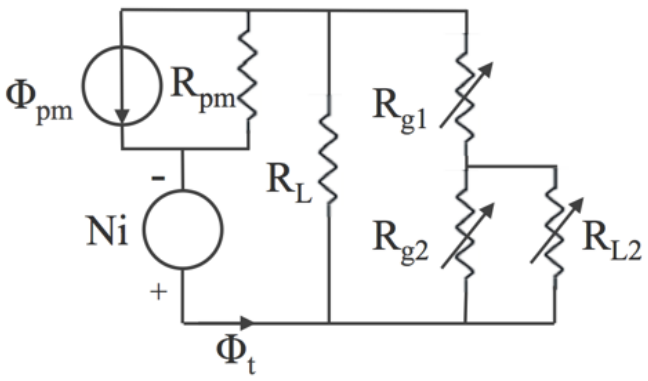

Figure 3-8: Magnetic circuit model of total flux distribution in flux-biased levitation actuator. Φ_{pm} is the remanence flux of the permanent magnet. Ni is the total Ampere-turn of the current of the coil, both DC and AC. Φ_t is the total flux that flows out from the flux sources. R_{g1} and R_{g2} are the magnetic reluctances of air gap in the center and in the periphery respectively, with the variation of the air gap lengths considered. R_{pm} is the internal reluctance of the permanent magnet. R_L and R_{L2} are the reluctances for leakage paths, where R_L is constant while R_{L2} is varying with R_{g2}.

mainly determined by the geometry of the actuator core, which is not changing with the variation of the air gap lengths. On the other hand, the reluctance R_{L2} is modeled as adjustable, since the variation of the air gap length in the periphery should have a significant influence on the leakage flux that flows through R_{L2}. In the analysis of this thesis, it is modeled as having a constant ratio with the air gap of R_{g2}, that is, the ratio of the flux in air gap 2 and the flux that leaks is constant. This model is being used in the derivation of the dynamic model of the sphere's magnetic levitation, which is presented in detail in the next section.

3.4 Magnetic levitation system modeling

In this section, the total flux in the flux-biased magnetic levitation actuation system is considered, and the transfer function from the coil current to the sphere's displacement is derived. After that, experimental measured plant frequency response data of the sphere's magnetic suspension is being used to verify the calculated result.

Figure 3-8 shows a magnetic circuit model of with both DC and AC fluxes con-

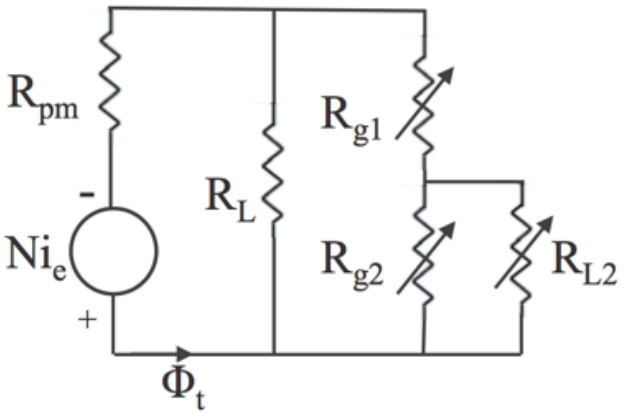

Figure 3-9: Equivalent magnetic circuit model of total flux in the flux-biased levitation actuation system. Ni_e is the equivalent total Ampere-turn in the coil.

sidered. The air gap reluctances R_{g1} and R_{g2} are defined in (3.24). The modeling of the leakage path reluctances follows the discussion in the AC flux section. The coil current i contains both DC and AC current, and can be written as $i = i_0 + \tilde{i}$. The model of the permanent magnet is the same as the model in Section 3.1.

In the model shown in Figure 3-8, there are two sources of DC flux: the permanent magnet and the DC current in the coil. The two sources are connected in series, working together to generate the DC flux for sphere's weight compensation. To make the model simpler, we can use an equivalent coil with DC current i_{e0} to replace these two sources. Figure 3-9 shows the new magnetic circuit model with this equivalent voltage source of Ni_e, with the current defined by $i_e = i_{e0} + \tilde{i}$.

To make the model in Figure 3-9 equivalent with the one in Figure 3-8, the generated total flux should be equal. We have calculated in Section 3.2 that the total flux generated by the two DC flux sources is $\Phi_{t0} = 6.78 \times 10^{-5}$ Wb. Let us define a magnetic reluctance value R_{total} as $R_{total} = R_{pm} + R_l//(R_{g1} + R_{g2}//R_{L2})$, and its average value is then $R^0_{total} = R_{pm} + R_l//(R_{g10} + R_{g20}//R_{L2}) = 1.22 \times 10^7 \ \frac{1}{\mathrm{H}}$. To make the two model equivalent in the DC flux generation, the following equation should hold:

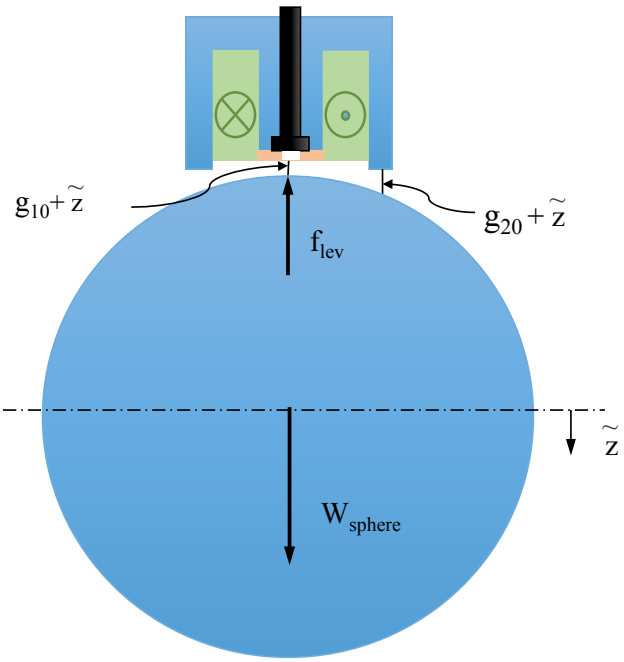

Figure 3-10: Magnetic levitation diagram of the reaction sphere. Incremental $\tilde{z}$ is the rotor sphere's vertical displacement variation, with its positive direction pointing downward. Air gap lengths at the center and the periphery are then $g_{10} + \tilde{z}$ and $g_{20} + \tilde{z}$.

$$\begin{aligned} Ni_e &= \Phi_{t0} \times R^0_{total} \\ &= 6.78 \times 10^{-5} \times 1.22 \times 10^7 \\ &= 824.22\text{V} \cdot \text{s/m}. \end{aligned} \tag{3.25}$$

As calculated in Section 3.2, the number of turns of the coil is approximately $N = 250$. Then the DC part of the equivalent current is approximately $i_{e0} = 3.30$A. These values, together with the equivalent magnetic circuit model shown in Figure 3-9, are used to derive the plant transfer function for the magnetic levitation system in this section.

Figure 3-10 shows a diagram of the magnetic levitated reaction sphere. f_{lev} is the levitation force. W_{sphere} is the weight of the sphere. $\tilde{z}$ is the rotor sphere's vertical displacement variation, with its positive direction pointing downward. Air gap lengths at the center and the periphery are $g_{10} + \tilde{x}$ and $g_{20} + \tilde{z}$ respectively. We also assume

the sphere's displacement is small compared to the nominal air gap lengths.

Based on the air gap reluctance models in (3.24) and the air gap lengths given above, we can write the air gap reluctances as

$$R_{g1} = \frac{g_{10} + \tilde{z}}{\mu_0 Ac}; \tag{3.26a}$$

$$R_{g2} = \frac{g_{20} + \tilde{z}}{\mu_0 Ac}. \tag{3.26b}$$

Equation (3.24) shows that the air gap reluctances are linear to the rotor sphere's vertical position variation $\tilde{z}$.

Then the total suspension force is calculated based on the equivalent model shown in Figure 3-9. The total flux, DC and AC, that flows through the air gap in the center can be calculated as

$$\Phi_{g1} = \frac{Ni_e}{R_{total}} \frac{R_L}{R_L + R_{g1} + R_{g2}//R_{L2}}, \tag{3.27}$$

and the flux that flows through the air gap in the periphery is

$$\Phi_{g2} = \Phi_{g1} \frac{R_{L2}}{R_{g2} + R_{L2}}. \tag{3.28}$$

In the calculation of the air gap magnetic fluxes and further the levitation force, we follow the assumptions in the previous section for the leakage reluctances by letting R_{L2} keep proportional to the reluctance of R_{g2}, while let the major leakage reluctance R_L keep a constant value. Another assumption for this calculation is that the total magnetic reluctance R_{total} is not varying with the sphere's vertical position variance, since by looking at the definition of $R_{total} = R_{pm} + R_L//(R_{g1} + R_{g2}//R_{L2})$, we can see that the total reluctance is mainly determined by R_{pm} and R_L. These assumptions will significantly simplify the derivation of the magnetic force derivation. Based on the assumption for the leakage path reluctance and the flux ratio given in Section 3.1, we can find the relationship between R_{L2} and R_{g2} as

$$\frac{R_{L2}}{R_{g2}} = \frac{R_{g20}}{R_{L20}} = \frac{1}{2}. \tag{3.29}$$

Then Equation 3.28 becomes

$$\Phi_{g2} = \Phi_{g1}\frac{R_{L2}}{R_{g2} + R_{L2}} = \frac{1}{3}\Phi_{g1}. \tag{3.30}$$

As a result, the total magnetic suspension force can be calculated by Maxwell stress tensor as

$$\begin{aligned} f &= A_c\frac{B_{g1}^2}{2\mu_0} + A_c\frac{B_{g2}^2}{2\mu_0} \\ &= \frac{\Phi_{g1}^2}{2A_c\mu_0} + \frac{\Phi_{g2}^2}{2A_c\mu_0} \\ &= \frac{10}{9}\frac{\Phi_{g1}^2}{2A_c\mu_0} = \frac{5}{9}\frac{\Phi_{g1}^2}{A_c\mu_0} \end{aligned} \tag{3.31}$$

By substitute the value of Φ_{g1} in (3.27) and the magnetic reluctances for the air gaps in (3.26), the magnetic suspension force is

$$\begin{aligned} f &= \frac{5}{9A_c\mu_0}\frac{N^2 i_e^2}{R_{total}^2}\frac{R_L^2}{(R_L + R_{g1} + R_{g2}/3)^2} \\ &= \frac{5}{9A_c\mu_0}\frac{N^2 i_e^2}{R_{total}^2}\frac{R_L^2}{(R_L + R_{g10} + R_{g20}/3 + \frac{4\tilde{x}}{3\mu_0 A_c})^2}. \end{aligned} \tag{3.32}$$

Equation (3.32) shows that the magnetic suspension force acting on the sphere rotor is nonlinear respect to both the exciting current in the coil i and the sphere's vertical displacement $\tilde{x}$. The dynamic equation of the sphere in Figure 3-10 is

$$mg - f = m\ddot{\tilde{z}}, \tag{3.33}$$

where m is the mass of the sphere, and g is the gravitational acceleration.

In the following derivation, a linearized model is developed for this second-order suspension system shown in Figure 3-10. Following the notation of the operating

points and incremental quantities in previous sections, we let $i_e = i_{e0} + \tilde{i}$, $z = 0 + \tilde{z}$, and $f = f_0 + \tilde{f}$. The subscript "0" indicates the operating point value, and the tilde indicates the incremental value of the variable.

A linearized model of the magnetic suspension force in (3.32) is reached by taking a Taylor expansion of f respect to i and $\tilde{x}$:

$$f = f_0 + \frac{\partial f}{\partial \tilde{z}}\Big|_{z=0,i=i_{e0}} \tilde{z} + \frac{\partial f}{\partial i}\Big|_{z=0,i=i_{e0}} \tilde{i} \tag{3.34}$$

Let us define variables K_i and K_s by letting $K_i = \frac{\partial f}{\partial i}\Big|_{z=0,i=i_{e0}}$ and $K_s = \frac{\partial f}{\partial \tilde{z}}\Big|_{z=0,i=i_{e0}}$. By taking a appropriate partial derivatives to (3.32) and evaluating them at the operating point yields these values as

$$f_0 = f\Big|_{z=0,i=i_{e0}} = \frac{5}{9A_c\mu_0}\frac{N^2 i_{e0}^2}{R_{total}^2}\frac{R_L^2}{(R_L + R_{g10} + R_{g20}/3)^2} = 6.38 \text{ N}; \tag{3.35a}$$

$$K_s = -\frac{\partial f}{\partial \tilde{z}}\Big|_{z=0,i=i_{e0}} = -\frac{5}{9A_c\mu_0}\frac{N^2 i_{e0}^2 R_L^2}{R_{total}^2}\frac{-2\frac{4}{3\mu_0 A_c}}{(R_L + R_{g10} + R_{g20}/3)^3} = 6.97e \times 10^3 \text{ N/m}; \tag{3.35b}$$

$$K_i = \frac{\partial f}{\partial i}\Big|_{z=0,i=i_{e0}} = \frac{5}{9A_c\mu_0}\frac{N^2 R_L^2}{R_{total}^2}\frac{2i_{e0}}{(R_L + R_{g10} + R_{g20}/3)^2} = 7.74 \text{ N/A}. \tag{3.35c}$$

Notice that in this system the DC part of the suspension force f_0 is equal to the sphere's weight. Then the linearized dynamic equation of the sphere can be written as

$$-K_i\tilde{i} + K_s\tilde{x} = m\ddot{\tilde{z}}. \tag{3.36}$$

Take a Laplace transform to Equation (3.36), the transfer function from current to sphere's position is given by

$$\frac{Z(s)}{I(s)} = -\frac{K_i}{ms^2 - K_s}. \tag{3.37}$$

Here a negative sign exists in the transfer function, meaning a positive current

input will tend to decrease the displacement variation $\tilde{z}$. With the sign in front of K_s being negative in the denominator, the transfer function have real axis poles at $s = \pm\sqrt{\frac{K_s}{m}}$. The pole at $+\sqrt{\frac{K_s}{m}}$ is of course unstable, and will need feedback control to stabilize this system. In magnetic suspension systems, the value of K_s is often called "negative stiffness".

With the value of m, K_i and K_s substituted into (3.37), we can get the numerical value of the transfer function from the current to the sphere's incremental displacement as

$$\frac{X(s)}{I(s)} = -\frac{7.74}{s^2 - 6968}. \tag{3.38}$$

To verify the calculated model given above, a comparison between an experimental measured Bode plot and the Bode plot from the model is performed. In the 1D-MSRS hardware, the displacement sensor for the sphere has a gain of 1.25 V/mm, and the current control amplifier has a gain of 0.2 A/V. So when comparing the two Bode plots, a gain of 1.25 V/mm $\times$ 1000 mm/m $\times$ 0.2 A/V = 250 A/m must be taken into account. The Bode plot is measured by a Dynamic Signal Analyzer with the magnetic suspension under closed-loop control. Figure 3-11 shows the experimental measured Bode plot of this magnetic suspension system (with the sensor and actuator gains removed) and the Bode plot of the modeled system in (3.37) together. Good match between the measured data and the model validates the calculation.

3.5 Magnetic suspension control of the reaction sphere

This section introduces the control for the magnetic suspension for the reaction sphere. As discussed in the previous section, there is one right plane pole in the plant transfer function, and this make the system inherently unstable. As a result, feedback control is needed to stabilize the system.

The controller's design is based on the plant transfer function from the previous section, both the model and the identified Bode plot. The plant transfer function is depicted in Figure 3-11. By removing the negative sign in the plant transfer function

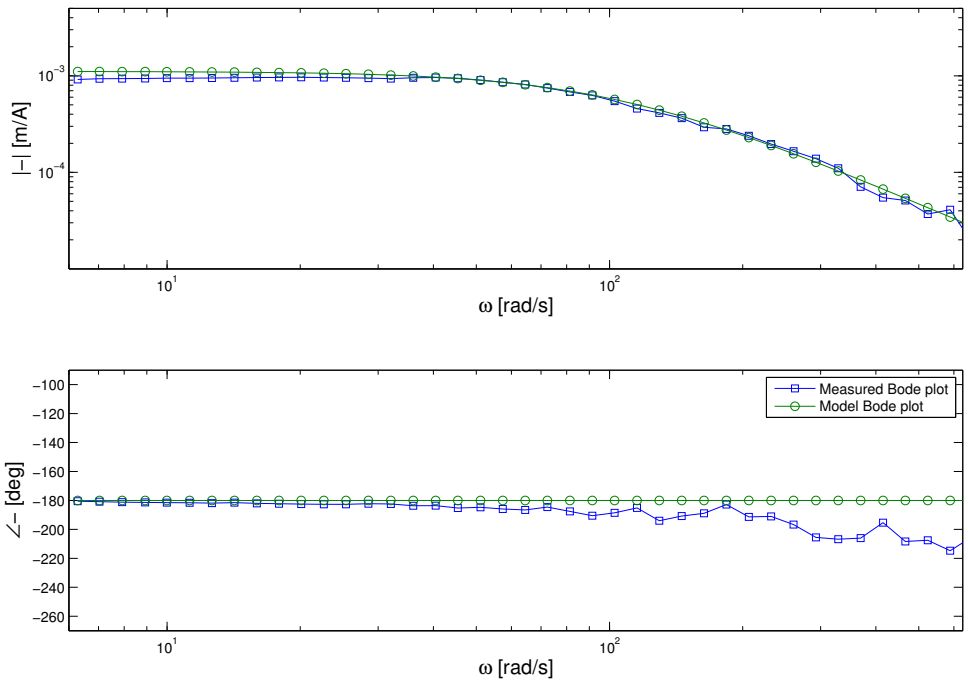

Figure 3-11: Bode plot of the plant transfer function of the sphere magnetic levitation system from the coil current i [A] to the sphere's vertical displacement z [m]F. Blue: experimental measured data; green: model.

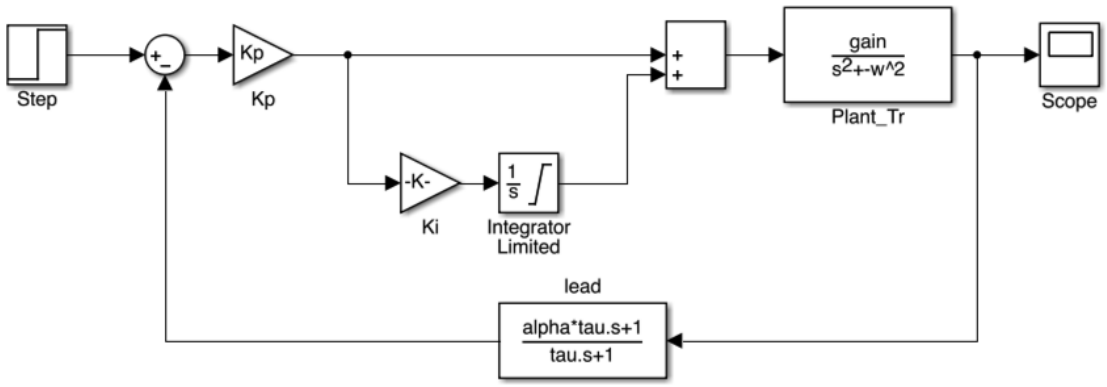

Figure 3-12: Block diagram of the levitation control loop for the reaction sphere.

without loss of generality, the numerical value of the transfer function is given by

$$\frac{Z(s)}{I(s)} = \frac{1936}{s^2 - 6968}. \tag{3.39}$$

We use series compensation to stabilize this magnetic suspension system. This is the approach that is generally used in practice as it only assumes the measurement of the sphere's vertical position. Lead-lag form of the PID controller is used for both stabilization and providing better disturbance rejection ability.

For the controller design, the lead network is chosen to have a pole-zero separation factor $\alpha = 10$. The loop is designed to cross over at 300 rad/s, thus we can calculate the lead time constant $\tau = 0.0014$ s to place the phase maximum at the desired crossover frequency. The integral gain for the system K_i is chosen to be 50. Figure 3-12 shows a block diagram of the control loop for this magnetic suspension system.

One thing worth pointing out is that for the levitation control for the reaction sphere we choose to place the lead compensator in the feedback path. Compared to the step response of a loop with a forward path lead compensator, placing the lead controller in the feedback path helps reduce the peak control effort by a factor of 10 (the α value of the lead network), and further reduce the overshoot of the position signal. A prefilter is also added to the loop to achieve a smoother step response. [22] gives a great reference on the controller design for a magnetic suspension system.

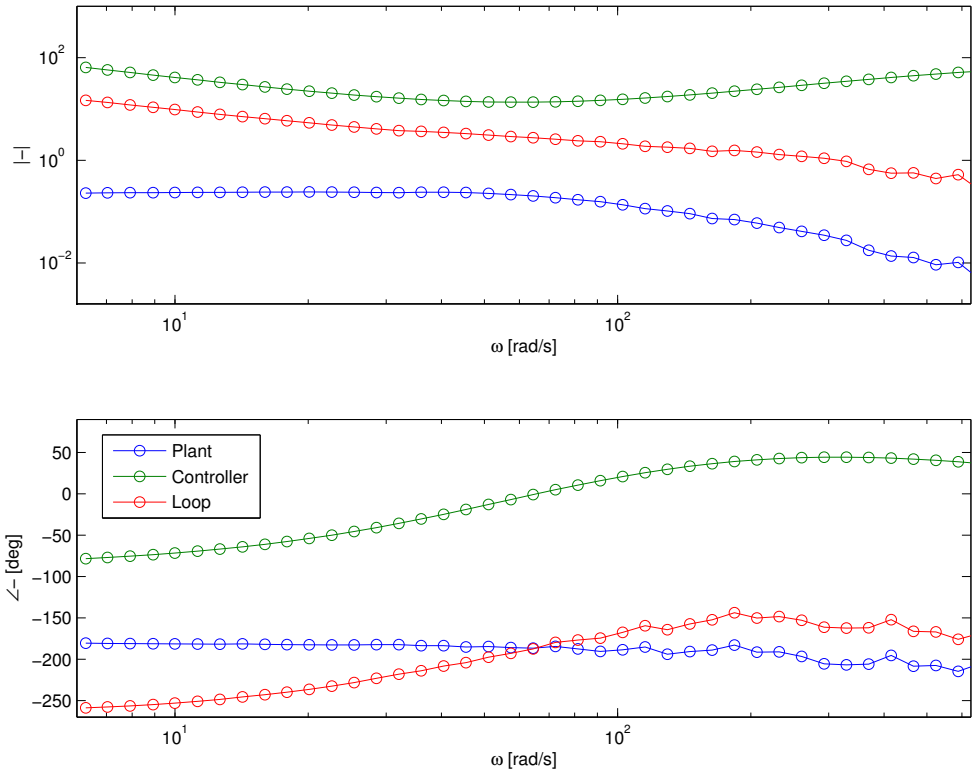

Figure 3-13: Bode plot for levitation plant, controller and loop return ratio. Crossover frequency is 300 rad/s with a phase margin of 37^o.

Figure 3-13 shows the Bode plot for the controller, plant and the loop return ratio for this control loop. By the controller we are showing in the plot, a crossover frequency of 300 rad/sec is reached, with a phase margin of 44^o.

3.6 Summary

In this chapter, a complete calculation for the magnetic suspension for the reaction sphere is presented. In the design of the levitation actuator, a piece of permanent magnet is added in the magnetic path of the actuator to add bias DC flux. The bias flux from the permanent magnet compensates 85% of the sphere's weight. This DC bias flux significantly reduces the DC current amplitude in the coil in the actuator slot to $i_0 = 0.24$ A in steady state. The dynamic equation of the sphere's magnetic

suspension is derived, and a transfer function is achieved by linearizing the equation. The model is verified by experimental measured Bode plot. In the transfer function, there is one stable pole and one unstable pole, so that the system will need closed-loop control to be stable. The controller design is also presented in this chapter, and a crossover frequency of 300 rad/s and a phase margin of 37^o is achieved.

The vertical suspension of the sphere is a typical single degree-of-freedom magnetic levitation system system. This is the foundation for studying magnetic suspension with multi degrees-of-freedom. The radial magnetic suspension of the reaction sphere is achieved by bearingless motor, which is discussed in the next chapter.

Chapter 4

Bearingless Motor System Modeling and Control

In order to drive the rotation and lateral suspension of the reaction sphere simultaneously, a bearingless motor is adopted in the 1D MSRS's design. The bearingless motor is implemented using two sets of windings on a single stator. By correctly configuring and controlling the current in these windings, the machine can generate radial force for suspension as well as a rotational magnetic field for spinning with only one stator assembly.

The first primitive electromagnet, i.e. motor drive, with stator windings having pole numbers of P and $P \pm 2$ was proposed by Hermann [23] in the middle of 1970s. This electromagnet was proposed as a motor which has a radial magnetic bearing function. Later, in 1990 Chiba and Fukao introduced a general concept for the bearingless motor [17]. Based on field-oriented theory, they concluded that most electrical machines can be used in a bearingless drive with additional suspension windings driven by a 3-phase inverter. The general concept is well explained in [24].

In this chapter, the principle of the suspension force generating in bearingless motors is introduced first. Then a complete mathematical model of the bearingless motor's lateral suspension is derived, and this model is used to analyze the reaction sphere's lateral suspension. Finally the AC excitations and the controller design for the sphere's lateral suspension based on analysis and experimental results are pre-

sented. The motor operation of the reaction sphere is presented in the next chapter.

4.1 Radial force generation principle of bearingless motor

In this section, the principles of magnetic suspension of bearingless machines are introduced. The multiple winding type bearingless motor uses the so-called P $\pm$ 2 principle. This means the motor has two sets of windings of P poles and P $\pm$ 2 poles respectively. Let us use a typical bearingless stator with 4-pole and 2-pole windings with a cylindrical rotor made of solid steel are described to demonstrate the concept, where the 4-pole winding is for rotational drive, while the 2-pole winding works for suspension control. That is, we use P = 4 for the motor windings and P = 4-2 = 2 for the suspension windings. The mechanical phase shift between the two windings is 45^o so that they are electrically orthogonal. For the sake of simplicity, we assume 2-phase windings without loss of generality.

Figure 4-1 shows a diagram of the bearingless motor under different conditions. In Figure 4-1 (a), there is a symmetrical 4-pole flux distribution around the motor. The green circles in the stator denote the conductors of the phase a in the 4-pole winding. The solid curves illustrate the flux paths circulating around the four concentrated conductors $4a$. These conductors are located in the stator slots. The 4-pole flux wave Φ_{4a} produces magnetic poles in the order N, S, N and S on the rotor at the air gaps 1, 2, 3 and 4 respectively. Since the flux distribution is symmetrical, the flux density magnitudes in the air gaps 1 to 4 are of the same value. There are attractive magnetic forces between the rotor poles and the stator iron, and under this condition the amplitudes of these attractive radial forces are the same, but the directions are equally distributed so that the sum of radial force acting on the rotor is zero in this center case.

Figure 4-1 (b) shows the principle of suspension force generation in x-direction. The blue circles denote phase a in the 2-pole winding. The two concentrated con-

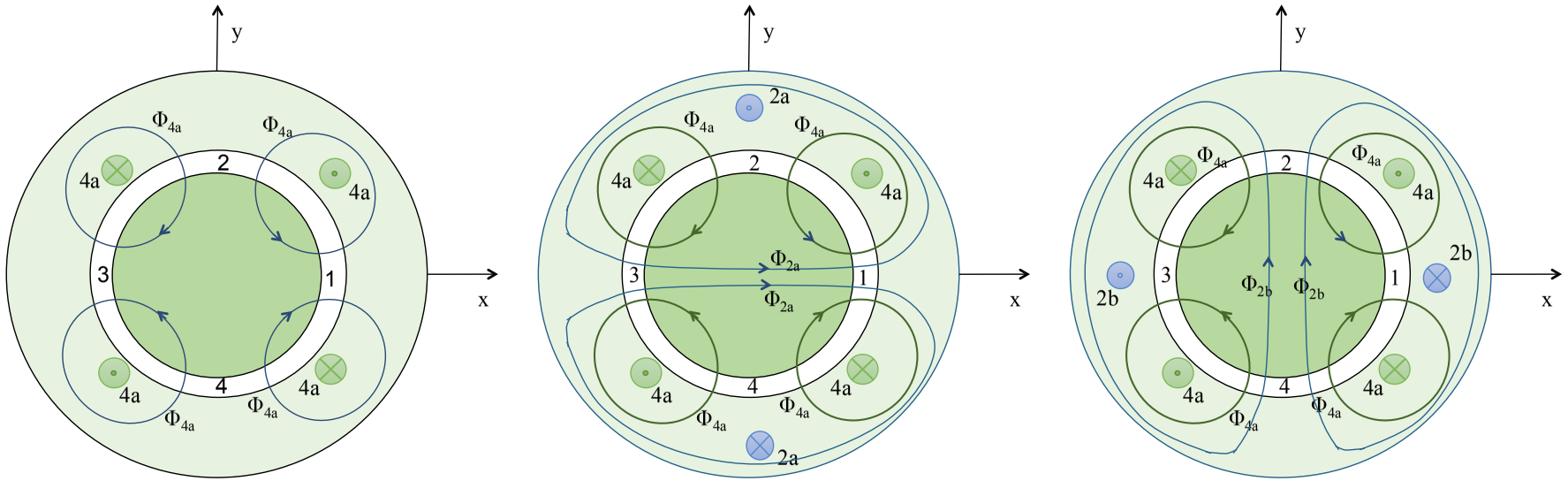

Figure 4-1: principles of radial suspension force generation. (a) 4-pole symmetrical flux; (b) x-direction radial suspension force generation; (c) y-direction radial suspension force generation.

ductors $2a$ are located in the stator slots. With the current directions shown in the figure, a 2-pole flux wave Φ_{2a} is generated. Under this condition, the flux density is increased in air gap 1 because the direction of the 4-pole fluxes and the 2-pole fluxes are the same. However, in air gap 3 the flux density is decreased since the direction of these two fluxes is opposite. The amplitude of the magnetic forces in the air gap 1 and 3 are no longer equal. Instead, the force in air gap 1 is greater than the force in air gap 3. Hence a radial force is generated on the rotor in the x-direction. Reversing the current direction in the 2a windings reverses the direction of this force. It follows that the amplitude of the radial force increases as the current value in the 2a winding increases.

Figure 4-1 (c) shows the radial suspension force generation in the y-direction. Two conductors 2b, which is the other phase of the assumed 2-phase-2-pole winding, generates a two-pole flux centering at the y-axis as shown. Similarly, a flux density imbalance occurs, but this time trading between air gap 4 and air gap 2, hence producing a radial force on the rotor to the y-direction. The polarity of the 2-pole current will dictate the direction of the force, and the amplitude of the 2-pole current can control the force amplitude.

These are the principles of the radial suspension force generation in x- and y-directions. A vector sum of the two radial forces can produce a radial suspension force in any direction, and the suspension force amplitude is approximately proportional to the current in the 2-pole suspension control windings. With only the 4-pole motor windings excited, an destabilizing radial force will act on the rotor if the rotor is not perfectly centered. Thus the suspension force is needed to compensate this instability and thus make sure that the rotor stays in the center. Feedback control is required in this process. In the next section, the modeling of the bearingless motor is presented in detail.

4.2 Bearingless motor system modeling and analysis

In this section a complete mathematical model of the lateral suspension of the reaction sphere by means of a bearingless motor is derived. This derivation of the air gap permeance distribution and the inductance matrix are based on the analysis by Chiba in [24]. Our contribution in this derivation are the modeling of the negative stiffness of a bearingless motor and further deriving the transfer function of a bearingless motor system, which provide a reliable basis for the controller design of the lateral suspension system. This modeling process is also suitable for a general electrical motor with magnetic or mechanical bearings. We also verified the model with experimentally measured data from the 1D-MSRS.

In the derivation in this section, we assume the spherical rotor's motion in the vertical direction is small, and that this axis is independently controlled by the levitation electromagnet introduced in the previous chapter. With this assumption, the bearingless motor for the reaction sphere is reduced to a cylindrical motor, and the motor length is the length of the stator. In addition, for the sake of simplicity, a 2-phase excitation is assumed in the analysis without loss of generality. This analysis can be easily changed to a 3-phase system actually used in the experiment by performing a coordinate transformation, which is introduced in Section 4.3.2.

In this modeling process, the derivation of MMF and air gap variation of the bearingless motor system is presented in Section 4.2.1. The derivation of the magnetic flux distribution is given in Section 4.2.2. The derivation of the unstable radial force and further the negative stiffness of the bearingless motor system is presented in Section 4.2.3. The derivation of the induction matrix and further the force constants for the radial suspension in bearingless motor systems are presented in Section 4.2.4. Finally, the transfer function of the lateral suspension of a bearingless motor is derived in Section 4.2.5.

4.2.1 MMF and airgap variation

In this section, the magneto-motive force (MMF) distribution in a bearingless motor system and the permeance variations caused by air gap length variation due to x-y rotor displacements are derived to provide a basis for the modeling in further sections. In this derivation, the following assumptions are made:

- The spatial distribution of the magneto-motive force (MMF) is approximated as its sinusoidal fundamental component.
- The air gap permeance distribution is smooth. Thus stator slot harmonics are neglected.
- The magnetic reluctance of the iron core and rotor are negligible. That is, their magnetic permeability is infinite. The rotor's magnetic hysteresis is not considered in this analysis for the lateral suspension.
- Lateral eccentric rotor displacements are small with respect to the air gap length between the rotor surface and stator inner surface. This displacement is also assumed small compared to the rotor radius.

Figure 4-2 shows the winding arrangement for the bearingless motor being analyzed. Two sets of 2-phase windings are wound on the stator: the 4-pole windings are 4a and 4b and the 2-pole windings are 2a and 2b. The positive current directions of each winding are shown by the crosses and dots in the figure. Note that the current in the 2-pole windings are arranged such that the MMF directions are aligned on the x and y axis directions respectively. The 4a winding is arranged so that the MMF direction in air gap 1 is also aligned to the x-axis, and 4b winding is arranged to be perpendicular to the 4a winding in electrical terms with a phase-lead angle of 90 electrical degrees in the counter-clockwise direction. If sinusoidal and cosinusoidal currents with an electrical frequency of 2ω are supplied to the 4-pole windings, then a magnetic field, revolving in a counter-clockwise direction with mechanical frequency ω, is generated. A similar field distribution is generated by the 2-pole windings, but

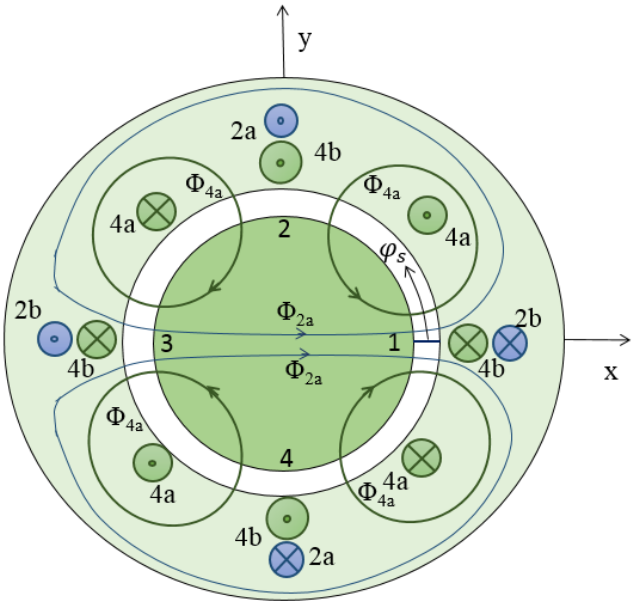

Figure 4-2: 4-pole and 2-pole winding arrangement of bearingless motor assuming a 2-phase configuration. The real hardware of 1D-MSRS is implimented with a 3-phase configuration.

for 2-pole field generation the electrical frequency and the mechanical frequency are equal. The flux lines in Figure 4-2 shows the case for a point in time when there are positive currents in 2a and 4a and zero current in 2b and 4b.

Let us assume the instantaneous currents that flow in the windings 4a, 4b, 2a and 2b are i_{4a}, i_{4b}, i_{2a} and i_{2b} respectively, and assume N_4 and N_2 are the numbers of turns per phase per pole of the 4-pole and 2-pole windings respectively. In the following we calculate the fundamental component of the MMF wave distribution of all windings.

Figure 4-3 shows the MMF wave that is generated by the winding 2a and its fundamental component. In the figure, the horizontal axis corresponds to the angular coordinate ϕ_s in Figure 4-2, which is a counter-clockwise rotational angular position starting from the x-axis. We also can think of this as stretching the cylindrical motor into a linear one. The positive direction of MMF, which generates air gap fluxes in the same direction, is defined in the radial direction from the rotor to the stator. With concentrated conductors 2a at $\phi_s = \frac{\pi}{2}$ and $\frac{3\pi}{2}$, the MMF distribution is a square wave

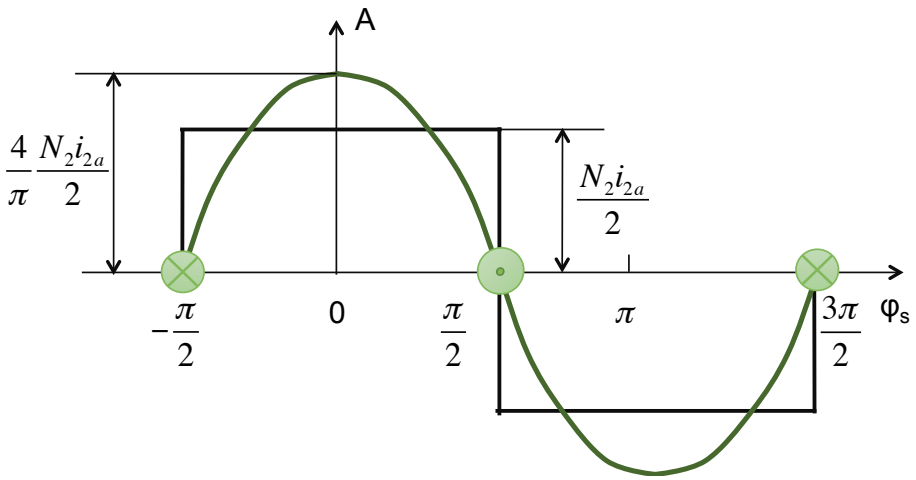

Figure 4-3: The MMF distribution generated by the winding 2a. The horizontal axis is the spatial angle ϕ_s. The black line shows the MMF of a concentrated winding, which is a square wave of $\frac{N_2 i_{2a}}{2}$ amplitude. The dark green line shows the fundamental component of the MMF, with an amplitude of $\frac{2N_2 i_{2a}}{\pi}$.

of amplitude $\frac{1}{2}N_2 i_{2a}$. By neglecting all the higher order harmonics of this MMF wave and only considering its fundamental component, we can calculate the magnitude of the approximated sinusoidal MMF wave, which is the first Fourier coefficient of the square wave, as shown in the Figure 4-3. For more detailed derivation of the harmonic analysis of electric motors see Fitzgerald and Kingsley [25]. Following this approach, the sinusoidal MMF space distributions for all the four windings can be written as

$$\mathcal{F}_{4a} = \frac{2}{\pi} N_4 i_{4a} cos(2\phi_s) \tag{4.1a}$$

$$\mathcal{F}_{4b} = \frac{2}{\pi} N_4 i_{4b} sin(2\phi_s) \tag{4.1b}$$

$$\mathcal{F}_{2a} = \frac{2}{\pi} N_2 i_{2a} cos(\phi_s) \tag{4.1c}$$

$$\mathcal{F}_{2b} = \frac{2}{\pi} N_2 i_{2b} sin(\phi_s). \tag{4.1d}$$

Here N_4 and N_2 are the numbers of turns per phase per pole of the 4-pole and 2-pole windings respectively. The angular coordinate ϕ_s is a counter-clockwise rotational angular position starting from the x-axis, as shown in Figure 4-2.

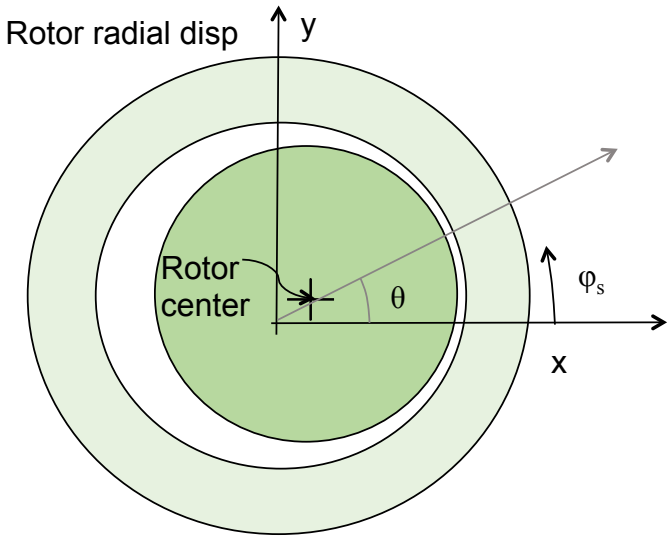

Figure 4-4: Air gap length variation with rotor eccentric displacement.

Figure 4-4 shows a rotor having an eccentric displacement from the stator center. The x-y coordinate is fixed to the stator center. The rotor center is displaced in the positive direction along the x and y axes. We define the nominal air gap length between the rotor and stator as g_0 when the rotor is centered in the stator bore. If the rotor's radial displacements are x and y in the corresponding directions, then the air gap length g between the rotor and the stator will become

$$g(\phi_s) = g_0 - xcos(\phi_s) - ysin(\phi_s). \tag{4.2}$$

To calculate the permeance of the air gap, the inverse of the air gap length distribution is needed. Based on the assumption that the displacements x and y are small compared to the nominal air gap length g_0, the inverse of the air gap length can be calculated by ignoring second and higher order terms in its Taylor expansion via

$$\begin{aligned}\frac{1}{g} &= \frac{1}{g}\bigg|_{x=0,y=0} - \left(-\frac{cos(\phi_s)}{g^2}\bigg|_{x=0,y=0}\right)x - \left(-\frac{sin(\phi_s)}{g^2}\bigg|_{x=0,y=0}\right)y + h.o.t. \\ &= \frac{1}{g_0}\left(1 + \frac{x}{g_0}cos(\phi_s) + \frac{y}{g_0}sin(\phi_s)\right) + h.o.t..\end{aligned}$$

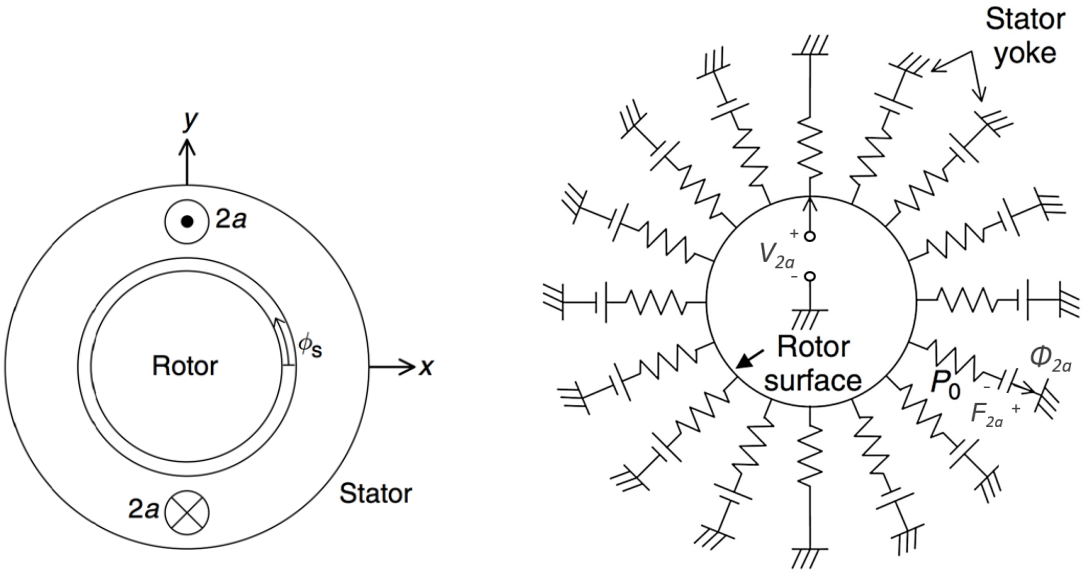

(a)Winding and coordinate diagram (b) Magnetic circuit model diagram.

Figure 4-5: Magnetic equivalent circuit of the bearingless motor with 2a winding current.

Then the magnetic permeance of the air gap P_0 at an angular position ϕ_s is given by

$$P_0(\phi_s) = \frac{\mu_0 Rl}{g} = \frac{\mu_0 Rl}{g_0}\left(1 + \frac{x}{g_0}cos(\phi_s) + \frac{y}{g_0}sin(\phi_s)\right). \tag{4.4}$$

Here R and l are the rotor radius and motor length respectively. For the reaction sphere, R is the sphere's radius, and the motor length l is the length of the stator iron.

4.2.2 Magnetic potential and flux distribution

In this section, the air gap flux distribution is derived using the MMF and air gap permeance distribution calculated above. Here we assume that the magnetic potential of the rotor is not zero because the flux distribution is unsymmetrical when a rotor has radial displacement.

Let us demonstrate the calculation of the air gap flux generated by the 2a windings first. Figure 4-5 shows a simplified magnetic circuit diagram for the bearingless motor

with only winding 2a excited. Figure 4-5 (a) shows the winding position and the coordinate system. Winding 2a is located in slots on the stator side. With current i_{2a} in this winding, we model that a space sinusoidal distribution of MMF is generated. Figure 4-5 (b) shows the magnetic circuit model of this system. The distributed reluctances represent the air gap, and their value distribution is the inverse of the air gap permeance given by (4.4). The reluctance values are not equal; they are dependent on the rotor radial displacement and angular position ϕ_s. In series with the air gap reluctances are DC voltage sources. These voltage sources represent the MMF of the winding 2a. The values of the voltage sources are also dependent on ϕ_s. The voltage value distribution the MMF distribution $\mathcal{F}_{2a}$ varies as given in (4.1d). The voltage sources are not included at $\phi_s = 90^o$ and 270^o because $\mathcal{F}_{2a}$ is zero at these two points. The ground symbols connected to the voltage sources indicate that the stator yoke magnetic potential is assumed to be zero.

The ring circuit that connects all air gap reluctances represents the rotor surface reluctance, which is assumed to be zero in this analysis. The voltage V_{2a} is the magnetic potential of the rotor generated by the current in winding 2a. The magnetic flux Φ_{2a} that goes through the permeance P_0 as a function of the angular position ϕ_s can then be written as

$$\Phi_{2a}(\phi_s) = P_0(\phi_s)\left(\mathcal{F}_{2a}(\phi_s) + V_{2a}\right). \tag{4.5}$$

According to the Gauss' law, taking a closed surface around the rotor, an integral of the flux through this surface should be zero, which means

$$\int_0^{2\pi} \Phi_{2a}(\phi_s)\mathrm{d}\phi_s = 0. \tag{4.6}$$

Substituting in (4.5) and (4.4) into (4.6), we can calculate the magnetic potential of the rotor induced by winding 2a as

$$V_{2a} = -\frac{\int_0^{2\pi} P_0\mathcal{F}_{2a}\mathrm{d}\phi_s}{\int_0^{2\pi} P_0\mathrm{d}\phi_s} = -\frac{N_2 i_{2a}}{\pi g_0}x. \tag{4.7}$$

Equation (4.8) implies that the magnetic potential of the rotor is zero if the rotor is centered, and when there is an eccentric displacement, the magnetic potential produced by the 2a winding V_{2a} is proportional to the rotor displacement in x-direction. Note that the variable y does not appear in the expression of V_{2a}, since the conductors of 2a windings are configured at $\phi_s = 90^o$ and 270^o, hence this winding cannot influence the field in y-direction.

Similarly, we can calculate the rotor magnetic potential induced by all sets of windings 2a, 2b, 4a, 4b as

$$V_{2a} = -\frac{N_2 i_{2a}}{\pi g_0} x \tag{4.8a}$$

$$V_{2b} = -\frac{N_2 i_{2b}}{\pi g_0} y \tag{4.8b}$$

$$V_{4a} = 0 \tag{4.8c}$$

$$V_{4b} = 0. \tag{4.8d}$$

Notice that the calculation results of V_{4a} and V_{4b} are zero and not depend on the rotor radial displacement. This can be simply explained by way of example: 2a in (4.8) is substituted by 4a, which is a periodic function of $2\phi_s$. The air gap permeance given in (4.4) is a periodic function of ϕ_s; therefore the integration of this product is zero.

Substituting the derived rotor magnetic potential value V_{2a} in (4.8) into (4.5), we can calculate that when the winding 2a is excited by current i_{2a}, the generated air gap flux resulting from winding 2a has a distribution of

$$\Phi_{2a}(\phi_s) = P_0(\phi_s) \left(\mathcal{F}_{2a}(\phi_s) - \frac{N_2 i_{2a}}{\pi g_0} x \right). \tag{4.9}$$

Similarly, when windings 2b, 4a and 4b are excited by the corresponding currents separately, the generated air gap magnetic flux distributions are

$$\Phi_{2b}(\phi_s) = P_0(\phi_s)\left(\mathcal{F}_{2b}(\phi_s) - \frac{N_2 i_{2b}}{\pi g_0} y\right) \tag{4.10a}$$

$$\Phi_{4a}(\phi_s) = P_0(\phi_s)\mathcal{F}_{4a}(\phi_s) \tag{4.10b}$$

$$\Phi_{4b}(\phi_s) = P_0(\phi_s)\mathcal{F}_{4b}(\phi_s). \tag{4.10c}$$

Here $P_0(\phi_s)$ is the air gap permeance distribution given in (4.4). $\mathcal{F}_{2a}$, $\mathcal{F}_{2b}$, $\mathcal{F}_{4a}$ and $\mathcal{F}_{4b}$ are the MMF distributions generated by the corresponding winding excitations, whose values are given in (4.1). Notice that in these air gap flux distributions the air gap permeance P_0 is a common factor, while the MMF distributions terms and the terms that related to the rotor displacements are linear to the corresponding current amplitudes. As a result, a flux distribution generated with several windings excited together can be expressed as a linear combination of the flux distributions generated by the windings separately.

4.2.3 Negative stiffness of lateral levitation system

This section introduces the calculation of the radial destabilization force on the rotor when only the motor windings, in this analysis the 4-pole windings, are excited. When an electrical motor is operating, the motor windings are driven by symmetric AC currents to generate a rotating magnetic field and further generate a torque to the rotor. Under this condition, the rotor is unstable in the radial directions since radial forces are generated to the rotor at the magnetic poles to the same direction with the rotor displacements. In this section we calculate this destabilization radial force and further find the "negative stiffness" of the lateral levitation plant of bearingless motor. This value will be used in the derivation of the plant transfer function in the lateral suspension control loop. This calculation can also be extended to other electrical machines with separate magnetic or mechanical bearings.

In the design 1D-MSRS, the 4-pole windings are the motor winding. When the motor operating under DC excitations, the 4-pole windings are excited by co-sinusoidal

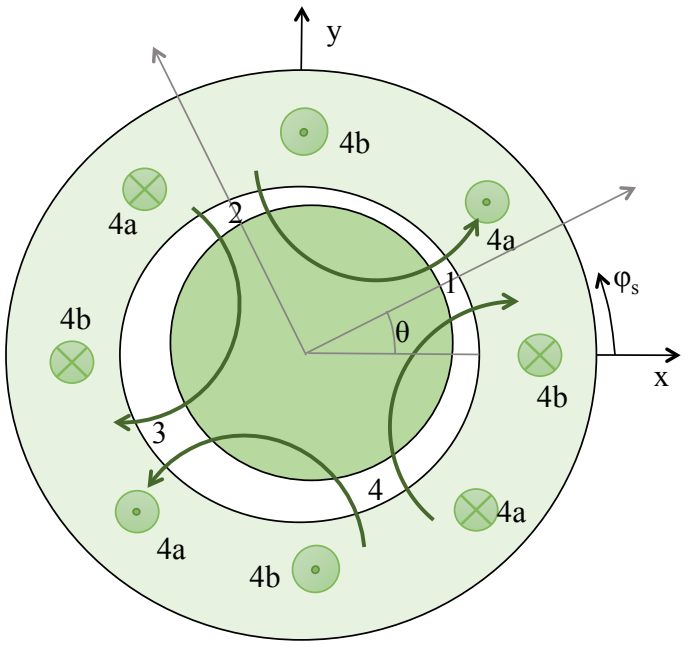

Figure 4-6: Unstable radial force generation with only the motor windings (4-pole windings) excited. Attractive forces are generated in the air gaps 1, 2, 3, and 4. The rotor has an eccentric displacement s towards the air gap 1 direction, which induces a radial force in this direction.

and sinusoidal distributed currents as

$$i_{4a} = I_4 \ \cos(2\theta) \tag{4.11a}$$

$$i_{4b} = I_4 \ \sin(2\theta). \tag{4.11b}$$

Here I_4 is the peak amplitude for the 2-phase excitation current, and θ is a fixed spatial angle, indicating the angular position of the magnetic poles. With the 4-pole windings being excited by the current above, sinusoidal MMF distributions along the stator is generated as

$$\mathcal{F}_{4a} = \frac{2}{\pi} N_4 I_4 \cos(2\theta)\cos(2\phi_s) \tag{4.12a}$$

$$\mathcal{F}_{4b} = \frac{2}{\pi} N_4 I_4 \sin(2\theta)\sin(2\phi_s). \tag{4.12b}$$

Note that in (4.12) the angle θ is fixed, while ϕ_s is the angular coordinate that starting from x-axis. With the MMF distribution given in (4.12), 4 magnetic poles will be generated on the rotor at $\phi_s = \theta$, $\phi_s = \theta + 90^o$, $\phi_s = \theta + 180^o$ and $\phi_s = \theta + 270^o$, as shown in Figure 4.23. Unstable attractive magnetic forces between the rotor and the stator iron are generated at these positions, so that the rotor's eccentric displacement driven by this force is more likely towards one of these directions. In this analysis, let us assume the rotor's eccentric displacement is toward the direction of $\phi_s = \theta$ without loss of generality. We define the length of the displacement of the rotor to be s. Hence the rotor's displacement in x- and y-directions are

$$x = s \ \cos(\theta) \tag{4.13a}$$

$$y = s \ \sin(\theta). \tag{4.13b}$$

Here we assume that the rotor's displacement s is small comparing to the nominal air gap length g_0. Then the air gap permeance distribution can be calculated by substituting (4.13) into (4.4) as

$$P_0(\phi_s) = \frac{\mu_0 R l}{g_0} \left(1 + \frac{s}{g_0} \cos(\theta)\cos(\phi_s) + \frac{s}{g_0} \sin(\theta)\sin(\phi_s) \right). \tag{4.14}$$

Based on the results derived in the previous section, the rotor's magnetic potential keeps zero when there is only 4-pole excitation in the system, despite the existence of rotor eccentric displacement. With both the MMF distribution and the air gap permeance distribution identified, the magnetic flux in the air gap that generated by the 4a windings can then be calculated as

$$\begin{aligned} \Phi_{4a}(\phi_s) &= P_0(\phi_s) \cdot \mathcal{F}_{4a}(\phi_s) \\ &= \frac{\mu_0 R l}{g_0} \left(1 + \frac{s}{g_0} \cos(\theta)\cos(\phi_s) + \frac{s}{g_0} \sin(\theta)\sin(\phi_s) \right) \cdot \frac{2}{\pi} N_4 I_4 \cos(2\theta)\cos(2\phi_s). \end{aligned} \tag{4.15}$$

Similarly, the air gap flux induced by 4b winding is

$$\begin{aligned}\Phi_{4b}(\phi_s) &= P_0(\phi_s)\cdot\mathcal{F}_{4b}(\phi_s)\\ &= \frac{\mu_0 Rl}{g_0}\left(1+\frac{s}{g_0}\cos(\theta)\cos(\phi_s)+\frac{s}{g_0}\sin(\theta)\sin(\phi_s)\right)\cdot\frac{2}{\pi}N_4 I_4\sin(2\theta)\sin(2\phi_s).\end{aligned} \tag{4.16}$$

The total flux distribution that generated by the 4-pole windings can be achieved by adding the two flux distributions in (4.15) and (4.16) together as

$$\Phi_4(\phi_s) = \frac{\mu_0 Rl}{g_0}\left(1+\frac{s}{g_0}\cos\theta\cos\phi_s+\frac{s}{g_0}\sin\theta\sin\phi_s\right)\cdot\frac{2N_4 I_4}{\pi}\left(\cos(2\theta)\cos(2\phi_s)+\sin(2\theta)\sin(2\phi_s)\right). \tag{4.17}$$

In the following derivation, the radial force between the rotor and the stator iron is calculated by means of the Maxwell stress tensor method. Based on the assumption that the magnetic flux in the air gap is in the radial direction (this is not true when the motor is running), we can use the formula $F=\frac{B_4^2}{2\mu_0}$ to calculate the force per unit area between the rotor and the stator in the radial direction, where B_4 is the air gap flux density generated by 4-pole excitations. The area between the stator and the rotor per unit radian is Rl. For the reaction sphere, R is the rotor's radius, and l is the length of the stator. Based on these results, we can calculate the force in the half-circle on the air gap 1 side (shown in Figure 4.23) to the direction of $\phi_s=\theta$ as:

$$\begin{aligned}f_+ &= \int_{\theta-\frac{\pi}{2}}^{\theta+\frac{\pi}{2}} Rl\frac{B_4^2}{2\mu_0}\cos(\phi_s-\theta)\mathrm{d}\phi_s\\ &= \int_{\theta-\frac{\pi}{2}}^{\theta+\frac{\pi}{2}} \frac{\Phi_4^2}{2Rl\mu_0}\cos(\phi_s-\theta)\mathrm{d}\phi_s.\end{aligned} \tag{4.18}$$

Substitute (4.17) into (4.18), we can calculate the force as

$$
\begin{aligned}
f_+ =& \frac{1}{2Rl\mu_0}\int_{\theta-\frac{\pi}{2}}^{\theta+\frac{\pi}{2}} \left(\frac{2\mu_0 RlN_4I_4}{\pi g_0}\right)^2 \left(1+\frac{s}{g_0}\cos\theta\cos\phi_s+\frac{s}{g_0}\sin\theta\sin\phi_s\right)^2 \\
& \left(\cos(2\theta)\cos(2\phi_s)+\sin(2\theta)\sin(2\phi_s)\right)^2\cos(\phi_s-\theta)\mathrm{d}\phi_s \\
=& \frac{2\mu_0 RlN_4^2I_4^2}{\pi^2 g_0^2}\left(\frac{76s^2}{105g_0^2}+\frac{\pi s}{2g_0}+\frac{14}{15}\right).
\end{aligned}
\tag{4.19}
$$

Note that the force f_+ has no dependency on the angle θ due to the symmetry of motor. Similarly, the flux in the half circle of the air gap 3 side generates a force toward the direction of $\phi_s = \theta + 180^o$ on the rotor. This force can be calculated as

$$
\begin{aligned}
f_- &= \int_{\theta+\frac{\pi}{2}}^{\theta+\frac{3\pi}{2}} Rl\frac{B_4^2}{2\mu_0}\cos(\phi_s-\pi-\theta)\mathrm{d}\phi_s \\
&= \int_{\theta+\frac{\pi}{2}}^{\theta+\frac{3\pi}{2}} \frac{\Phi_4^2}{2Rl\mu_0}\cos(\phi_s-\pi-\theta)\mathrm{d}\phi_s.
\end{aligned}
\tag{4.20}
$$

Substitute the expression of flux distribution into (4.20), we can calculate the value of f_- as

$$
\begin{aligned}
f_- =& \frac{1}{2Rl\mu_0}\int_{\theta+\frac{\pi}{2}}^{\theta+\frac{3\pi}{2}} \left(\frac{2\mu_0 RlN_4I_4}{\pi g_0}\right)^2 \left(1+\frac{s}{g_0}\cos\theta\cos\phi_s+\frac{s}{g_0}\sin\theta\sin\phi_s\right)^2 \\
& \left(\cos(2\theta)\cos(2\phi_s)+\sin(2\theta)\sin(2\phi_s)\right)^2\cos(\phi_s-\pi-\theta)\mathrm{d}\phi_s \\
=& \frac{2\mu_0 RlN_4^2I_4^2}{\pi^2 g_0^2}\left(\frac{76s^2}{105g_0^2}-\frac{\pi s}{2g_0}+\frac{14}{15}\right).
\end{aligned}
\tag{4.21}
$$

The total radial force that acting on the rotor towards the direction of $\phi_s = \theta$, which is also the direction of the rotor's incremental displacement, can be calculated as

$$
\begin{aligned}
f = f_+ - f_- =& \frac{2\mu_0 R l N_4^2 I_4^2}{\pi^2 g_0^2} \cdot \frac{\pi s}{g_0} \\
=& \frac{2\mu_0 R l N_4^2 I_4^2}{\pi g_0^3} \cdot s.
\end{aligned}
\tag{4.22}
$$

The above equation demonstrates the relationship between the radial force f generated by the motor windings and the eccentric displacement of the rotor s. This relation resembles the force and motion relation of a spring: the force is proportional to the length (displacement). However, different from a mechanical spring, as the displacement increases, the force produced by this "spring" tends to make the displacement even larger, making the rotor unstable in the center of the stator bore. Let us define the coefficient in (4.22) to be the **Negative Stiffness** of this bearingless motor:

$$
K_s = \frac{2\mu_0 R l N_4^2 I_4^2}{\pi g_0^3}. \tag{4.23}
$$

Therefore the total radial force acting on the rotor is $f = K_s \cdot s$.

Similar to the single degree-of-freedom magnetic suspension system that we studied in the previous chapter, the lateral magnetic suspension of the reaction sphere in the bearingless motor system has a transfer function of the same form. This negative stiffness value will be used to develop the plant transfer function of the sphere's lateral suspension system.

4.2.4 Force constant of the lateral levitation system

In this section, the motor inductance matrix is derived first using the air gap flux distributions found in the Section 4.2.2. Some elements of the inductance matrix are shown to be a function of the rotor's radial displacement. Then the suspension forces in the bearingless motor are derived by taking partial derivatives of the stored magnetic energy, where the magnetic energy is calculated from the inductance functions. From this calculation we can find the force constant of the suspension forces

generation in a bearingless motor system, which is also a key element of forming the transfer function of the lateral magnetic suspension system.

We continue to analyze the 2-phase 4-pole 2-pole bearingless motor. Assume that the flux linkages of the winding 2a, 2b, 4a, and 4b are λ_{2a}, λ_{2b}, λ_{4a} and λ_{4b} respectively, and the instantaneous currents in these windings are i_{2a}, i_{2b}, i_{4a} and i_{4b}. Then the flux linkage and current relationships can be expressed in a matrix form as

$$\begin{bmatrix} \lambda_{4a} \\ \lambda_{4b} \\ \lambda_{2a} \\ \lambda_{2b} \end{bmatrix} = \begin{bmatrix} L_{4a4a} & M_{4a4b} & M_{4a2a} & M_{4a2b} \\ M_{4a4b} & L_{4b4b} & M_{4b2a} & M_{4b2b} \\ M_{4a2a} & M_{4b2a} & L_{2a2a} & M_{2a2b} \\ M_{4a2b} & M_{4b2b} & M_{2a2b} & L_{2b2b} \end{bmatrix} \cdot \begin{bmatrix} i_{4a} \\ i_{4b} \\ i_{2a} \\ i_{2b} \end{bmatrix}. \tag{4.24}$$

The inductances defined in the above matrix can be derived by integration of the product of air gap flux under unity current excitation and the according MMF distribution under unity current excitation such that

$$L_{4a} = \int_0^{2\pi} \Phi_{4a}(\phi_s)\Big|_{i_{4a}=1} \mathcal{F}_{4a}(\phi_s)\Big|_{i_{4a}=1} d\phi_s \tag{4.25a}$$

$$L_{4b} = \int_0^{2\pi} \Phi_{4b}(\phi_s)\Big|_{i_{4b}=1} \mathcal{F}_{4b}(\phi_s)\Big|_{i_{4b}=1} d\phi_s \tag{4.25b}$$

$$M_{4a4b} = \int_0^{2\pi} \Phi_{4b}(\phi_s)\Big|_{i_{4b}=1} \mathcal{F}_{4a}(\phi_s)\Big|_{i_{4a}=1} d\phi_s \tag{4.25c}$$

$$L_{2a} = \int_0^{2\pi} \Phi_{2a}(\phi_s)\Big|_{i_{2a}=1} \mathcal{F}_{2a}(\phi_s)\Big|_{i_{2a}=1} d\phi_s \tag{4.25d}$$

$$L_{2b} = \int_0^{2\pi} \Phi_{2b}(\phi_s)\Big|_{i_{2b}=1} \mathcal{F}_{2b}(\phi_s)\Big|_{i_{2b}=1} d\phi_s \tag{4.25e}$$

$$M_{2a2b} = \int_0^{2\pi} \Phi_{2a}(\phi_s)\Big|_{i_{2a}=1} \mathcal{F}_{2b}(\phi_s)\Big|_{i_{2b}=1} d\phi_s \tag{4.25f}$$

$$M_{4a2a} = \int_0^{2\pi} \Phi_{2a}(\phi_s)\Big|_{i_{2a}=1} \mathcal{F}_{4a}(\phi_s)\Big|_{i_{4a}=1} d\phi_s \tag{4.25g}$$

$$M_{4b2a} = \int_0^{2\pi} \Phi_{2a}(\phi_s)\Big|_{i_{2a}=1} \mathcal{F}_{4b}(\phi_s)\Big|_{i_{4b}=1} d\phi_s \tag{4.25h}$$

$$M_{4a2b} = \int_0^{2\pi} \Phi_{2b}(\phi_s)\Big|_{i_{2b}=1} \mathcal{F}_{4a}(\phi_s)\Big|_{i_{4a}=1} d\phi_s \tag{4.25i}$$

$$M_{4b2b} = \int_0^{2\pi} \Phi_{2b}(\phi_s)\Big|_{i_{2b}=1} \mathcal{F}_{4b}(\phi_s)\Big|_{i_{4b}=1} d\phi_s. \tag{4.25j}$$

Here Φ_{4a}, Φ_{4b}, Φ_{2a} and Φ_{2b} are the air gap flux distribution given in (4.10), and $\mathcal{F}_{4a}$, $\mathcal{F}_{4b}$, $\mathcal{F}_{2a}$ and $\mathcal{F}_{2b}$ are the MMF distribution given in (4.1). Substituting their values into the above equation and solving the integrations results in a simple mathematical form. Denoting them in a matrix form we can get the following relations:

$$\begin{bmatrix} L_{4a} & M_{4a4b} \\ M_{4a4b} & L_{4b} \end{bmatrix} = \frac{4\mu_0 RlN_4^2}{\pi g_0} \begin{bmatrix} 1 & 0 \\ 0 & 1 \end{bmatrix} \tag{4.26}$$

$$\begin{bmatrix} L_{2a} & M_{2a2b} \\ M_{2a2b} & L_{2b} \end{bmatrix} = \frac{4\mu_0 RlN_2^2}{\pi g_0} \begin{bmatrix} 1 & 0 \\ 0 & 1 \end{bmatrix} \tag{4.27}$$

$$\begin{bmatrix} M_{4a2a} & M_{4a2b} \\ M_{4a2b} & M_{4b2b} \end{bmatrix} = \frac{2\mu_0 RlN_4N_2}{\pi g_0^2} \begin{bmatrix} x & -y \\ y & x \end{bmatrix}. \tag{4.28}$$

From the above-calculated results, we can see the following:

1. The self-inductances L_{4a}, L_{4b}, L_{2a} and L_{2b} are a product of air permeability, stator's axial length, rotor radius and winding turns of 4-pole motor winding, and the inverse of the air gap length.

2. The mutual inductance M_{4a4b} between the 4-pole windings is zero because windings 4a and 4b are perpendicular to each other. The same is true for M_{2a2b}.

3. The mutual inductances M_{4a2a}, M_{4b2a}, M_{4a2b} and M_{4b2b} represent the coupling between the 4-pole and 2-pole windings. These mutual inductances are proportional to the rotor radial displacements x and y.

4. These mutual inductances are zero when the rotor is positioned at the cen-

ter. This fact is easily understood because the 4-pole and 2-pole windings are symmetrically wound and are not coupled when the rotor is centered. If these inductances are zero, there is no induced voltage in the 2-pole winding when a 4-pole revolving magnetic field is generated. On the other hand, no induced voltage appears at the 4-pole terminals when the 2-pole winding current generates a 2-pole revolving magnetic field. Therefore the voltage requirement for the suspension winding is low when the rotor's eccentric displacement is small.

Suspension radial force is associated with the radial-displacement-dependent inductance terms in (4.28) because they represent an imbalance in stored magnetic energy in the air gap. Under the assumption of magnetic linearity, the derivatives (with respect to the radial displacement) of (4.28) are constant, producing constant radial force gains.

For simplicity, let us define a current vector as $[i] = [i_{4a}, i_{4b}, i_{2a}, i_{2b}]^T$, and denote the 4×4 inductance matrix in (4.24) to be $[L]$, which can be written as

$$[L] = \begin{bmatrix} L_4 & 0 & M'x & -M'y \\ 0 & L_4 & M'y & M'x \\ M'x & M'y & L_2 & 0 \\ -M'y & M'x & 0 & L_2 \end{bmatrix}. \tag{4.29}$$

Here L_4 and L_2 are constants, i.e., the self-inductances of 4-pole and 2-pole windings. M' is the coefficient of the mutual inductance in (4.28), that is $M' = \frac{2\mu_0 RlN_4N_2}{\pi g_0^2}$. Then the magnetic energy stored in the system is given by

$$W_m = \frac{1}{2}[i]^T[L][i]. \tag{4.30}$$

Expansion of the above equation results in

$$\begin{aligned} W_m =& \frac{1}{2}L_4 i_{4a}^2 + \frac{1}{2}L_4 i_{4b}^2 + \frac{1}{2}L_2 i_{2a}^2 + \frac{1}{2}L_2 i_{2b}^2 \\ &+ M'x i_{4a} i_{2a} - M'y i_{4a} i_{2b} + M'y i_{4b} i_{2a} + M'x i_{4b} i_{2b}. \end{aligned} \tag{4.31}$$

The first four terms represent the stored magnetic energy associated with the self-inductances. The last four terms are the energy terms of the mutual inductances between the 4-pole and 2-pole windings. The radial forces can be derived from the partial derivatives of the stored magnetic energy. Here we assume a magnetically linear system, where the co-energy is equal to the energy. Then the forces can be written as

$$\begin{bmatrix} F_x \\ \\ F_y \end{bmatrix} = \begin{bmatrix} \frac{\partial W_m}{\partial x} \\ \\ \frac{\partial W_m}{\partial y} \end{bmatrix}. \tag{4.32}$$

Substituting (4.28) and (4.31) into (4.32) yields a simple mathematical expression because the first row in (4.31) disappears since the first 4 terms are not functions of radial displacement:

$$\begin{bmatrix} F_x \\ \\ F_y \end{bmatrix} = M' \begin{bmatrix} i_{4a} i_{2a} & i_{4b} i_{2b} \\ \\ -i_{4a} i_{2b} & i_{4b} i_{2a} \end{bmatrix}. \tag{4.33}$$

Rewrite the above equation in a matrix form yields:

$$\begin{bmatrix} F_x \\ \\ F_y \end{bmatrix} = M' \begin{bmatrix} i_{4a} & i_{4b} \\ \\ i_{4b} & -i_{4a} \end{bmatrix} \begin{bmatrix} i_{2a} \\ \\ i_{2b} \end{bmatrix}. \tag{4.34}$$

where M' is the mutual inductance factor between the 2-pole and 4-pole windings. When the 4-pole windings are the motor windings, it is driven with symmetical co-sinusoidal and sinusoidal excitation. At one time instant, the currents in the 4-pole winding can be written as

$$i_{4a} = I_4 \; cos(2\theta) \tag{4.35a}$$

$$i_{4b} = I_4 \; sin(2\theta). \tag{4.35b}$$

Here I_4 is the peak amplitude for the 2-phase excitation current, and θ is a the angular position of the magnetic pole. Then the suspension force in (4.34) can be written as

$$\begin{bmatrix} F_x \\ \\ F_y \end{bmatrix} = M' \begin{bmatrix} I_4 cos(2\theta) & I_4 sin(2\theta) \\ \\ I_4 sin(2\theta) & -I_4 cos(2\theta) \end{bmatrix} \begin{bmatrix} i_{2a} \\ \\ i_{2b} \end{bmatrix} \tag{4.36}$$

This is the expression of the suspension radial force when the magnetic pole is at $\phi_s = \theta$, and the coefficient in (4.36) demonstrates the **force constant** of the lateral suspension force generation. This equation tells us that the radial suspension force is approximately linear to the suspension winding current, which is often regarded as the control input of the lateral suspension system in a bearingless motor. This is a result of the "hard linearization" design of the device. In the bearingless motor system is an example of the flux steering design, where the current in the two-pole windings are steering the flux generated by the 4-pole windings. As a result, the current to suspension force is approximately linear. Reference [18] introduced the concept of the flux steering device design in detail.

The lateral suspension force that calculated above will be used to derive the plant transfer function model for the bearingless motor system for the reaction sphere in the next section.

4.2.5 Transfer function for bearingless motor system

In this section the transfer function of the lateral suspension in a bearingless motor system is calculated based on the negative stiffness and the force constant that we derived before. In this analysis, a DC excitation is assumed. It can be also viewed as a

time instant when the motor is under AC excitation. Since the system is symmetric, in this analysis let us restrict our attention to the lateral levitation system in the x-direction without loss of generality. This means we consider a time instant with $\theta = 0$, and the rotor's radial eccentric displacement is in the x-direction. Substituting $\theta = 0$ into (4.35), we can get the 2-phase-4-pole currents under this condition as

$$i_{4a} = I_4 \tag{4.37a}$$

$$i_{4b} = 0. \tag{4.37b}$$

Equation (4.37) shows that in this analysis only the 4a winding is excited with current I_4, and the 4b winding's current in zero. Similarly, substituting $\theta = 0$ into the analysis in Section 4.2.3, the rotor's displacement is $x = s$ and $y = 0$. Then the unstable radial force that generated only by the 4-pole windings is

$$f = K_s \cdot x. \tag{4.38}$$

This radial force is toward the x-direction, the same direction with the rotor's incremental displacement. The coefficient in this equation is the negative stiffness value $K_s = \frac{2\mu_0 RlN_4^2 I_4^2}{\pi g_0^3}$.

The suspension force can be calculated by substituting $\theta = 0$ into (4.36) as

$$\begin{bmatrix} F_x \\ \\ F_y \end{bmatrix} = M' \begin{bmatrix} I_4 & 0 \\ \\ 0 & -I_4 \end{bmatrix} \begin{bmatrix} i_{2a} \\ \\ i_{2b} \end{bmatrix}. \tag{4.39}$$

From this equation, we can see that the suspension force in x-direction is only related to the control current in 2a windings i_{2a}. Let us define the force constant in x-direction as $K_i = M' I_4$, and thus the suspension force in x-direction is $F_x = K_i \cdot i_{2a}$. Hence the total force acting on the rotor can be written as

$$\Sigma F_x = K_i \cdot i_{2a} + K_s \cdot x. \tag{4.40}$$

Let us define the mass of the rotor to be m. Then the dynamic equation of the rotor in the x-direction can be written as

$$\Sigma F_x = K_i \cdot i_{2a} + K_s \cdot x = m\ddot{x} \tag{4.41}$$

Applying the Laplace transform to the above equation, we can find the transfer function from the control current i_{2a} and output rotor displacement x as

$$\frac{X(s)}{I_{2a}(s)} = \frac{K_i}{ms^2 - K_s} \tag{4.42}$$

Note again the negative sign in front of K_s in this result. This implies the rotor is unstable in the center since the transfer function has a right plane pole, and feedback control is needed to stabilize this plant.

Although in this analysis only the x-direction is considered, we can use a rotational transformation to generalize the above analysis to any radial direction. We can also see that this transfer function is consistent with the dynamics of the single degree-of-freedom magnetic levitation system that we studied in the previous chapter, with both transfer functions exhibit negative stiffness in the suspension dynamics.

This section presents a complete mathematical model for the lateral suspension of the bearingless motor system. In the next section of this chapter, the reaction sphere hardware is related to the model we derived via a three-phase-to-two-phase transformation, and the model derived in this section is verified by the experimental data from the 1D-MSRS hardware.

4.3 Bearingless motor system in 1D-MSRS

In this section, the lateral suspension of the sphere in the 1D-MSRS system is studied with the model that we derived above. First the hardware design and the parameters are presented, and is related to the model that we derived in the previous section via a three-phase-to-two-phase coordinate transformation. Then the experimental test results of the lateral magnetic levitation of the reaction sphere are presented and

compared with the model.

4.3.1 Bearingless motor hardware

First let us present the design of the bearingless motor hardware design in the 1D-MSRS in detail. Figure 4-7 shows the winding pattern of the stator of the 1D-MSRS system. The stator has 24 slots. Two sets of 3-phase winding (4-pole and 2-pole) are distributed in the stator slots. Symbols 4u, 4v and 4w represents the 4-pole windings of phase u,v and w respectively. The same notation is used for the 2-pole windings.

In the 1D-MSRS design, the 4-pole windings are being used for commutation to reach a better torque ability, and the 2-pole windings are for levitation. Table 4.1 presents the parameters that describe the bearingless motor system for 1D-MSRS.

Table 4.1: Parameters for MSRS bearingless motor system

parameter	value
Rotor sphere radius	27 mm
Stator length	9.5 mm
Rotor mass	0.63 kg
Air gap length between stator and sphere (each side)	0.5 mm
Stator number of slots	24
Number of poles for motor winding	4
Number of wires per slot for motor winding	80
Number of poles for suspension winding	2
Number of wires per slot for suspension winding	40

Figure 4-8 shows a overall hardware configuration of the bearingless motor system in the reaction sphere design. The controller of the system is a PXI realtime target.

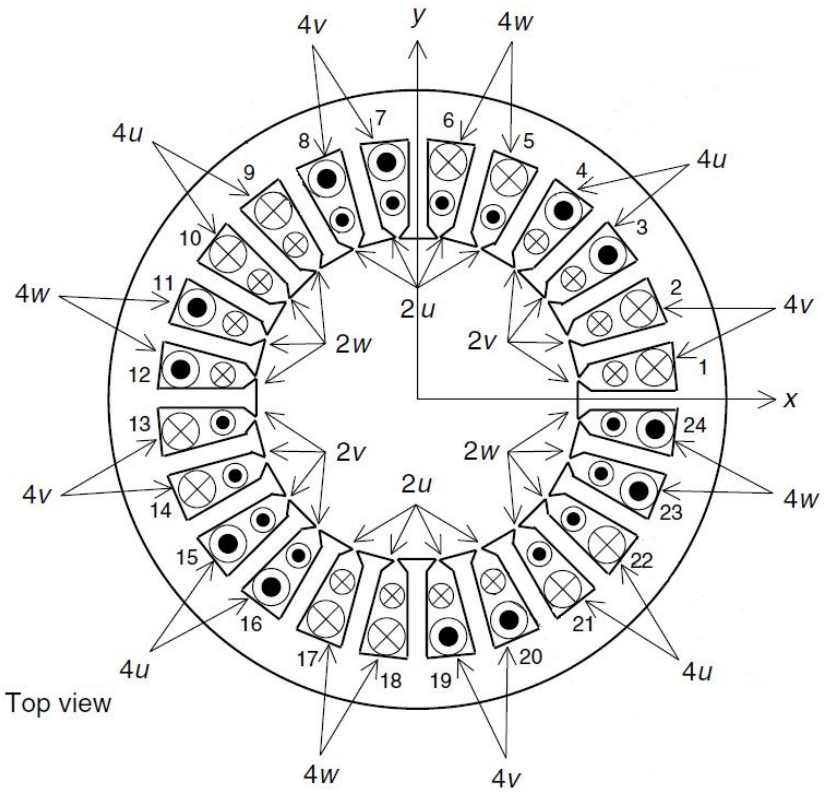

Figure 4-7: Multiple winding diagram for bearingless motor in 1-D MSRS. Winding 4u, 4v and 4w represents the 4-pole windings, and 2u, 2v and 2w represents the 2-pole windings. The two sets of windings are configured to be electrical orthogonal.

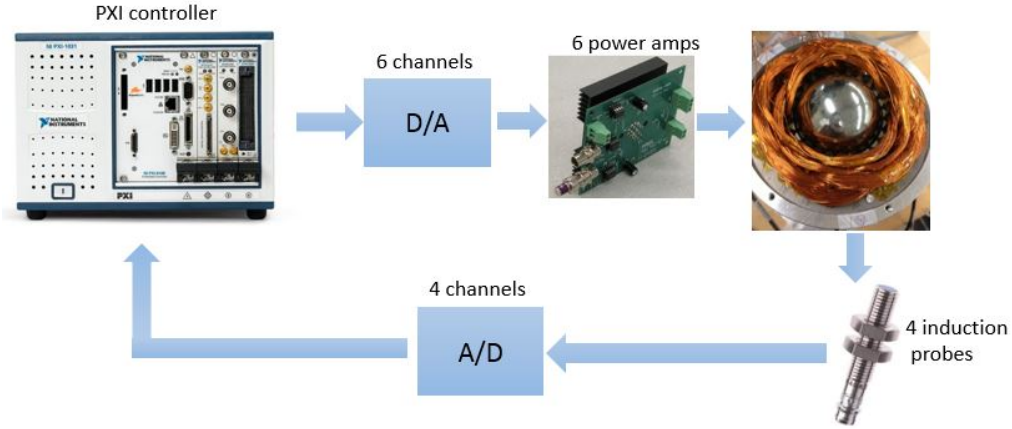

Figure 4-8: Overall hardware connection for the bearingless motor control system in reaction sphere's design.

It generates 6 current signals and goes into the current control amplifiers through the D/A converters. The amplified currents energize the 6 separated of windings in the reaction sphere system. The rotor's radial displacements in x- and y-directions are measured by 4 induction probes. The sensor signals goes into the controller through 4 channels of A/D converters. For more details of the hardware specifications see hardware description in Chapter 2.

4.3.2 Three phase system

This section considers the coordinate transformation that links the model of the bearingless motor that we derived in the previous section with the hardware implementation of the 1D-MSRS. Although a 2-phase system is being considered in the modeling for simplicity, 3-phase windings are usually used in real implementations. The 2-phase coordinate that used in the modeling can be readily transformed into 3-phase coordinates. The current relationships can be related to each other using a matrix transformation via

$$\begin{bmatrix} i_{4u} \\ \\ i_{4v} \\ \\ i_{4w} \end{bmatrix} = [C_{32}]^T \begin{bmatrix} i_{4a} \\ \\ i_{4b} \end{bmatrix}. \tag{4.43}$$

Here $[C_{32}]^T$ is the connection matrix given by

$$[C_{32}]^T = \frac{\sqrt{2}}{\sqrt{3}} \begin{bmatrix} 1 & 0 \\ \\ -\frac{1}{2} & \frac{\sqrt{3}}{2} \\ \\ -\frac{1}{2} & -\frac{\sqrt{3}}{2} \end{bmatrix}. \tag{4.44}$$

Similarly, using an inverse transformation we can also calculate the equivalent 2-phase currents from the symmetrical three-phase current values, that is

$$\begin{bmatrix} i_{4a} \\ \\ i_{4b} \end{bmatrix} = [C_{32}] \begin{bmatrix} i_{4u} \\ \\ i_{4v} \\ \\ i_{4w} \end{bmatrix}. \tag{4.45}$$

This transformation can link the reaction sphere system with a 3-phase implementation and the dynamic model of the bearingless motor's lateral suspension that we derived in before.

4.3.3 Model and measured transfer functions

In this section we study the lateral suspension of the reaction sphere under DC excitations. When the windings are excited with DC currents, there is no torque provided to the rotor. In this case the bearingless motor is working solely as an active magnetic bearing. Under DC excitations, the motor windings are driven by stationary three-phase current with a peak value of I_m. The subscript "m" means the motor winding current. By choosing the phase angle of the current in 4u winding to be zero, we can get the DC currents in the motor windings 4u, 4v and 4w as

$$i_{4u} = I_m \tag{4.46a}$$

$$I_{4v} = -\frac{1}{2} I_m \tag{4.46b}$$

$$I_{4w} = -\frac{1}{2} I_m. \tag{4.46c}$$

To link this design with the dynamic model of the bearingless motor's lateral suspension, let us perform the transformation from 3-phase to 2-phase to the above equations and reach a set of equivalent 2-phase currents of

$$i_{4a} = \frac{\sqrt{3}}{\sqrt{2}} I_m \tag{4.47a}$$

$$I_{4b} = 0. \tag{4.47b}$$

Thus the 2-phase equivalent peak current amplitude I_4 in the model is $I_4 = \frac{\sqrt{3}}{\sqrt{2}} I_m$.

From the data in Table 4.1, we know that the number of turns per pole per phase for the 4-pole winding N_4 is $80 \times 2 = 160$ turns. Rotor radius is $R = 27 \times 10^{-3}$ m. Motor length is $l = 9.5 \times 10^{-3}$ m. Substituting these parameters into the expression of the system's negative stiffness in (4.23) we can calculate its numerical value as

$$\begin{aligned} K_s &= \frac{2}{\pi} \frac{Rl\mu_0 N_4^2 I_4^2}{g_0^3} \\ &= \frac{2}{\pi} \frac{Rl\mu_0 N_4^2 (\sqrt{3}/\sqrt{2} I_m)^2}{g_0^3} = 7.29 \times 10^3 \cdot I_m^2 [N/m]. \end{aligned} \tag{4.48}$$

With the number of turns per phase per pole of the 2-pole winding $N_2 = 40 \times 4 = 160$ turns calculated, and a coefficient of $\frac{\sqrt{3}}{\sqrt{2}}$ is added to the system due to the transformation of the 2-pole currents from 3-phase to 2-phase, the force constant of the bearingless motor system of MSRS can be calculated as

$$\begin{aligned} K_i &= \frac{\sqrt{3}}{\sqrt{2}} \frac{2\mu_0 Rl N_2 N_4}{\pi g_0^2} I_4 \\ &= \frac{\sqrt{3}}{\sqrt{2}} \frac{2\mu_0 Rl N_2 N_4}{\pi g_0^2} (\frac{\sqrt{3}}{\sqrt{2}} I_m) = 31.74 \cdot I_m [N/A]. \end{aligned} \tag{4.49}$$

Here the value I_m is the zero-to-peak current amplitude of the 3-phase current in the 4-pole motor windings. With the above calculation we can figure out the transfer function of the lateral levitation system of the 1D-MSRS, with input of equivalent 2-phase 2-pole current i_{2a} and output x.

In the following let us compare the derived transfer function and the experimental measured Bode plot of the bearingless motor system. Figure 4-9 presents the mea-

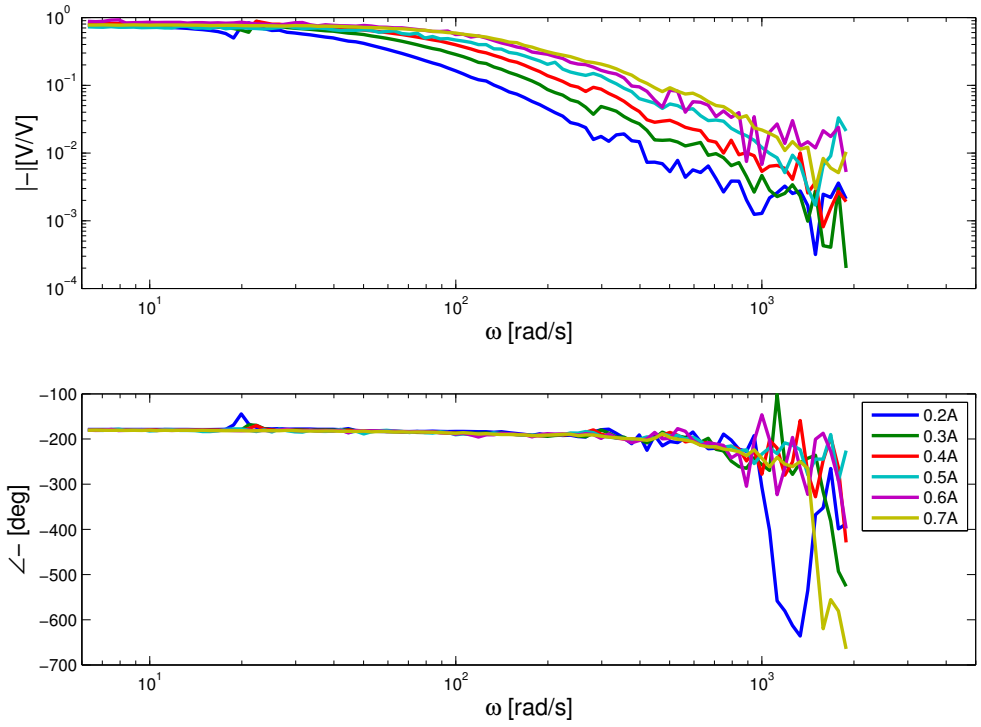

Figure 4-9: Experimentally measured plant frequency response for X direction sphere suspension from signal to amplifier[V] to position sensor output [V] under different 3-phase-4-pole excitation amplitude I_m (zero-to-peak). Note that plant dynamics are faster as I_m is increased.

sured plant Bode plot of the lateral levitation system of the 1D-MSRS under different motor winding current peak amplitude in 3-phase (I_m). Note that this measurement must be carried with the feedback control loop closed since the open-loop system of the sphere's lateral suspension is unstable.

From the measured frequency response data of the lateral suspension plant, we can see that the break frequency of the Bode plot is increasing as the 4-pole excitation current amplitude increases. This observation is consistent with the model, where the negative stiffness of the system K_s is proportional to the square of the 3-phase motor current amplitude I_m.

In the measurement of the frequency response, the signal we are applying is the command given to the current control amplifier, which has a amplifier gain of $g_{amp} =$ 0.1 A/V. The signal that we are measuring is the output signal of the sensors, which

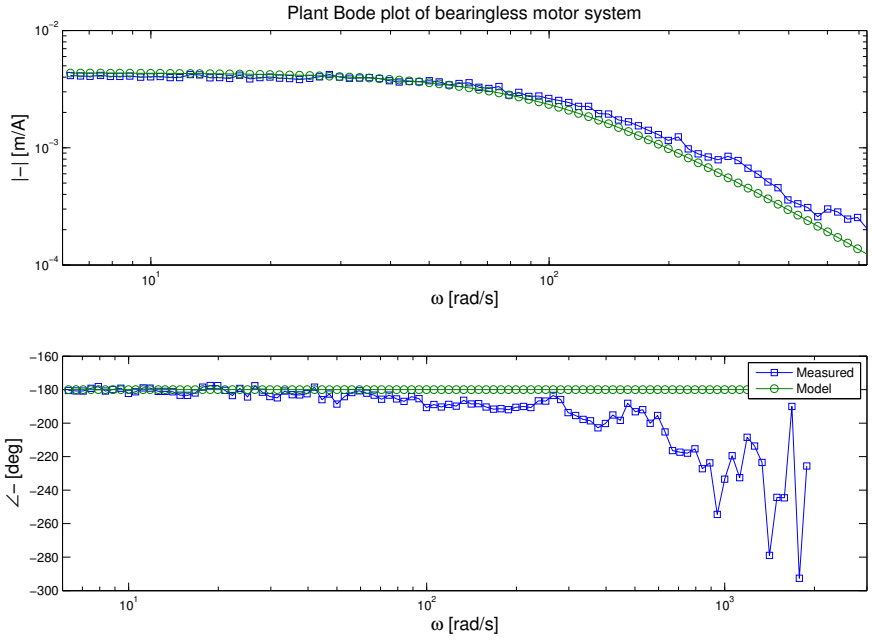

Figure 4-10: Measured and modeled plant frequency response of the lateral levitation system of 1D-MSRS from 2-pole winding current i_{2a} to sphere's position x. Green line: modeled plant transfer function. Blue: experimental measured plant transfer function. $I_m = 0.5$ A.

have a gain of $g_{sensor} = 1.25 \times \sqrt{2}$ V/mm. We can divide the measured magnitude of the plant Bode plot with this the total scaling gain to get the transfer function from i_{2a} to x.

Let us compare the transfer function that we calculated from the model and the experimental measured transfer function. Selecting $I_m = 0.5$ A, we can calculate the modeled plant transfer function from i_{2a} to x as

$$\begin{aligned} \left.\frac{X(s)}{I_{2a}(s)}\right|_{I_m=0.5\text{ A}} &= \left.\frac{K_i}{ms^2 - K_s}\right|_{I_m=0.5\text{ A}} \\ &= \frac{37.74}{0.63s^2 - 7290}\ [\text{m/A}]. \end{aligned} \tag{4.50}$$

Figure 4-10 plotted the modeled Bode plot of the transfer function in (4.50) and the measured frequency response data with $I_m = 0.5$ together. From the plot we can

see that the model matches with the measured data well. This comparison verifies the transfer function that we derived before.

4.4 Controller design and AC excitation

In this section the AC excitations of the bearingless motor system in 1D-MSRS and the controller design for lateral suspension are discussed.

4.4.1 AC excitation

First the AC excitation of the bearingless motor system is introduced in this section. In order to generate a torque to the rotor, three-phase AC currents are supplied to the motor winding of the bearingless motor for the 1D-MSRS to generate a revolving magnetic field. The symmetric three-phase current in the 4-pole winding can be written as

$$i_{4u} = I_m \times cos(2\omega t) \tag{4.51a}$$

$$i_{4v} = I_m \times cos(2\omega t + \frac{2\pi}{3}) \tag{4.51b}$$

$$i_{4w} = I_m \times cos(2\omega t + \frac{4\pi}{3}) \tag{4.51c}$$

For the simplicity of analysis, we first apply the transformation from three-phase to two-phase coordinate, as:

$$\begin{bmatrix} i_{4a} \\ \\ i_{4b} \end{bmatrix} = [C_{32}] \begin{bmatrix} i_{4u} \\ \\ i_{4v} \\ \\ i_{4w} \end{bmatrix} \tag{4.52}$$

where the $[C_{32}]$ matrix is given in (4.44). This transformation results in an equivalent two-phase AC current of:

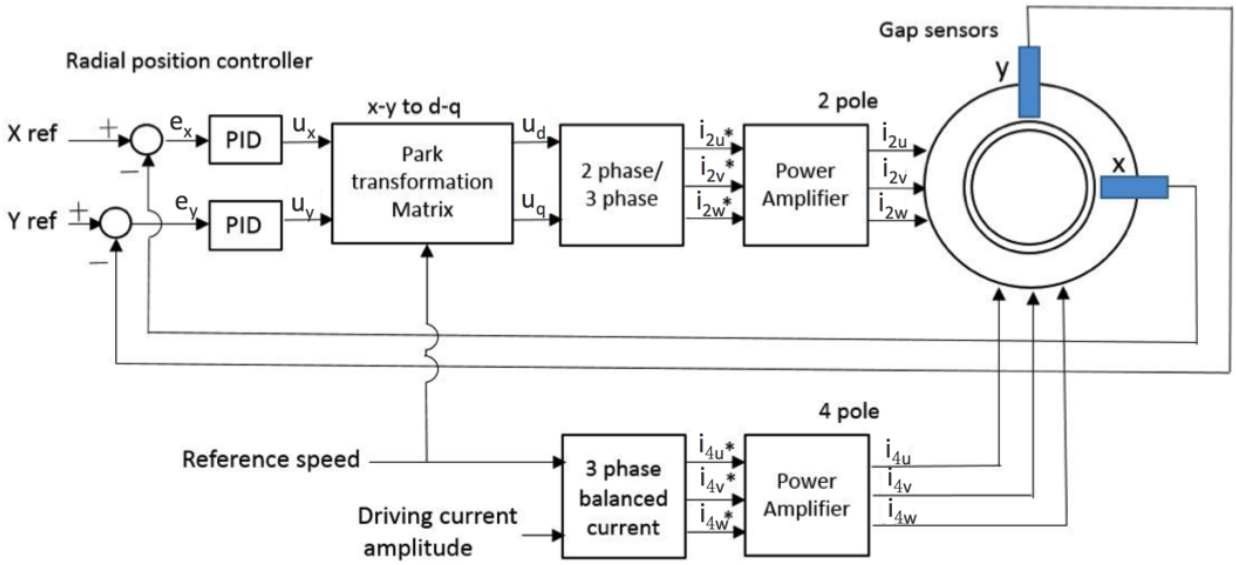

Figure 4-11: Diagram showing bearingless motor control approach under AC excitation.

$$i_{4a} = I_4 \times cos(2\omega t) \tag{4.53a}$$

$$i_{4b} = I_4 \times sin(2\omega t) \tag{4.53b}$$

Where I_4 is the amplitude of the equivalent 2-phase AC current, and its value is $I_4 = \frac{\sqrt{3}}{\sqrt{2}} I_m$. This 2-phase current is rotating with an angular electrical velocity of 2ω, and the generated magnetic field is rotating with a mechanical angular velocity of ω. As a result, all the radial force generations, both the unstable radial magnetic forces and the suspension forces, are in the rotational coordinate of an angular velocity of ω. This coordinate is often called d-q coordinate [**?**]. However, the rotor displacement measurements and radial position control signals are in the stationary x-y coordinate, thus a transformation from stationary x-y frame to the rotational d-q frame in needed to link the two coordinates.

Figure 4-11 presents the block diagram of a bearingless motor under AC excitation. By exciting the 4-pole motor windings with a symmetric rotational 3-phase current given in (4.51), a rotational magnetic field with a mechanical angular velocity of ω

can be created, which will generate an unstable radial force in the d-q coordinate to the rotor when the rotor has an eccentric displacement.

The air gap lengths in stationary x-y coordinates are measured by displacement sensors. Rotor's position error are calculated by $e_x = x_{ref} - x$, and $e_y = y_{ref} - y$. In the design of reaction sphere, we set both x_{ref} and y_{ref} to be zero.

Two controllers in x- and y-directions are designed for the sphere's lateral suspension, and the control effort signals are defined as u_x and u_y. The design details of the controller are presented in the next section. These two control effort signals are then transformed to the rotational d-q coordinate via the well-known Park transformation as

$$\begin{bmatrix} u_d \\ \\ u_q \end{bmatrix} = \begin{bmatrix} cos(2\omega t) & sin(2\omega t) \\ \\ sin(2\omega t) & -cos(2\omega t) \end{bmatrix} \begin{bmatrix} u_x \\ \\ u_y \end{bmatrix}. \tag{4.54}$$

More details about the Park transformation are presented in [25]. The rotational control effort signals u_d and u_q are then transformed into 3-phase via the two-phase to three-phase transformation by

$$\begin{bmatrix} i^*_{2u} \\ \\ i^*_{2v} \\ \\ i^*_{2w} \end{bmatrix} = [C_{32}]^T \begin{bmatrix} u_d \\ \\ u_q \end{bmatrix}. \tag{4.55}$$

The control signals in rotational three-phase coordinate i^*_{2u}, i^*_{2v} and i^*_{2w} are then fed into the current control power amplifiers and energizes the radial position control windings (here the 2 pole windings). The combination effect of the two sets of windings will work in the same way as under DC excitation, except that when the system under DC excitation the force generations are in stationary x-y coordinate, while under AC excitation it is in the rotational d-q coordinate.

4.4.2 Lateral suspension control design

This section discuss the controller design for the lateral suspension of the bearingless motor system. Since the Park transformation can transform an AC excited system to a DC excited system, and the three-phase to two-phase transformation can effectively decouple the x- and y-direction levitation, the control for the bearingless motor is essentially the same as the control for single degree-of-freedom magnetic levitation. Based on the plant transfer function that we have derived and the measured plant dynamics, two PID controllers are designed to stabilize the lateral magnetic levitation system in x- and y-directions. The control loop is similar to the vertical suspension we discussed in Chapter 3. However, different from the control loop for a single degree-of-freedom magnetic levitation, the change of negative stiffness with the motor current amplitude requires a controller that can stabilize the system with all excitation amplitudes.

We modify the controller for lateral levitation according to both the model derived in the above sections and the measured frequency response data. From the transfer function given in (4.42), it can be observed that the break frequency of the plant transfer function is the square root of the ratio between negative stiffness and the rotor mass, or $\sqrt{K_s/m}$, and (4.48) shows that the negative stiffness K_s is proportional to the square of the peak amplitude of the 4-pole current I_m. Based on these facts, we can predict that the break frequency of the plant Bode plot should have a linear relationship with I_m. Plotting the break frequencies of the measured plant Bode plots under different driving current amplitudes I_m, we get the data shown in Figure 4-12. Fitting the data with a linear function we can get the relation as

$$f_{break}[\text{Hz}] = 3.14 \times I_m[\text{Amp}] + 3.19. \tag{4.56}$$

This change of the break frequency of the lateral levitation plant shows that as the amplitude of the excitation strength decreases, the unstable radial force is getting smaller, thus the negative stiffness in this radial suspension system decreases. This implies that a bearingless motor system requires a minimum driving current amplitude

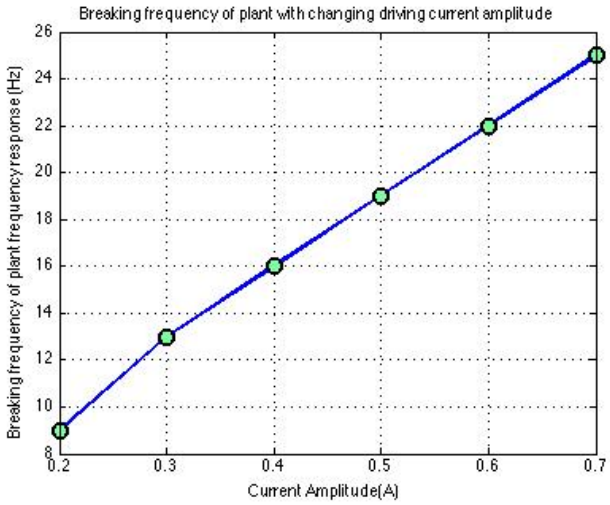

Figure 4-12: Break frequency of plant with changing driving current amplitude.

in the motor windings, even when no driving torque is needed, in order to maintain radial suspension.

This change in the plant frequency response also requires adjustments in the controller to keep the system stable under all driving conditions. To address this, the PID controllers are designed to adaptively adjust their parameters according to (4.56). The transfer function of the lead-lag form PID controller for lateral suspension control of the reaction sphere can be written as

$$C(s) = K_p \left(1 + \frac{1}{T_i s}\right) \cdot \frac{\alpha\tau s + 1}{\tau s + 1}. \tag{4.57}$$

Here K_p is the proportional gain. T_i is the integral time, which determines the zero position of the lag compensator. α is the separation ratio of the lead compensator, and τ is the time constant that determines the pole and zero locations in the lead compensator. In the design of the controller, we decide to crossover at 5 times of the break frequency. Hence under certain excitation amplitude I_m the desired crossover frequency is $\omega_c = 5 \times 2\pi \times f_{break}(I_m)$.

In the controller design we want to put the phase peak of the lead compensator at the desired crossover frequency. Let us set the α fixed at 10, thus the τ need to adjust by

$$\tau = \frac{1}{\omega_c \sqrt{(\alpha)}}. \tag{4.58}$$

To achieve a fixed phase margin, we also set the zero position of the lag compensator $\frac{1}{T_i}$ at one decade before the desired crossover frequency. A fixed proportional gain $K_p = 6$ is used. As a result, two parameters in the controller, τ and T_i, are adjusting in real time with the excitation amplitude I_m.

Figure 4-13 shows the measured loop return ratio of the reaction sphere's lateral suspension control of the system. From the measured Bode plots we can see that the proposed controller design can stabilize the lateral suspension control under different motor current amplitude. With this controller design, the loop reached a bandwidth varying with the excitation current amplitude and a fixed phase margin of 45^o. Under 0.2 A excitation current, the loop has a crossover frequency of 95 rad/s. With 0.7 A excitation the crossover frequency is is 380 rad/s. In this way the radial position of the sphere is successfully regulated at the center of the stator under different excitation amplitudes.

4.5 Summary

This chapter studies the lateral suspension of the reaction sphere, which is achieved by means of a bearingless motor. By arranging two sets of three-phase windings on a single stator and control the currents that energize the windings, the sphere can be successfully driven by a revolving magnetic field while levitated at the center of the stator bore.

In this chapter, we first introduced the principle of suspension force generation in a bearingless motor. Then a complete model for a bearingless motor is developed, and a plant transfer function of the sphere's lateral suspension is derived. Later on this model is being verified by experimental data measured from the 1D-MSRS hardware. Finally the AC excitation of a bearingless motor and the controller design of the reaction sphere's lateral suspension are introduced.

This chapter mainly talks about the bearing function of the bearingless motor in

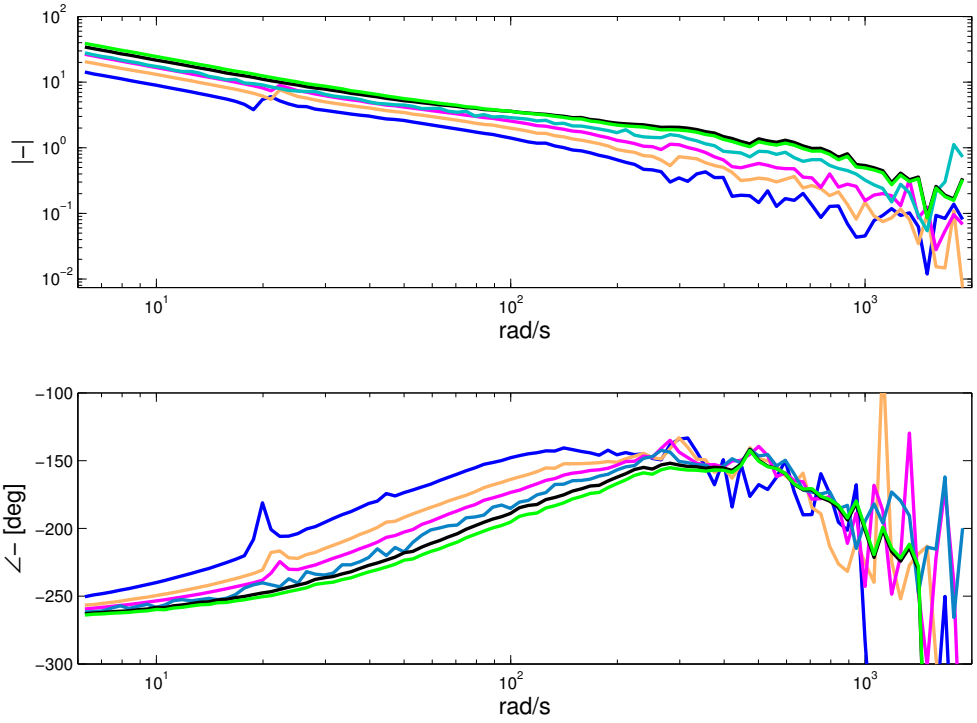

Figure 4-13: Measured Bode plots of loop-return-ratio of the lateral suspension control loop under different 3-phase-4-pole peak current amplitudes.

the reaction sphere designs. The motor operation of the reaction sphere is introduced in the next chapter.

Chapter 5

Hysteresis Motor

This chapter presents the motor operation of the 1D-MSRS. The reaction sphere in the 1D-MSRS is driven by a hysteresis motor. In this chapter, we first briefly introduce the torque production mechanism of the hysteresis motor. Then an equivalent circuit model for hysteresis motor is introduced and being modified to analyze the reaction sphere. After that, the test results of the motor operation of the 1D-MSRS are presented, and the simulation results using the equivalent circuit model are compared with experimental data from the 1D-MSRS hardware. This comparison verifies the simulation, which produces a testbed for the speed control design for the 1D-MSRS system.

5.1 Introduction to hysteresis motor

Among many different kinds of electrical motors, the hysteresis motor is well-known for its simple structure, constant torque during the starting period, and its quiet operation. Another distinct feature of this motor is that its rotor can be made out of a single piece of hard and strong steel, which allows the rotor to stand large stresses and makes this motor concept attractive for high-speed applications. In this section we introduce the basic principle of the hysteresis motor.

The hysteresis motor has a very simple motor construction. It consists of a regular poly-phase stator to produce revolving magnetic fields and a rotor of solid magnetic

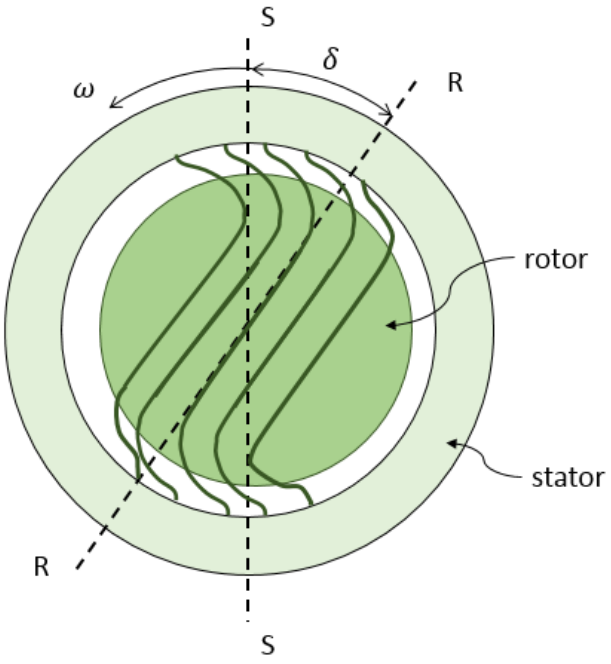

Figure 5-1: Hysteresis motor operation principle: rotor field lags behind stator excitation due to magnetic hysteresis in rotor material.

hard material. Figure 5-1 shows a diagram of an operating hysteresis motor. The rotating magneto-motive force (MMF) produced by the stator is in the direction of axis S-S, and this MMF wave is rotating with a mechanical angular velocity ω. The hysteresis of rotor material causes a lag angle δ between the direction of the rotor magnetic fields and the stator fields. This lag in spatial angle generates an tangential component of magnetic field in the air gap, and thus produce a torque to the rotor. The strength of the hysteresis torque is correlated to both the strength of the magnetic field and the lag angle.

Aside from the hysteresis torque production during the steady state operation, eddy current also works for the torque production when the motor is starting up. Before the rotor reaches the synchronous speed, each region inside the rotor experiences hysteresis cycle at the slip frequency. At the same time, due to the slip between stator and rotor field, eddy currents are generated in the rotor. The axial component of the eddy currents can produce an accelerating torque by interacting with the mag-

netic field. As the motor speed slip becomes smaller, the eddy currents in the rotor decays, until the speed of the rotor reaches the synchronous speed. When the motor is operating in steady state, the eddy currents vanish, and only the hysteresis effect is producing torque.

To sum up, hysteresis motors use the combination of eddy currents and the hysteresis of rotor material for torque production. In this sense, hysteresis motor is a combination of a weak permanent magnet motor and an induction motor. Being a synchronous motor, during the start-up, the accelerating torque is due to both eddy current and reluctance force by hysteresis. Once the rotor becomes synchronous with stator field, the eddy current vanishes and it resembles a permanent magnet machine.

In the next section, an equivalent circuit model of the hysteresis motor is presented, and is being modified to analyze the motor operation of the reaction sphere.

5.2 Equivalent circuit model of hysteresis motor

In order to study the dynamic behavior of 1D-MSRS, a model of the hysteresis motor is necessary. Modeling of the hysteresis motor is difficult due to the nonlinearity of hysteresis material properties. Researchers have developed several different models for hysteresis motor. Copeland [26] presented an analytical study of hysteresis motors and introduced the idea of using the fundamental harmonic response to the magnetizing field by simplifying the hysteresis loop into a parallelogram shape. Miyairi and Kataoka [15] introduced an elliptical hysteresis loop model and derived an equivalent circuit model for the hysteresis motor under this assumption. Several other papers [27] and [28] presented different set of hysteresis motor models using the analogies to other types of motors.

In our work, the elliptical hysteresis model based equivalent circuit of hysteresis motor developed by Miyairi and T. Kataoka [15] and further presented in [29] and [6] is used to analyze the dynamic behavior of the 1D-MSRS. This model is used to analyze both the steady state running and starting up of the reaction sphere, although the model is built based on sinusoidal steady state assumptions. The reasons that we

extended this model for hysteresis motor transient analysis are listed below.

1. We are using the self-bearing motor for the lateral suspension of the 1D-MSRS, thus the sphere is always first levitated in radial directions and then being driven by rotating magnetic field. In this way, under DC excitation conditions or rotating under the excitation of rotating magnetic field, the magnetization pattern and pole distribution of the sphere surface is the same. Therefore we do not need to model the virgin magnetization curve (B-H curve starting from zero magnetization) as most hysteresis motor transient simulation does.

2. The reaction sphere is excited below saturation. In this circumstance the real hysteresis loop has less higher order harmonics, which makes it more similar to a phase lag between B field and H field.

3. Due to the effect of eddy currents, the hysteresis property is showing dependency to excitation frequency. The loop widening effect makes the hysteresis loop get more close to an elliptical model.

4. This model has an assumption that the hysteresis lag angle is held constant and is equal to it's maximum when slip is large, which makes the motor hysteresis starting torque maximum and does not depend on slip during starting up. This assumption is close to what is really happening when a hysteresis motor is starting spinning, and makes this equivalent circuit model valid for motor transient behavior simulation, although usually they are not accurate when slip is large.

In the following of this section, the equivalent circuit of hysteresis motor is presented in detail. The derivation in this thesis follows the paper by Miyairi and Kataoka [15].

In the hysteresis motor's equivalent circuit model, a balanced single-frequency, three-phase source is assumed. The B-H curve of the rotor material is approximated by a ellipse, with B and H are give by:

$$B = B_m cos(\theta) \tag{5.1a}$$

$$H = \frac{B_m}{\mu} cos(\theta + \delta). \tag{5.1b}$$

Here δ is the lag angle between H and B. In this equation the permeability of the hysteresis material μ is defined as the ratio of the maximum value of B and H is $\mu = \frac{B_m}{H_m}$.

Another assumption in this analysis is that the distribution of the rotating MMF is pure sinusoid. Higher order harmonics of the MMF and flux distributions are neglected.

Then we start calculate the value of components in the equivalent circuit from electromagnetic modeling. In this derivation, let us assume a general hysteresis motor is being considered. The stator has m-phase, $2p$-pole motor winding, and the conductor distribution of every phase is sinusoid around the rotor. Then the k-th winding has a distribution of

$$Z_k = Zcos(\phi - (k-1)\frac{2\pi}{m})[conductors/electricradian]. \tag{5.2}$$

Here $k = 1, 2, ..., m$. ϕ is the angle in the coordinate that fixed to the stator. Z is the maximum of the conductor density, and its expression is

$$Z = \frac{2K_w N}{p\pi}. \tag{5.3}$$

Here K_w is the winding factor, N is the number of turns per phase per pole of the motor winding, and p is the number of pole pairs. Then the currents that flow through m-phase stator winding is:

$$i_k = I \cdot cos\left(\omega t - (k-1)\frac{2\pi}{m} + \phi_1\right). \tag{5.4}$$

In this equation, I is the peak current amplitude of the m-phase current, ω is the electrical angular velocity, and ϕ_1 is the initial phase of the current. From the

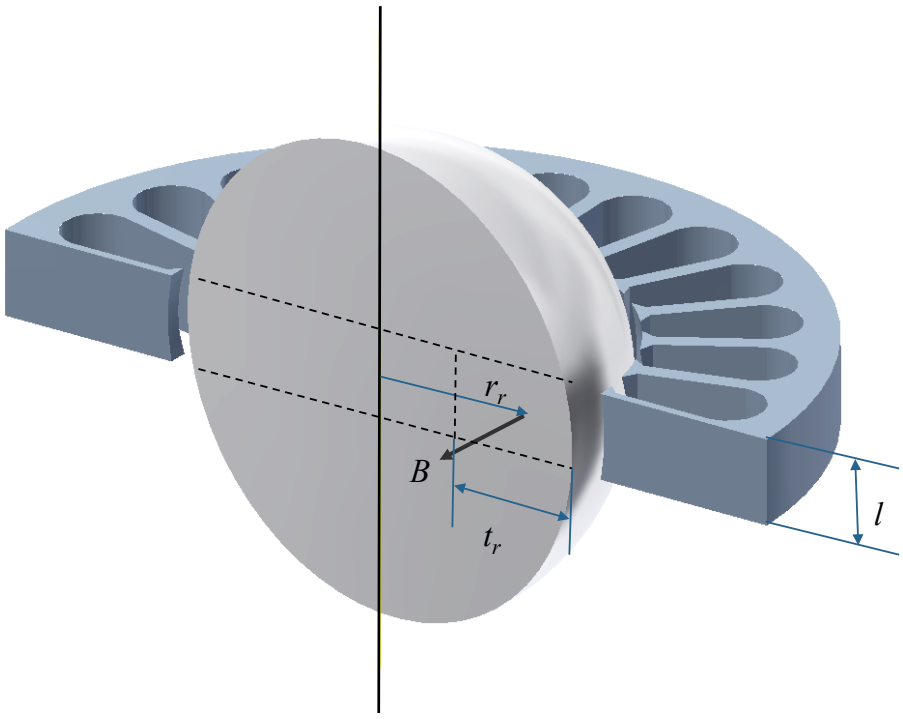

Figure 5-2: Cross section of the reaction sphere and stator structure. In this diagram, l is the height of the stator. The region in the dash line shows the equivalent cross-section area that the magnetic fluxes flow through. t_r is the equivalent depth of the rotor. r_r is the equivalent radius of the rotor sphere, which is the average radius in the rotor where the magnetic fluxes flows along.

winding and current distribution in (5.4) and (5.2), the magneto-motive force (MMF) distribution generated by the stator winding can be calculated as

$$\mathcal{F}_M = \sum_{k=1}^{m} Z_k i_k = \frac{m}{2} I Z cos(\omega t - \phi + \phi_1) \tag{5.5}$$

We can use the MMF distribution expression in (5.5) to study the flux distribution in the air gap and the rotor. In this analysis, the permeability of the stator iron material is assumed to be infinite, thus the magnetic field intensity in the stator back iron is zero.

Figure 5-2 shows a cross section diagram of the reaction sphere. As shown in the figure, the motor length is defined to be the length of the stator since the rotor sphere is much longer than the stator in the z-axis direction. In the cross-section of the sphere rotor, the region in the dash line shows an equivalent cross-section area

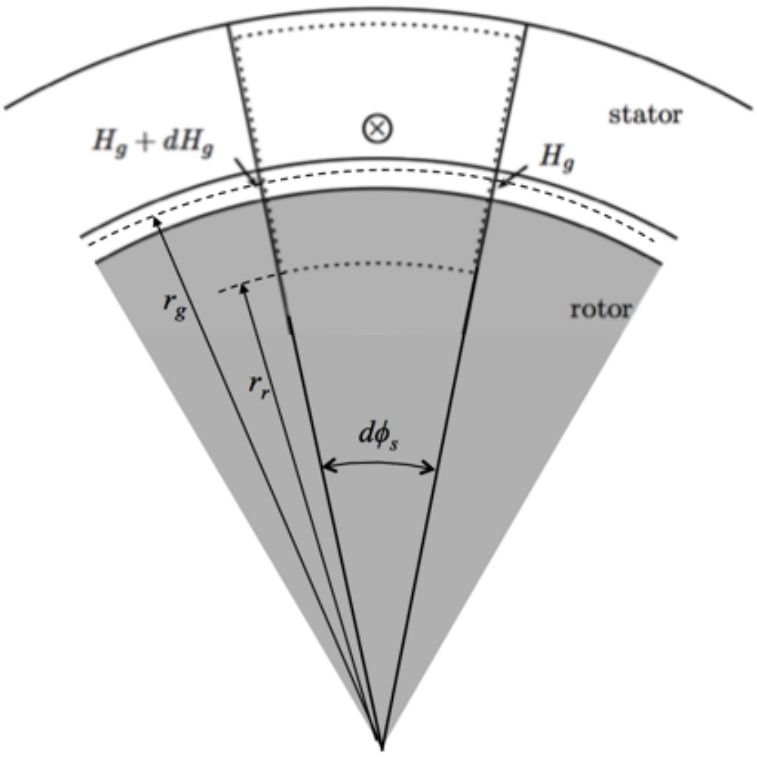

Figure 5-3: Motor geometry and magnetic path at equator of sphere. $\mathrm{d}\phi_s$ is an incremental angle in the angular coordinate. r_r is the equivalent radius of the rotor. r_g is the average radius of the air gap.

that the magnetic flux in the rotor will flows through. The length t_r shows the depth of this area, and r_r shows the average radius of this cross section. In the following derivation, we assume that all the magnetic fluxes in the rotor are flowing along the radius r_r, so the radius r_r is also called equivalent radius of the rotor sphere.

Figure 5-3 shows a top-view cross section of stator-gap-rotor of hysteresis motor with a small angle $\mathrm{d}\phi_s$. The average radius of the air gap is defined to be r_g, and the air gap length is denoted by g. A closed magnetic path that goes through the equivalent radius in the rotor r_r is shown with dotted line in Figure 5-3. By applying Ampere's law to the defined closed magnetic path, we can have

$$\mathcal{F}_M \mathrm{d}\phi_s = -(H_g + \mathrm{d}H_g)g + H_g g + H_r r_r \frac{\mathrm{d}\phi_s}{p}. \tag{5.6}$$

In this equation, $\mathcal{F}_M \mathrm{d}\phi_s$ denotes the magneto-motive force provided by the section

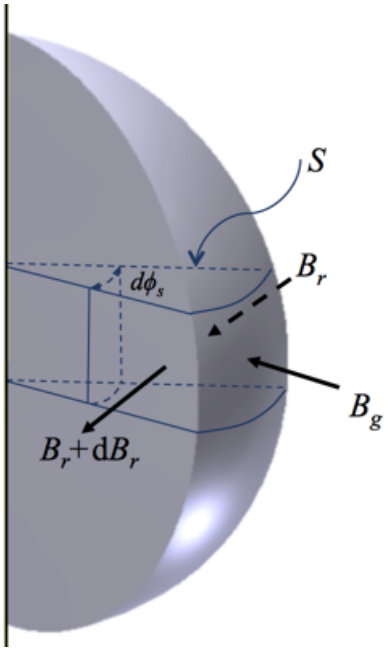

Figure 5-4: A section of rotor with an incremental angle of dϕ_s in the angular coordinate around the vertical axis. B_g is the flux in the air gap. B_r is the magnetic flux in the rotor.

of stator winding inside the magnetic path. dϕ_s is the incremental angle in the angular coordinate around the motor. p is the number of pole pairs. g is the length of the air gap. r_r is the radius that the magnetic field that passes through in the rotor. H_g is the magnetic field strength in the air gap, and dH_g is the incremental air gap field strength. H_r is the field strength in the rotor align to the selected magnetic path.

By dividing (5.6) by dϕ_s, and let d$\phi_s \to 0$, we can have

$$\mathcal{F}_M = g\frac{\partial H_g}{\partial \phi_s} + \frac{r_r}{p}H_r. \tag{5.7}$$

Figure 5-4 shows a section of the rotor of angle dϕ_s. We can see that the magnetic fluxes that flow into this section of rotor include the flux in the rotor B_r and B_r + d$B_r$and the flux in the air gap B_g. S is a closed surface denoted in the figure by the dark blue lines. By applying Gauss's law to the closed surface S, we can have

$$\iint_S BdS = (B_r + \mathrm{d}B_r)t_r l - B_r t_r l + \mu_0 H_g l r_g \frac{d\phi_s}{p} = 0. \tag{5.8}$$

Here t_r is the equivalent thickness of the rotor defined in Figure 5-2. l is the motor length. r_g is the mean radius in the air gap. B_r is the magnetic flux that flows in the cross-section of the rotor. H_g is the magnetic field strength in the air gap. With $\mathrm{d}\phi_s \to 0$ we can get the expression of flux in the air gap as

$$B_g = \mu_0 H_g = -\frac{pt_r}{r_g}\frac{\partial B_r}{\partial \phi_s}. \tag{5.9}$$

Substituting the value of H_g give by (5.9) into (5.7), we can get

$$\mathcal{F}_M = -\frac{gpt_r}{\mu_0 r_g}\frac{\partial^2 B_r}{\partial \phi_s^2} + \frac{r_r}{p}H_r. \tag{5.10}$$

Let us substitute the material property given in (5.1) and the expression of the MMF distribution given in (5.5) into the above equation, and apply the sinusoidal distribution assumption to the flux distributions. Then the below equation is reached:

$$\frac{m}{2}IZcos(\omega t - \phi + \phi_1) = \frac{gpt_r}{\mu_0 r_g}B_m cos(\omega t - \phi) + \frac{r_r}{p\mu}B_m cos(\omega t - \phi + \delta). \tag{5.11}$$

The equivalent circuit model is developed based on the above equation. The left-hand side in (5.11) is the MMF generated by the stator winding. The two terms on the right-hand side can be regarded as the magnetic potential that dissipated in the air gap and inside the rotor respectively. This equation separated the magnetic potential into two parts: the air gap part and the rotor part. Based on this equation, we can separate the stator current of k-th phase as

$$i = i_g + i_r, \tag{5.12}$$

where i is the k-th phase current that flows in the stator winding, and i_g and i_r are the equivalent current for air gap and rotor respectively. We know that the k-th phase current in the stator winding is given by

$$i = Icos(\omega t - (k-1)\frac{2\pi}{m} + \phi_1). \tag{5.13}$$

Based on equation (5.11), we can calculate the values of the equivalent air gap and rotor currents as:

$$i_g = \frac{2gpt_r}{mZ\mu_0 r_g} B_m cos(\omega t - (k-1)\frac{2\pi}{m}) \tag{5.14a}$$

$$i_r = \frac{2r_r}{mZp\mu} B_m cos\omega t - (k-1)\frac{2\pi}{m} + \delta. \tag{5.14b}$$

Since the stator current and both the equivalent currents are sinusoidal in time, we can write them into phasor form, as

$$\dot{I} = \dot{I}_g + \dot{I}_r. \tag{5.15}$$

Here $\dot{I}$ is the phasor of the sinusoidal stator current value. $\dot{I}_g$ and $\dot{I}_r$ are the phasors of the equivalent air gap and rotor currents respectively. Their values are

$$\dot{I} = Ie^{j\phi_1} \tag{5.16a}$$

$$\dot{I}_g = \frac{\pi p^2 g t_r B_m}{\sqrt{2} m K_w N \mu_0 r_g} e^{j0} \tag{5.16b}$$

$$\dot{I}_r = \frac{\pi r_r B_m}{\sqrt{2} m K_w N \mu} e^{j\delta}. \tag{5.16c}$$

Figure 5-5 shows the phasor diagram of the equivalent currents with the phase of the equivalent air gap current $\dot{I}_g$ set to zero. The phasor ϵ denotes the stator voltage of k-th phase winding, which is orthogonal to the air gap current phasor. We can see from the diagram that the phasor of the stator current $\dot{I}$ is a vector sum of the equivalent currents $\dot{I}_g$ and $\dot{I}_r$. The phase difference between the two equivalent current is the lag angle δ.

Based on the current phasors that we have derived, we can calculate an equivalent circuit components of the hysteresis motor by paralleling the two current paths: equivalent rotor current and the equivalent air gap current. Note that these two currents are not real current that flows in the air gap or rotor. Instead, they are a part

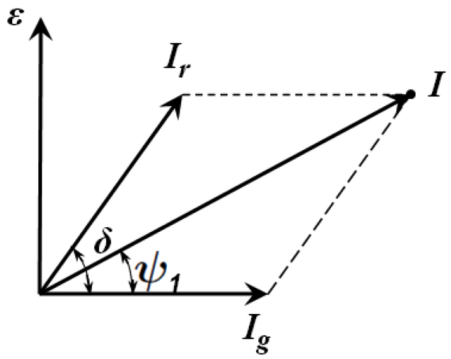

Figure 5-5: Phasor diagram of the apparent currents in the equivalent circuit. I is the current in the stator winding. I_r is the rotor equivalent current. I_g is the air gap equivalent current.

of the stator current. The equivalent circuit diagram is shown in Figure 5-6. The values of the equivalent circuit components are:

$$L_g = \frac{2mK_w{}^2N^2\mu_0 l r_g}{p^2\pi g} \tag{5.17a}$$

$$R_r = \omega_b \frac{mK_w{}^2N^2V_r\mu}{\pi^2 r_r{}^2} sin\delta \tag{5.17b}$$

$$L_r = \omega_b \frac{mK_w{}^2N^2V_r\mu}{\pi^2 r_r{}^2} cos\delta. \tag{5.17c}$$

Here V_r is the equivalent volume of the rotor, which is calculated as $V_r = 2\pi r_r t_r l$. Notice that the hysteresis part of the rotor apparent impedances are depending on the lag angle δ.

Aside from the hysteresis of rotor material, another phenomena that produces accelerating torque to the rotor is the eddy current effect. When there is slip between the stator frame and the rotor frame, eddy current will be generated in the rotor, mainly in the axial direction, and a torque will be produced to the rotor by the interaction between this current and the stator magnetic field. With the slip becomes smaller, the eddy current decays. To represent this effect, a resistance R_e/s is added to the hysteresis motor's equivalent circuit model, where s is the motor slip. Then the modified rotor current I_r is the total current that flows through the hysteresis

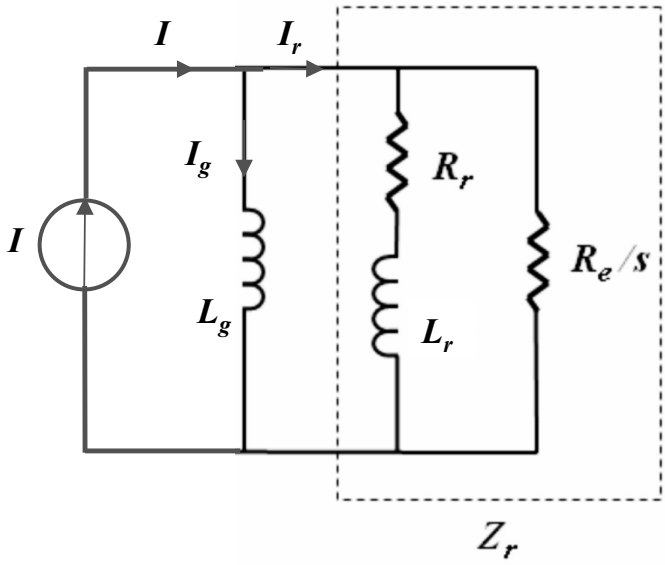

Figure 5-6: Equivalent circuit model of hysteresis motor. Here I denotes stator current. I_g and I_r are the equivalent currents for air gap and rotor respectively. L_g is the equivalent air gap impedance. Z_r is the rotor equivalent impedance, which included both rotor hysteresis impedance R_r and L_r and equivalent impedance R_e/s. Here s is the motor speed slip.

rotor impedances and the eddy current apparent resistance. According to the report by Livermore National Laboratory [29], the value of R_e can be calculated by

$$R_e = \frac{12\rho l}{10^4 A_h}. \tag{5.18}$$

where ρ is the specific resistivity of the rotor material, and A_h is the axial cross-section area of the rotor. In our analysis, the cross section area is $A_h = \pi(R^2 - (R - t_r)^2)$, with the R being the radius of the rotor sphere.

Then torque production of the hysteresis motor, including both the hysteresis torque and eddy current torque, can be calculated by:

$$T_e = \frac{m}{2}\frac{P}{2} L_g I_r I_g sin\delta. \tag{5.19}$$

Here I_r and I_g are the equivalent current values that calculated by the equivalent circuit model in Figure 5-6. Then the motor's mechanical speed can be calculated by the rotor's dynamic equation:

$$T_e - T_d = \frac{J}{p}\frac{d\omega_r}{dt} + A|\omega_r|^2. \tag{5.20}$$

Here ω_r is the mechanical angular speed of the rotor, J is the inertia of the rotor, and the air drag to the rotor is expressed as proportional to the square of the angular velocity with a coefficient of A. The lag angle between electrical angular position and mechanical angular position is given by:

$$\frac{\omega - \omega_r}{p} = \frac{\mathrm{d}\delta}{\mathrm{d}t}. \tag{5.21}$$

The above equations present a dynamic model to a hysteresis motor, with its torque production calculated by the equivalent circuit model. We will use this model to simulate the motor behavior of the 1D magnetic suspended reaction sphere.

5.3 Identification of motor equivalent circuit parameters

In order to simulate the motor dynamics of the 1D-MSRS, we need to identify the parameters of the reaction sphere that are required for the calculation. Most of the numbers are motor design parameters, which are determined by the 1D-MSRS hardware. Table 5.1 shows the design parameters for the 1D reaction sphere.

Table 5.1: Parameters for equivalent circuit model simulation

parameter	value
Sphere radius	27 mm
Stator height	9.5 mm
Stator back iron length	12mm
Stator pole width	3 mm
Air gap length between stator and sphere (each side)	0.4 mm
Stator number of slots	24
Number of poles for motor winding	4
Number of wires per slot for motor winding	80
Number of poles for suspension winding	2
Number of wires per slot for suspension winding	40

Aside from the above listed design parameters, there are still several system parameters of the reaction sphere that will be used in the modeling. These parameters will need to be identified by either calculation or measurement. These parameters are: permeability μ and lag angle of hysteresis loop δ of the rotor material, average radius of magnetic path in rotor r_r and the rotor's equivalent thickness t_r. In the following text in this section, the identification of these parameters are introduced.

Hysteresis material approximation

In the derivation of the equivalent circuit model of the hysteresis motor, an elliptical assumption of hysteresis loop is adopted. The flux density and field under this assumption can be written as

$$B = B_m cos(\theta) \tag{5.22a}$$

$$H = \frac{B_m}{\mu} cos(\theta + \delta). \tag{5.22b}$$

Here δ is defined as the lag angle between H and B, and the permeability μ is defined as the ratio of the maximum value of B and H, and can be written as

$$\mu = \frac{B_m}{H_m}. \tag{5.23}$$

Figure 5-7 presents the hysteresis loops of D2 steel measured from a ring of D2 steel. The original data and the measurement process are given in the doctoral thesis of Dr. Mohammad Imani Nejad [6]. In the figure, the red and blue lines are the data measured under 3 Hz and 50 Hz excitations and their elliptical approximations respectively. We can clearly see that the loop shapes that measured under different excitation frequencies are different. This effect is called loop widening effect, which means that the magnetic hysteresis loop gets widen as the excitation frequency goes up. Reference [30] gives a general introduction about the physics of the loop widening effect.

Figure 5-8 shows the measured D2 steel magnetic properties as a function of excitation frequency. In this figure, the blue line shows the relative permeability μ, and the green line shows the lag angle δ. The data is taken from the doctoral thesis of Dr. Mohammad Imani Nejad [6].

The measured data in Figure 5-7 and 5-8 allow us to choose the rotor material property parameters in the simulation according to the excitation frequency. In the simulation shown in this thesis, the reaction sphere is running at an electrical frequency of 60 Hz. As a result, the material property parameters used in the simulation are $\mu = 150$ and $\delta_{max} = 42°$.

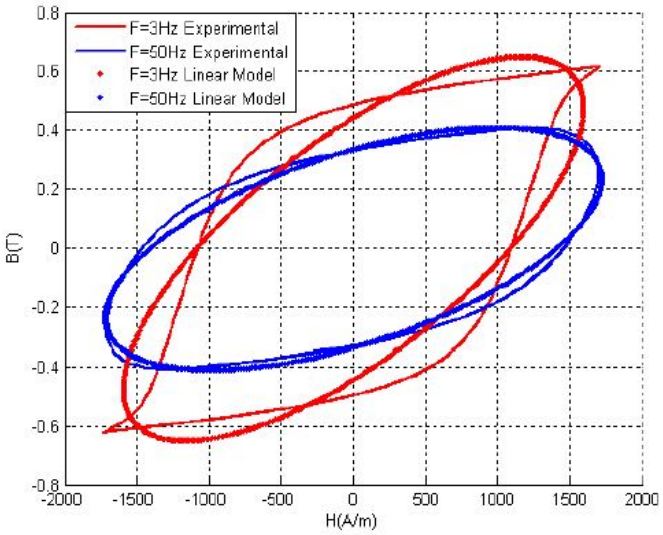

Figure 5-7: D2 steel linear model approximation.

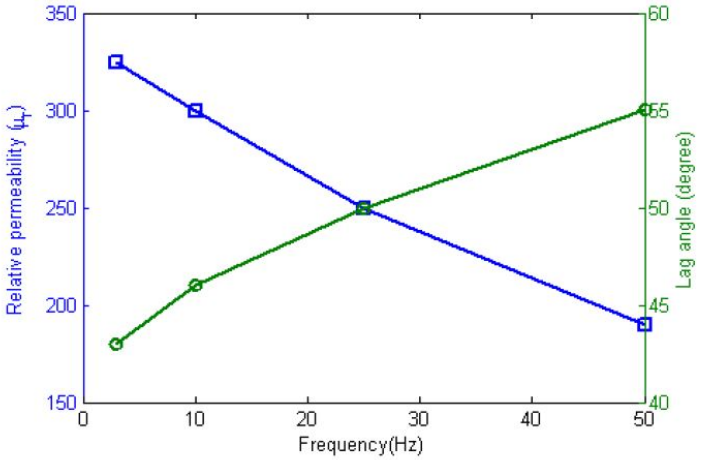

Figure 5-8: D2 steel magnetic properties as a function of frequency.

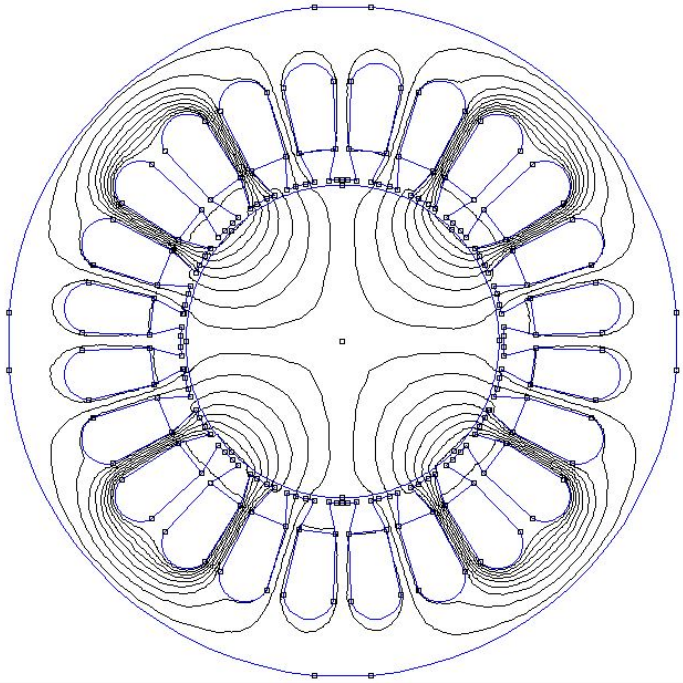

Figure 5-9: Magnetic field of the motor calculated by the 2D finite element method. Figure shows the motor geometry of the cross-section along the equator of the sphere.

Equivalent magnetic path in rotor

In the derivation of the equivalent circuit model of hysteresis motor, there are two parameters about the geometry of the magnetic path in rotor: (a) the equivalent rotor thickness t_r, and (b) the mean radius r_r. In Miyari's paper [15], the hysteresis motor being considered has a ring type rotor, thus radius is defined as the radius of the mid-line in the rotor ring, and the thickness is also determined by the rotor's geometry. However, when the rotor becomes a solid sphere, these definitions are no longer suitable. In order to make the simulations more accurate, finite element method is used to identify the equivalent thickness and the average radius of the magnetic path in the rotor sphere. Figure 5-9 presents the calculation result of the finite element analysis of the motor magnetic field using FEMM [21]. From the magnetic field shown in the figure, we can determine the average thickness of the rotor is t_r and the mean radius of the magnetic path in rotor r_r. In the simulation, the parameters being chosen are $t_r = 10$ mm and $r_r = 21.5$ mm.

5.4 Simulation

In this section the simulation of the hysteresis motor of the reaction sphere is described. Matlab/Simulink is used for the simulation of the motor system. This model is originally created by Dr. Mohammad Imani Nejad following the simulation procedure described in a technical report from Livermore National Laboratory [29], and is modified for the reaction sphere's simulation. The steps of this simulation can be summarized as:

1. Assign appropriate initial conditions: in this simulation we define the proper initial condition for angular velocity and lag angle in order to solve the governing differential equations of the motor dynamics.

2. Solve equivalent circuits for apparent currents: once we have the equivalent impedances, we can use Kirchhoff's circuit laws to find the rotor and gap apparent currents for given excitation current amplitude and electrical frequency.

3. Calculate motor torque: the torque that produced by the motor can be computed as

$$T_e = \frac{m}{2}\frac{P}{2} L_g I_r I_g sin\delta \tag{5.24}$$

4. Calculate motor speed: the motor's mechanical speed can be calculated by the rotor's dynamic equation

$$T_e - T_d = \frac{J}{p}\frac{\mathrm{d}\omega_r}{\mathrm{d}t} + A|\omega_r|^2 \tag{5.25}$$

5. Calculate lag angle: The lag angle is given by

$$\frac{\omega_b - \omega_r}{p} = \frac{d\delta}{dt} \tag{5.26}$$

Figure 5-10 and 5-11 shows the Simulink model for the 1D-MSRS simulation. The simulation results are compared with the experimental measured motor operation data of the reaction sphere in the next section.

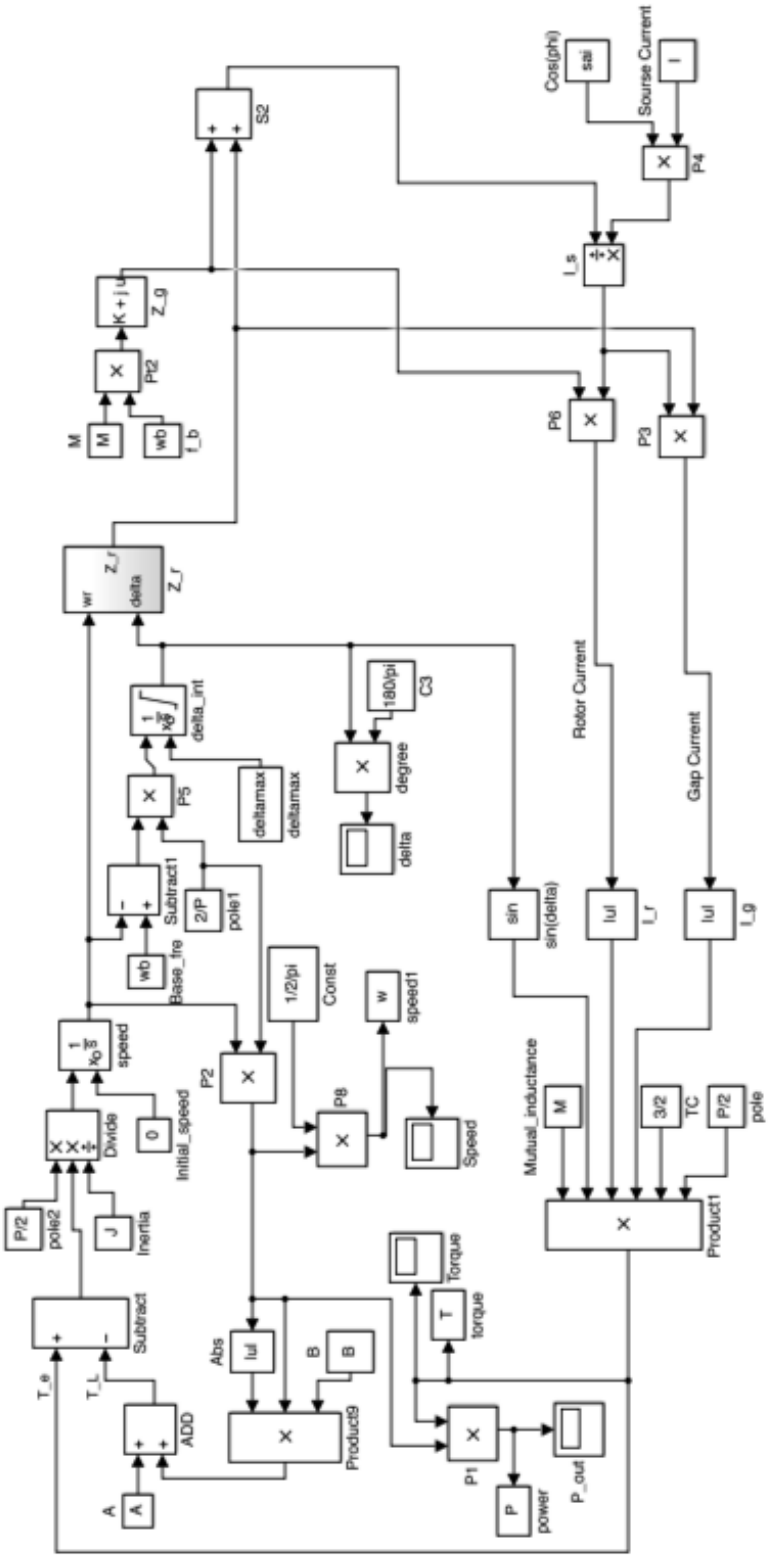

Figure 5-10: Simulink model for the hysteresis motor simulation.

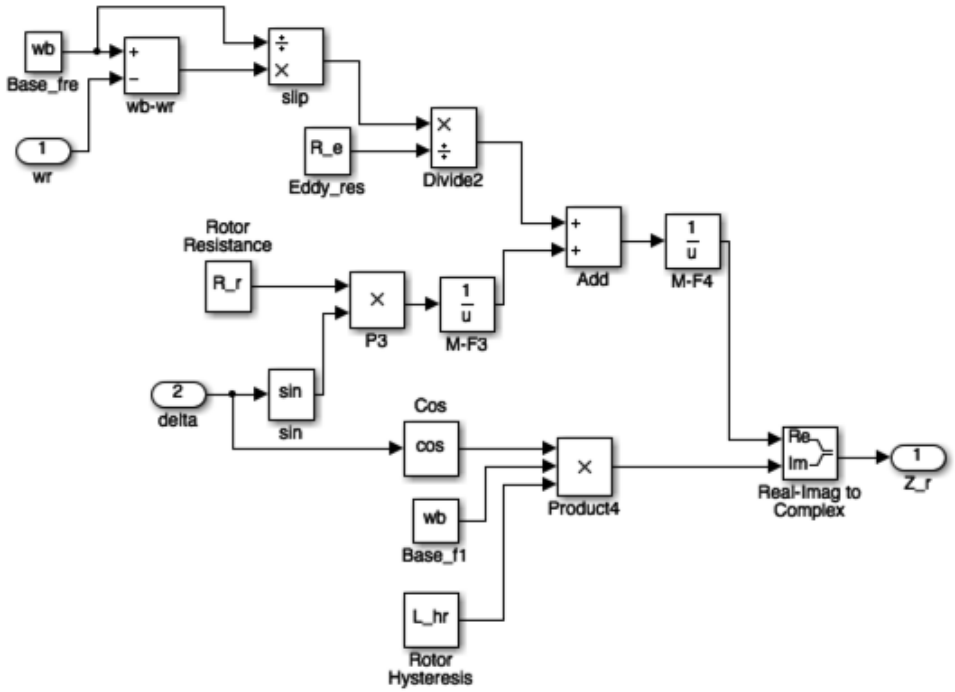

Figure 5-11: Simulink model for the rotor equivalent impedance Z_r.

5.5 Experimental and simulated motor operation

In this section, the measured starting transient speed data of the magnetic suspended reaction sphere is presented. The measurement of input power of the1D-MSRS when running in open-loop is also demonstrated. After that, the simulation results from the above described model are presented and are compared with the experimental data. Good agreement between the experimental data and the simulation results verified the effectiveness of the simulation, and this model will provide a reliable platform to study the speed control scheme for the reaction sphere.

The magnetic suspended reaction sphere is running by exciting the 4-pole motor windings with a symmetrical 3-phase current, and is magnetically suspended in all translational directions. Figure 5-12 presents the acceleration curves of the 1D-MSRS under different amplitudes of excitation current. We can see that all curves locks into the reference speed after acceleration, and a 3-5 Hz oscillation occurs when the speed reaches synchronous due to the hunting nature of hysteresis motor. The data also shows that with an excitation current of 0.7 A zero-to-peak value, the sphere can reach the synchronous speed of 30 Hz (1800 rpm) within 6 seconds. The starting torque under this excitation is 8.15×10^{-3} N.m.

The power specifications of 1D-MSRS is also tested. The currents in the motor and suspension windings are controlled through current control amplifiers following the current command that we assigned, therefore the measurement of power can be achieved by measuring the rms voltage value of the windings. In this measurement, we kept the motor winding currents to be a sinusoidal signal with a zero-to-peak value of 0.6 A (thus rms current value 0.42 A). The measurement is taking when the reaction sphere is spinning synchronously. The measured data are listed in Table 5.2. Note that these values are tested under constant motor current amplitudes. When the speed control is added to the 1D-MSRS system that enables the current amplitude changes with speed error or torque requirements, the power consumption of the sphere running in steady state can be greatly reduced.

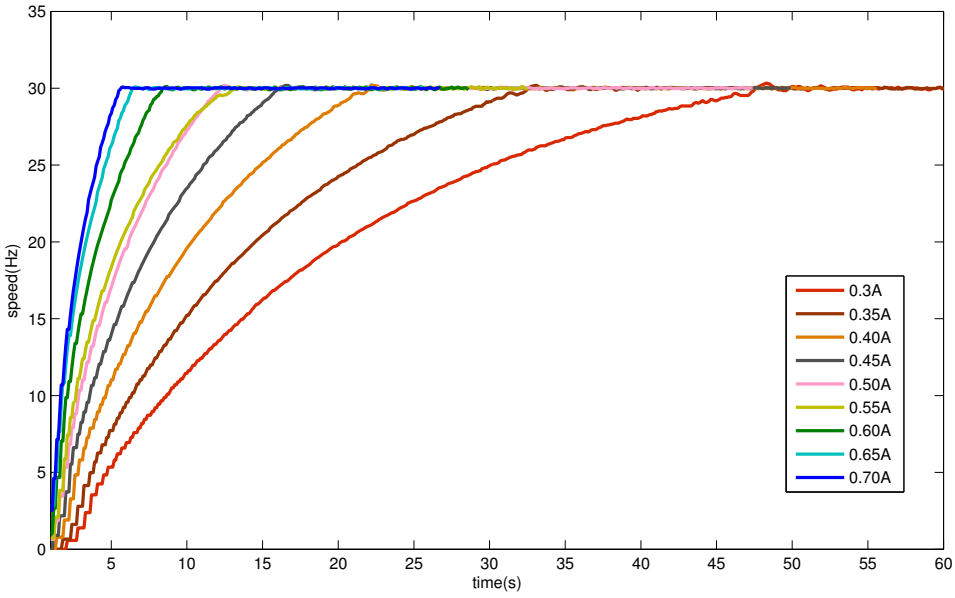

Figure 5-12: Acceleration curves of 1D-MSRS under different excitation current amplitudes. Synchronous speed is 30 Hz.

Table 5.2: Motor power consumption measurement of 1D-MSRS.

Excitation (electrical) frequency	Motor winding current (rms)	Motor winding voltage (rms)	Suspension winding current (rms)	suspension winding voltage (rms)	Total motor power consumption
60 Hz	0.42 A	10.41 V	0.052 A	6.32 V	14.63 W
120 Hz	0.42 A	16. 85 V	0.082 A	7.12 V	21.55 W

Then let us compare the simulated speed data with the experimental measured speed data under different excitation conditions. Figure 5-13, 5-14, 5-15, 5-16, 5-17 and 5-18 present the simulated and experimentally measured speed during the starting transient of the hysteresis motor of the reaction sphere plotting together under different driving current amplitude. In the figure (a) of these figures, the blue line is the simulated data of the hysteresis motor with the Matlab/Simulink model

that presented before, and the red line is showing the the speed of the reaction sphere measured by the optical tachometer during the sphere is stating up. Good agreement between simulation and experimental speed data confirms the validity of the equivalent circuit model for analysis of the 1D-MSRS. The figure (b) in these figures, the simulated results of the electrical torque production of the hysteresis motor under the given conditions are plotted. Note that although the plots are having similar shapes, the time scale shows that the rise time of the sphere's speed and the torque production ability is very sensitive to excitation current amplitude.

5.6 Summary

In this chapter the motor operation of the reaction sphere is being studied. The 1D-MSRS is driven by a hysteresis motor , which uses a combination of magnetic hysteresis and eddy current effect for torque generation. In this chapter, the principle of hysteresis operation is introduced. Then an equivalent circuit model for hysteresis motor based on the model proposed by Miyairi and Kataoka [15] is presented. A simulation of motor dynamics based on the equivalent circuit model of hysteresis motor is carried out, and a comparison between the experimental measured sphere acceleration curves and the simulated result validates the effectiveness of the model.

The experimental measured acceleration curves of the reaction sphere tells us that with 0.7 A excitation current, the sphere can reach the synchronous speed of 30 Hz (1800 rpm) within 6 seconds. The starting torque under this excitation condition can reach 8.15×10^{-3} N.m.

In the next chapter, feedback control for the hunting suppression is discussed.

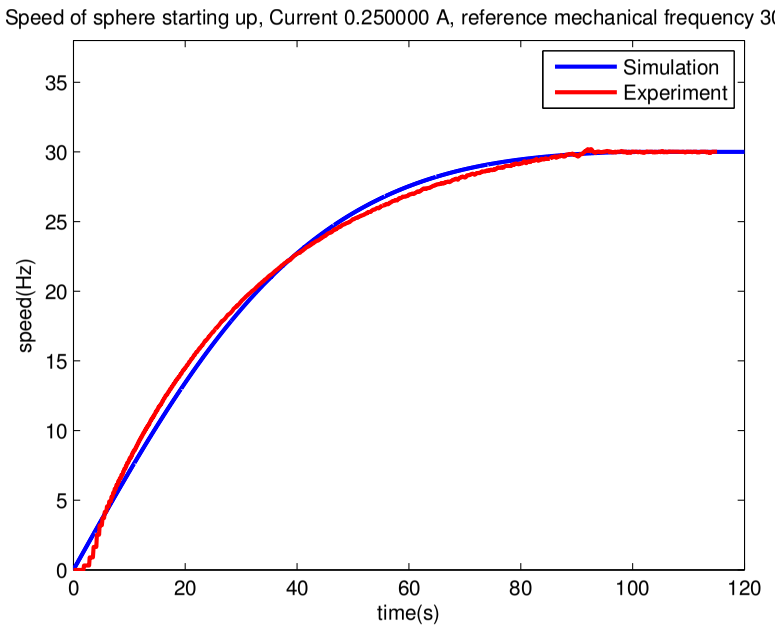

(a)

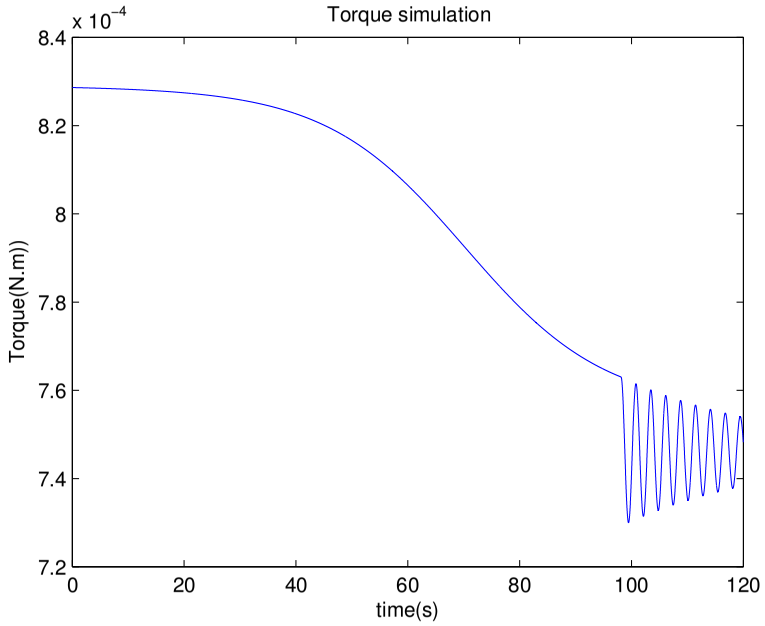

(b)

Figure 5-13: Starting transient speed data under excitation current of 0.25A.
(a) Angular Speed of Experiment and Simulation Data; (b)Torque curve.

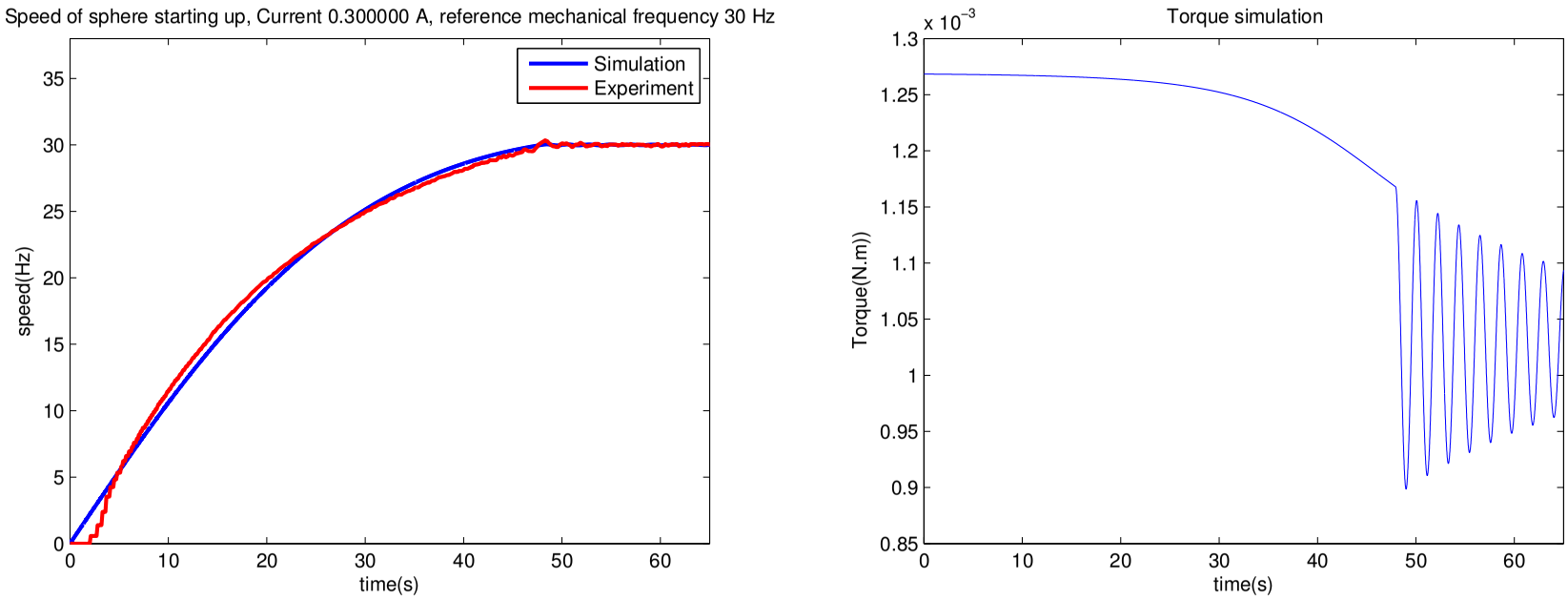

(a) (b)

Figure 5-14: Starting transient speed data under excitation current of 0.3A.
(a)Angular Speed of Experiment and Simulation Data; (b)Torque curve.

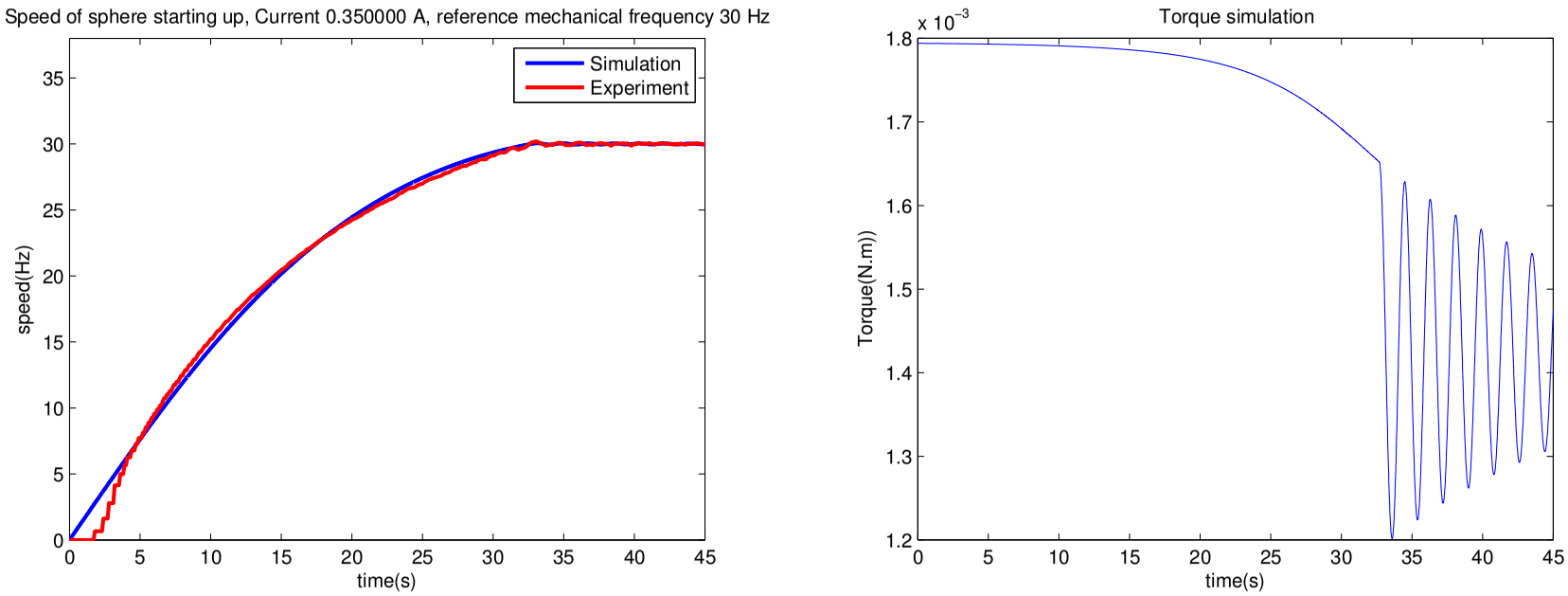

(a) (b)

Figure 5-15: Starting transient speed data under excitation current of 0.35A.
(a)Angular Speed of Experiment and Simulation Data; (b)Torque curve.

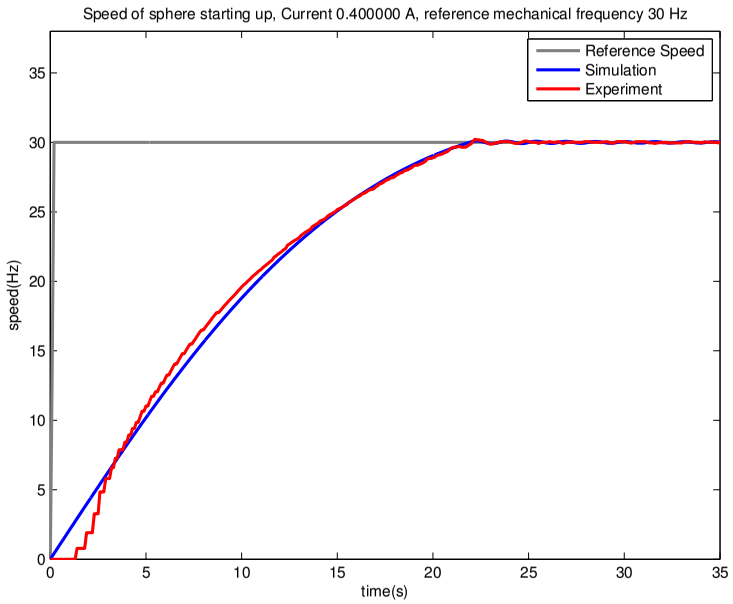

(a)

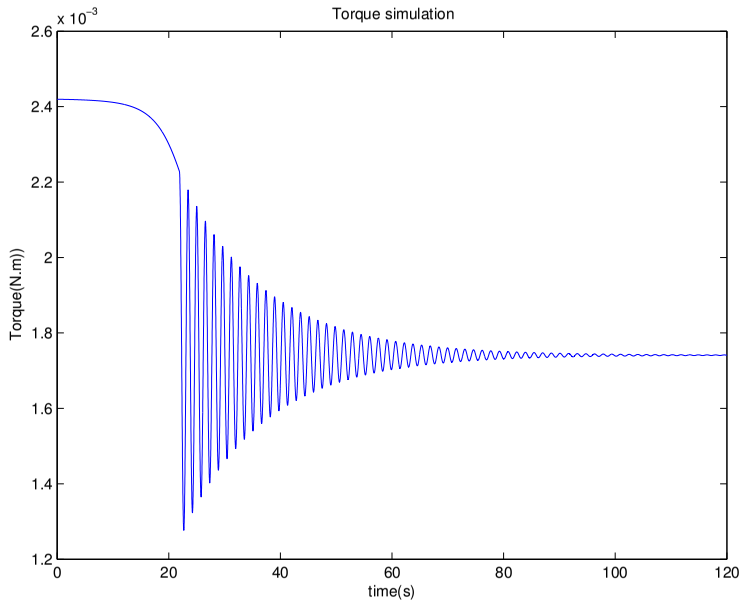

(b)

Figure 5-16: Starting transient speed data under excitation current of 0.4A.
(a)Angular Speed of Experiment and Simulation Data; (b)Torque curve.

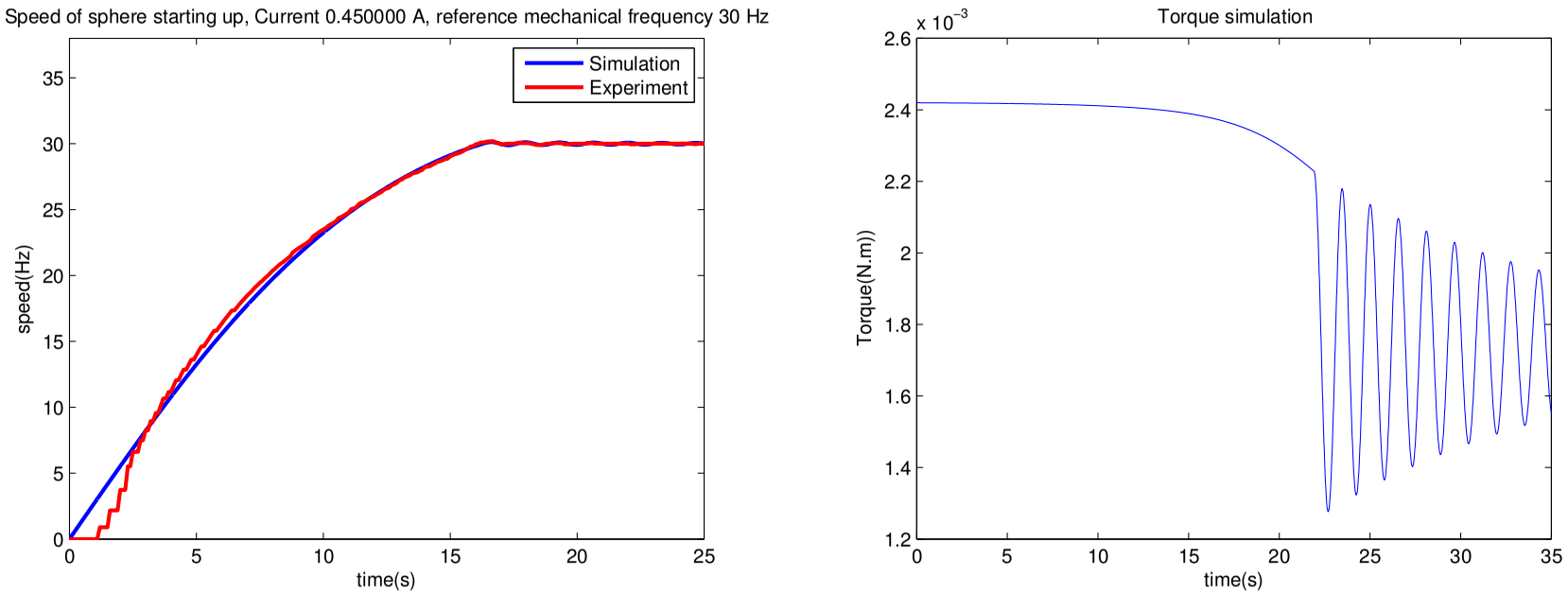

(a) (b)

Figure 5-17: Starting transient speed data under excitation current of 0.45A.
(a)Angular Speed of Experiment and Simulation Data; (b)Torque curve.

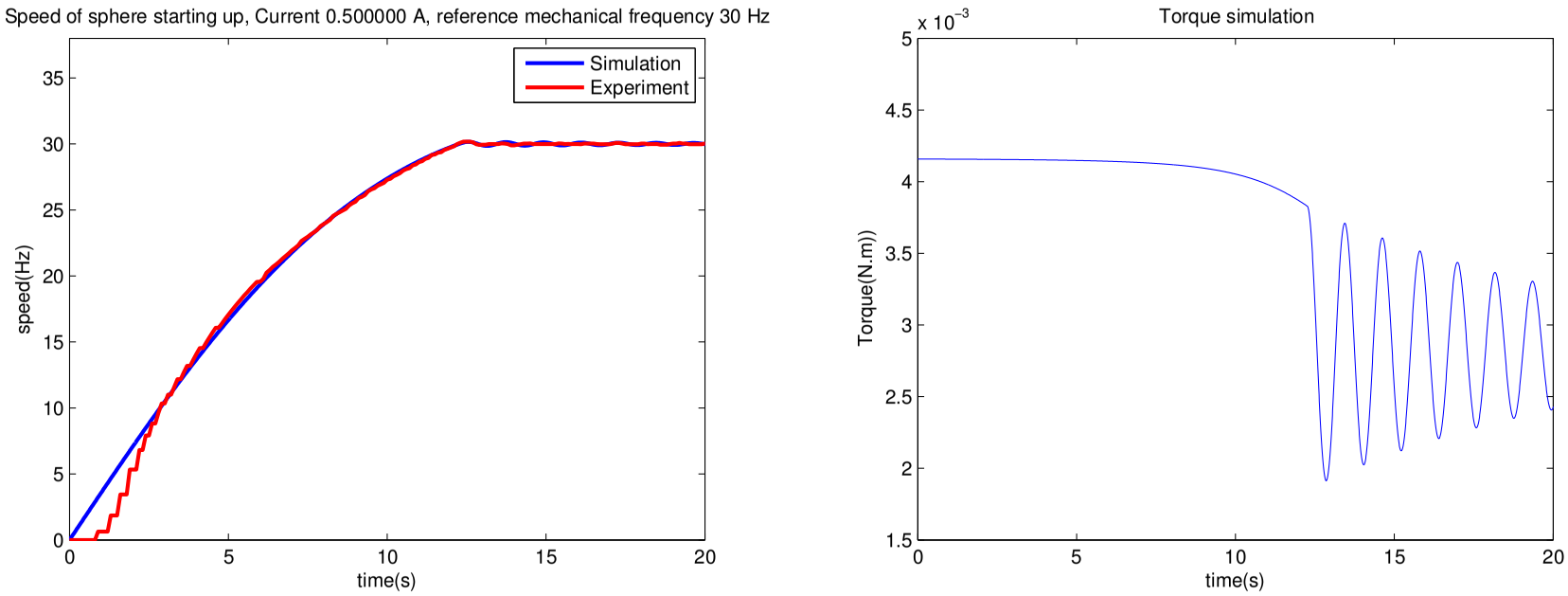

(a) (b)

Figure 5-18: Starting transient speed data under excitation current of 0.5A.
(a)Angular Speed of Experiment and Simulation Data; (b)Torque curve.

Chapter 6

Speed Control of Reaction Sphere with One-axis Hysteresis Drive

In the design of the 1D-MSRS, hysteresis motor is used due to its ability of constant torque, self-start, and quiet operation. These properties are very important for motors in precision applications such as inertial actuators for satellite attitude control. However, hysteresis motors also have their drawbacks. As we have shown in the previous chapter, the speed of the motor fluctuates slightly above and below the desired synchronous frequency while it operates. This speed oscillation occurs when the motor speed is getting close to the synchronous speed. This motor speed variation about the desired synchronous speed is known as hunting.

The hunting phenomena of hysteresis motor may cause errors which could hinder system performance. For example, when a torque is need to provide to the satellite by the reaction sphere, this hunting behavior can cause the whole satellite oscillates, and thus impair the pointing accuracy of the satellite.

In addition, since magnetic suspension eliminated all mechanical frictions, the torque needed for the reaction sphere during steady state operation is very low. Therefore we should be able to reduce the current amplitude in the motor winding when the sphere reaches synchronous speed depending on the torque requirement. This adjustment in current can reduce the copper loss of the 1D-MSRS in steady state operations.

In this chapter of the thesis, the hunting behavior of the hysteresis motor for the 1D-MSRS is studied first. After that, a speed control strategy is proposed for actively monitors motor activity and compensates for the hunting. With the sphere's speed under closed-loop control, the motor current amplitude can be reduced when the sphere is running synchronously and thus reduce energy consumption. This control method is tested on the 1D-MSRS hardware and simulated by the hysteresis motor model for 1D-MSRS presented in the previous chapter.

6.1 Linear model of the hunting

In this section we study the hunting dynamics of the hysteresis motor. A linear second-order model is used to fit the hunting dynamics of the hysteresis motor. This linear model is used to design the controller for hunting suppression.

Figure 6-1 shows the open-loop step response speed data for the 1D-MSRS under an excitation current of fixed peak value 0.35 A. In the measurement, we step the reference speed, i.e., a half of the electrical speed, from 0 to 20 Hz, and recorded the speed measurement from the optical tachometer.

From the speed step response data in Figure 6-1, we can see that the hunting is happening when the motor speed is getting close to the reference speed. By looking at the enlarged plot of the speed data as the rotor speed first reaches the reference speed, we can find that the period of the speed oscillation is 1.6 s, and it takes approximately 6 seconds to damp out.

A second-order linear system is used to study the hunting dynamics of the hysteresis motor. From the parameters that we observed from the experimental data, we can calculate that the natural frequency of the fitted second-order linear system is $\omega_n = 3.93$ rad/s, and the damping ratio is $\zeta = 0.067$. The DC gain of the linear model is determined the amplitude of the hunting. As a result, the linear dynamic model that fits this hunting speed data will have a transfer function of

$$H = \frac{0.3}{s^2 + 0.53s + 15.42}. \tag{6.1}$$

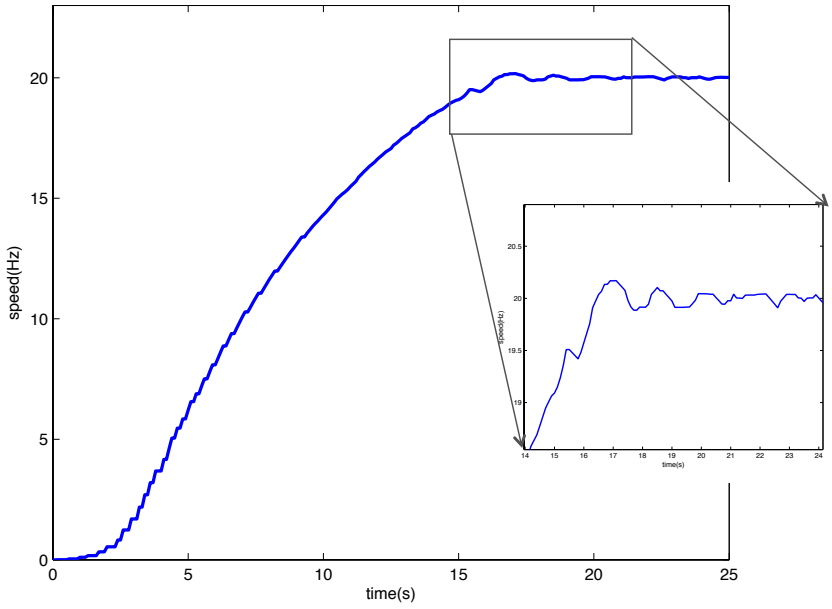

Figure 6-1: Step response of the 1D-MSRS speed with hysteresis drive. Reference mechanical speed is 20 Hz. Motor winding current peak amplitude is 0.35 A.

Figure 6-2 shows the fitted second-order linear model and the experimentally measured speed hunting data plotting together. Figure shows that the linear model basically captured the major features of the hunting dynamics.

From the measurement of the speed step response of the reaction sphere under different motor current amplitude, it is observed that the hunting of the hysteresis motor demonstrate similar frequency and damping. This linear approximation of hunting dynamics is being used to determine the controller gains of the speed compensator. The detailed controller design is introduced in the next section.

6.2 Speed control for reaction sphere

In this section the speed control design for the hysteresis motor in 1D-MSRS is presented in detail.

Figure 6-3 shows a block diagram of the speed control loop of the reaction sphere. In the 1D-MSRS hardware, the speed measurement is completed by means of a optical reflective tachometer. It will generate one TTL pulse as the dark mark on the

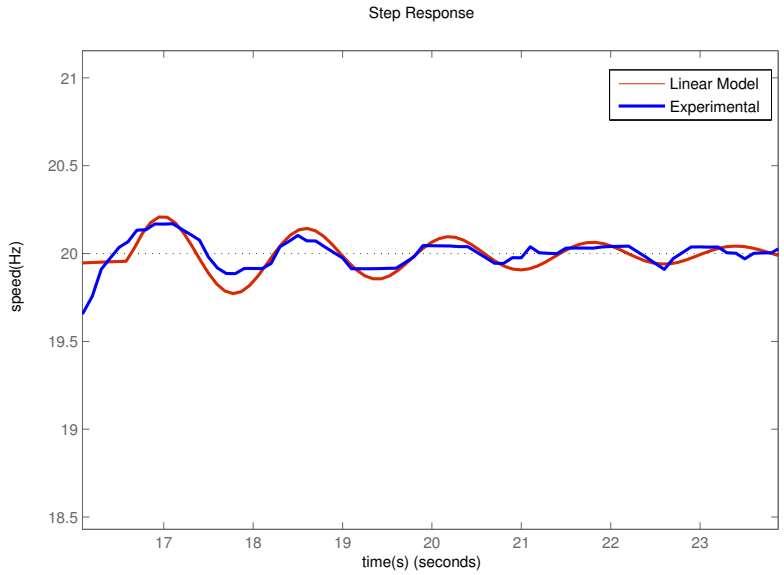

Figure 6-2: Linear 2-nd order model approximation of the hunting phenomena. Red: linear 2-nd order model. Blue: measured hunting speed data.

sphere passes through the sensor, thus one pulse will be generated per revolution. By counting the number of pulses in unity time, a measurement of the sphere's rotational speed can be achieved. This measurement is our variable of interest ω_m in the controller design (in Hz, or rev/s). The reference angular speed ω_d is a half of the electrical speed that we assign to the motor windings, which is also the synchronous speed of the hysteresis motor. Let us define the error between the reference speed and the measured motor speed to be e_ω, which is the input signal of the speed controller. The control effort in this control loop is defined to be the zero-to-peak amplitude of the three-phase excitation current, I_m. In this analysis let us call it u, denoting the control effort. This value is used in the generation of symmetrical 3-phase signal which later energize the motor windings of the reaction sphere after amplified. Note that in this system the value of u is non-negative, and it cannot go below 0.2 A in order to maintain lateral suspension. Also note that in this control system a positive control effort provides decelerating torque when e_ω is negative.

Since the hysteresis motor is a synchronous motor, the motor speed ω_m can ultimately reach the reference speed ω_d when the load torque is smaller than the hysteresis

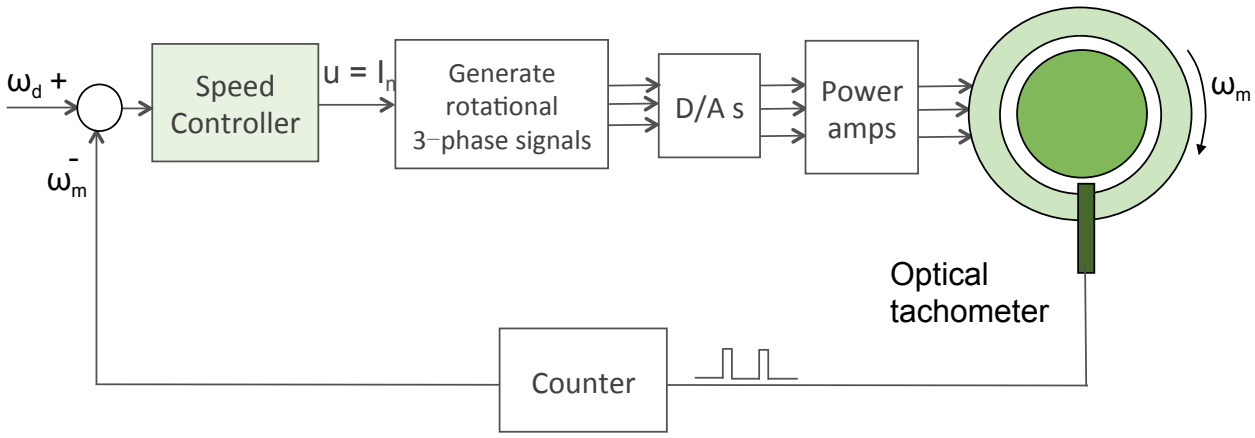

Figure 6-3: Block diagram of the reaction sphere's speed control.

torque production ability. However, there are some undesirable motor dynamics, like hunting that we demonstrated before, existing when the hysteresis motor operates, thus impair the performance of the reaction sphere. Eliminating these dynamics is one of the major goal of the speed feedback control loop.

Another target of the speed feedback control of the reaction sphere is to make a better use the electrical power. When the reaction sphere operating in open-loop, the excitation amplitude of the currents in motor windings I_m is fixed. As shown by the data in Figure 5-12, this value is directly related to the rise time of the sphere's speed step response, thus a relatively large I_m value is desirable during the starting phase to reach a short rise time. However, after the sphere's speed reaches the reference speed, the motor current amplitude needed for maintaining the speed is much smaller than the desired value of I_m when the sphere is accelerating. Feedback control of the angular velocity of the reaction sphere can make the current amplitude I_m change with the speed error, thus save a lot of power when torque production to the sphere is not needed while maintains a good torque production ability when the sphere is accelerating.

To sum up, there are three requirements on the speed controller design for the reaction sphere: (a) suppress the hunting dynamics of hysteresis motor; (b) make the motor reaches the desired angular velocity with minimum rise time; and (c) reduce the power consumption when no acceleration torque is needed. In the speed controller

design for 1D-MSRS, these three specific requirements are being considered.

In the following, let us focus our discussion on the controller design of this speed control loop for the 1D-MSRS. When the reaction sphere is starting up or breaking, it is desired that the motor can catch up with the reference angular velocity as fast as possible. In optimal control theory, the minimum time problem can be solved by means of Pontryagin's minimum principle [31], especially in the presence of constraints for control effort signals. The result shows that a bang-bang controller, which in this case allows the motor accelerates with its maximum available control effort to the desired speed, is the best mechanism for achieving minimum speed rise time. For the 1D-MSRS, this requires the motor to operate in open-loop with the maximum allowed excitation amplitude, which allows the motor to accelerate or decelerate with its maximum ability.

In order to add active damping to the system to eliminate hunting, a PD controller with a low-pass filter for noise rejection, or a lead filter, is used for the speed control when the hunting is happening. Define the maximum available control effort is u_{max}. Then the control law can be written as:

$$u = \begin{cases} u_{max} & \text{if } e_\omega > \Delta \text{ or } e_\omega < -\Delta \\ u_{lead} & \text{if } -\Delta < e_\omega < \Delta \end{cases} \tag{6.2}$$

In this controller, Δ is a small constant number that we define, which sets the threshold of the controller change. It can also be understood as the hysteresis band of the bang-bang controller. The controller activity is obvious: when the error' s absolute value is larger than the defined threshold Δ, the controller is using its maximum ability to reduce the error. When the error is small and within the boundary of Δ, which means the motor speed ω_m is close to the reference speed ω_d, the lead controller is activated to add additional damping to the system to get rid of the hunting. When the speed error is very small, then the control effort signal is almost zero since it is a linear filter. In this way, all the three goals of the speed control can be achieved.

Let us then consider the design of the lead compensator in the above equation.

The compensator has a form of

$$\frac{U_{lead}(s)}{E_{\omega}(s)} = K_p \frac{\alpha\tau s + 1}{\tau s + 1}. \tag{6.3}$$

To determine the values of the parameters in the above transfer function, the linear model approximation of the hunting described in the previous section is used. From the model of hunting dynamics given in Equation 6.1, we can find the speed oscillation that we want to damp out has a frequency of $\omega_n = 3.93$ rad/s. In the controller design for the reaction sphere, we selected a cross-over frequency of $\omega_c = 8$ rad/s for the speed control loop, and a typical separation ratio $\alpha = 10$ is selected for the lead compensator. By arranging the phase peak of the lead compensator at the desired crossover frequency, we can calculate the value of τ by

$$\tau = \frac{1}{\omega_c \sqrt{\alpha}} = 0.04 \text{ s}. \tag{6.4}$$

The K_p value is selected to be 3.5 to let the loop crossover at the desired crossover frequency. As a result, the lead compensator for the reaction sphere's speed regulation is

$$\frac{u_{lead}(s)}{E_{\omega}(s)} = 3.5 \frac{0.4s + 1}{0.04s + 1}. \tag{6.5}$$

The simulation and the experimental measured speed data of the reaction sphere based on this controller design are presented in the following sections.

6.3 Simulation of speed control

In this section the simulation of the speed control of the reaction sphere is presented. The model that is being used in the simulation is the Matlab/Simulink model of the reaction sphere based on the equivalent circuit model of hysteresis motor. Figure 6-4 shows the Simulink model of the sphere's closed loop control. The sub-model shown in the figure is the model for the motor dynamics, which is being discussed in the chapter 5. The controller that this model demonstrated follows the design shows in

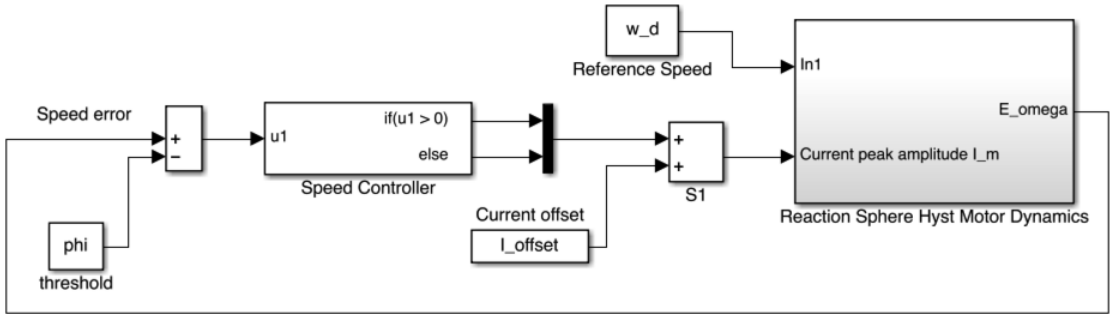

Figure 6-4: Simulink diagram of speed closed-loop control for reaction sphere.

the previous section.

In the implementation of the controller in simulation, a current offset of 0.2 A is added to the control effort signal to maintain the lateral suspension for the bearingless motor, and to produce a torque to compensate the air drag when the sphere reaches synchronous speed. The maximum allowed control effort u_{max} is selected to be 0.3 A, therefore the maximum of the current amplitude is set to be 0.5 A. The controller threshold value Δ is selected to be 1 Hz.

Figure 6-5 shows a simulation result of the step response of the reaction sphere speed. The current amplitude is $I_m = 0.35$ A. The simulation result of the closed-loop reaction sphere speed step response is shown in Figure 6-6, and the corresponding control effort signal u, which is also the excitation current amplitude I_m, is shown in Figure 6-7.

Comparing the simulation results in Figure 6-5 and 6-6, we can see that the controller can effectively damp out the reaction sphere's speed hunting, and also drives the sphere reaches the synchronous speed with a smaller rise time.

The controller described in the this chapter is also implemented in the real-time controller for the 1D-MSRS, and experiments of the closed-loop control for the reaction sphere's rotational speed are carried out. Figure 6-8 shows a comparison between open-loop acceleration speed data and the closed-loop controlled speed data. The cor-

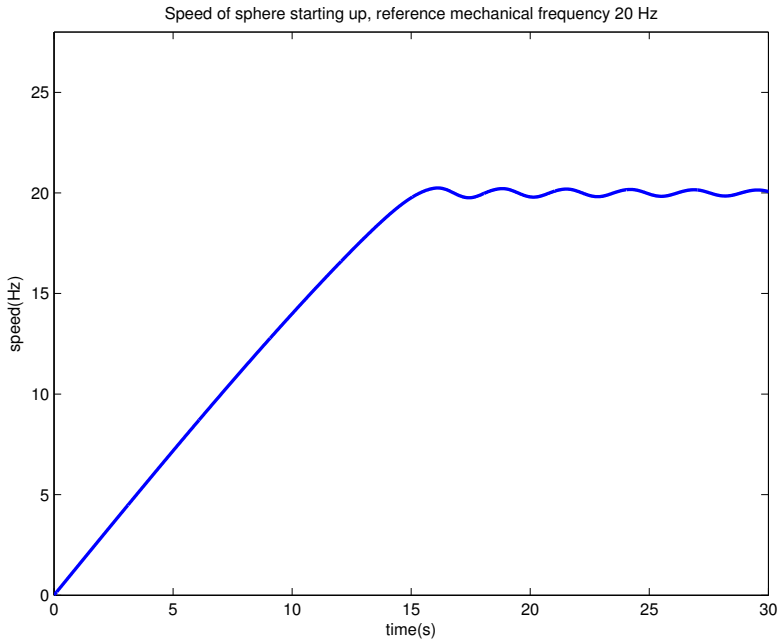

Figure 6-5: Reaction sphere open-loop speed simulation with current 0.35 A.

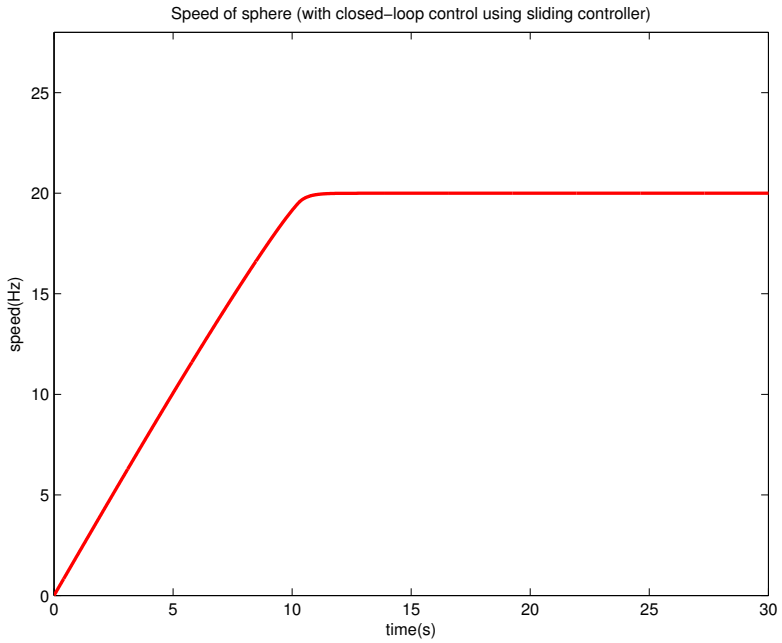

Figure 6-6: Reaction sphere closed-loop speed simulation.

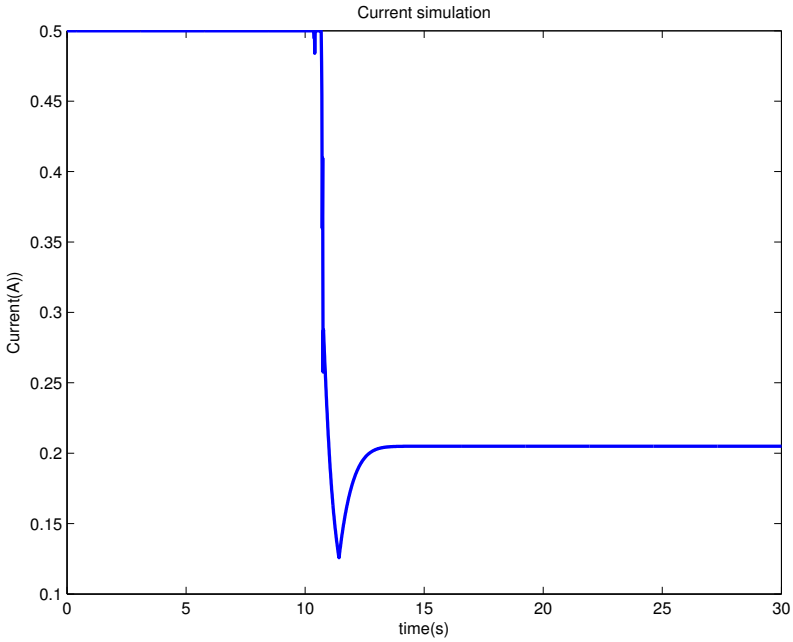

Figure 6-7: Reaction sphere closed-loop simulation of current change.

responding current signal is shown in Figure 6-9.

6.4 Experiment of speed control

From the speed data shown in Figure 6-8, we can see that the closed-loop control of the reaction sphere's speed effectively suppressed the hunting that exists in the open loop step response. It also enables the sphere to reach the reference speed faster since a larger control effort is used during the acceleration period. The current data in Figure 6-9 shows that the peak value of the 3-phase current in the motor windings reduced to 0.2 A when the reaction sphere is operating in steady state. The experimental data shows the effectiveness of the control design.

When the reaction sphere is under the steady stator operation at a mechanical speed of 30 Hz/1800 rpm, the rms current value in the motor windings is $\frac{\sqrt{2}}{2}0.2 = 0.14$ A, and the measured rms voltage of the motor windings is 8.2 V. Since the suspension current rms values are just 0.01 A, we neglected the suspension winding power consumption in this calculations. There for the electrical power dissipation in

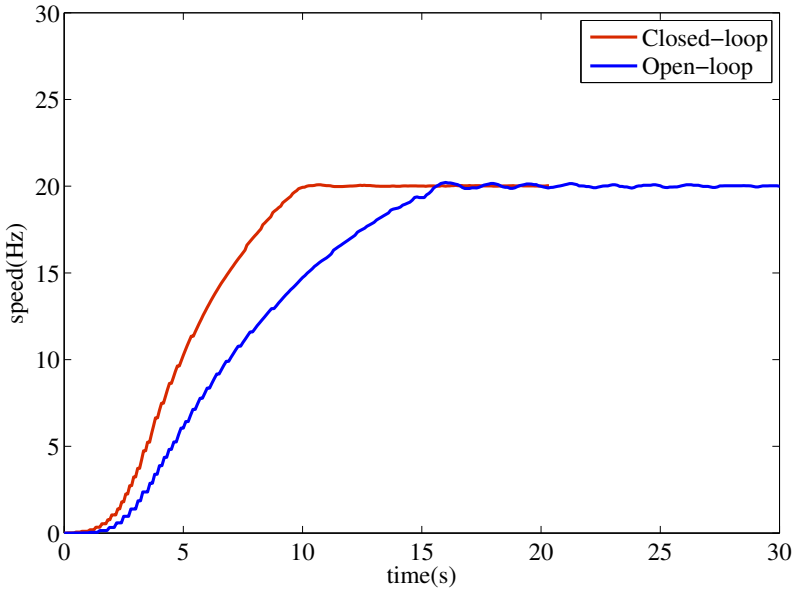

Figure 6-8: A comparison of experimental open-loop step response data and the closed-loop step response data of reaction sphere. The open-loop step response is measured under a peak current value of 0.35 A. The feedback controller design of the closed-loop system follows the introduction in previous sections.

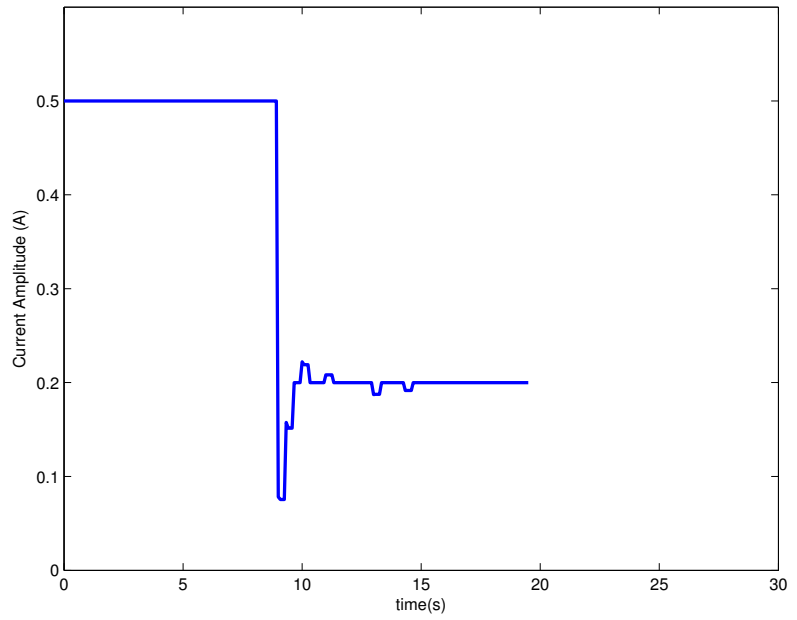

Figure 6-9: Experimental closed-loop control effort data (peak amplitude for motor current) of reaction sphere start up.

the motor windings under steady state is $P = 3 \times 0.14\ A \times 8.2\ \text{V} = 3.44\ \text{W}$.

6.5 Summary

This chapter introduces the feedback control for the speed of the reaction sphere. This control loop is designed to reach three goals: (a) suppress the hunting dynamics of hysteresis motor; (b) make the motor reaches the desired angular velocity with minimum rise time; and (c), reduce the power consumption when no acceleration torque is needed.

First, the hunting dynamics of the reaction sphere is fitted by a linear second-order system. This model is used to design the speed controller for the reaction sphere. Then the detailed controller design is introduced. The controller is a combination of a bang-bang controller and a linear lead compensator. After that, the simulated and measured speed data with and without the speed feedback control are demonstrated. The data verified the effectiveness of the speed control design. All the three goals for the speed control are achieved, specifically the hunting of the reaction sphere being effectively suppressed.

Chapter 7

Three-dimensional Spherical Motor Design Concepts

In the prior chapters of this thesis, the design, modeling and test results of the 1D-MSRS are presented. In this thesis, we also extended our scope to the conceptual design of a 3D version of MSRS by studying the possible motor driving principles and magnetic design concepts for spherical motors. This chapter gives a summary of our exploration in this direction.

In this chapter, first the prior works on the development of spherical motors are studied. After that, we evaluated several different kinds of motor driving principles, and discussed that whether they are suitable for the development of a 3D spherical motor. Finally, several spherical motor magnetic design concepts for reaction spheres and for other applications are presented.

7.1 Introduction and prior arts in spherical motor design

In the past several decades, there is a growing interest in high-speed, servo-controlled spherical actuators in multiple degrees of freedom, mainly for applications in robotics and automated manufacturing. Achieving multi-degree-of-freedom (DOF) motions

by separate motor/actuators for each axis is not adequate for some applications. As a result, researchers begin to explore the design and development of various types of multi-dimensional spherical motors for the spacecraft attitude control problem, enables us to directly drive several rotational DOFs simultaneously without suffering the effect of gyroscopic coupling between axes and backlash and nonlinear friction from gears.

In this section, some major developments of multi-DOF spherical motors are reviewed. Table 7.1 shows a summary of the reported spherical motor designs that we have studied. They are classified into different categories according to their driving principles. In the table, we also briefly show the advantages and limitations of the motor type for spherical actuator design. More discussions will be presented in the next section.

An early spherical motor is of a induction type, which was conceptualized by Vachtsevanos et al. in 1987 [39]. Figure 7-1 shows the motor winding in this design. A detailed analysis was given by Devay and Vachtsevanos [40], where the analytical expression of the torque production about one axis is derived. This design arranges windings in a spherical coordinate, therefore all the rotor surface area are involved in the torque production. However, it is difficult to realize a prototype of this kind because of its complexity in mechanical and winding design and manufacturing, which requires inlaying all three transversing windings on the inner spherical surface of the stator.

A spherical induction motor with two degrees-of-freedom is reported by Dehez et al. in [41]. Figure 7-2 shows a diagram of the two-DOF induction motor designed by Dehez. In this motor, a combination of four linear induction stator segments and one piece of 2-DOF induction stator segment with slots in two directions are used to generate torques about two axes.

Kumagai and Hollis [32] developed a 3-DOF spherical induction motor for mobile robot application. The multi-DOF motion is realized by means of a combination of several linear motors. Figure 7-3 shows a photo of the spherical motor they have implemented. It has 4 stator segments for linear induction motor, and the rotor is

Table 7.1: A summary of spherical motor designs.

Motor type	**Drive Principle**	**Advantages**	**Limitations**	**Related literature**
Induction motor	Torque production by eddy current in rotor.	Linear operation under vector control. Suitable for high speed.	Not efficient for small motor applications.	Devay et al. [10], Hollis et al. [32]
DC motor	Uses Lorentz .force for torque production.	Linear, easy to control, uniform torque constant.	Limited torque capability.	Kaneko [9].Kim [33]
PM synchronous motor	With permanent magnets on rotor and windings on stator.	Synchronous operation; good torque ability; linear current-to-torque relation	Cogging torque. Cannot self-start. Complicated rotor structure.	Wang [12], Onillon [14], Yano [34], Yan [35]
PM based stepper motor	Use multiple electromagnets and PMs for torque generation by turning on and off the electromagnets accordingly.	Open-loop control is available. Relatively simple structure.	Sophisticated switching scheme is required for spherical stepper.	Stein [36]
Reluctance motor	use saliency and reluctance force for torque production	large torque density and simple structure	Nonlinear current/torque relation; large torque ripple	Lee [37]
Ultrasonic motor	Stator generates vibration in the ultrasonic frequency range, and Uses frictional drive by elliptical motion.	High responsiveness, moderate torque production, compactness.	low speed, hysteresis.	Toyami [38]

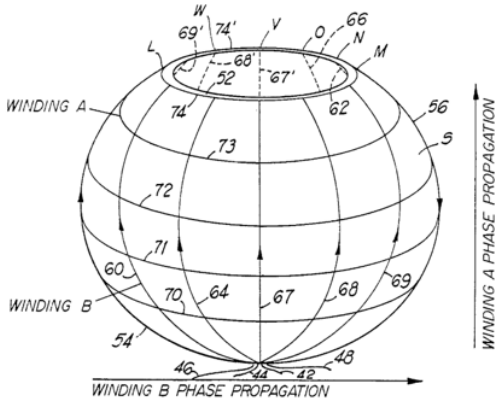

Figure 7-1: Winding design of the spherical induction motor by Devay and Vachtsevanos. Figure taken from [40].

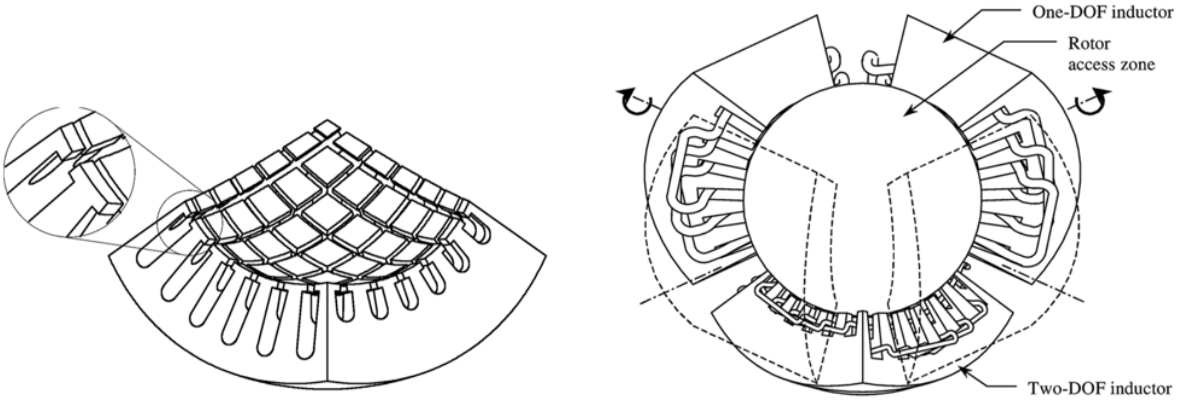

(a) A 2-DOF induction stator segment.

(b) Spherical motor design.

Figure 7-2: The two-DOF spherical induction motor presented by Dehez et al. Figure taken from [41].

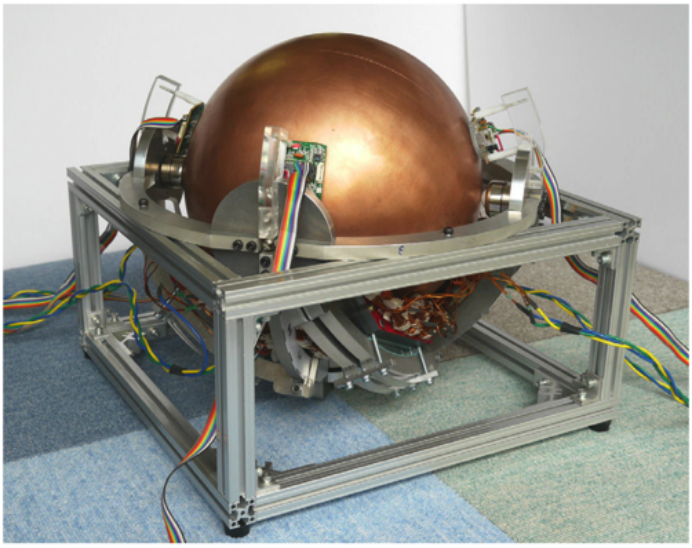

Figure 7-3: Spherical induction motor for mobile robot presented by Kumagai and Hollis. Figure taken from [32].

a two-layered spherical shell whose inner layer is made of steel and outer layer is of copper. Servo control for this 3D spherical motor is also realized in their work.

A DC spherical motor design with three-DOFs in rotation was demonstrated by Kaneko et al. in 1988 [9]. Figure 7-4 shows the winding diagram of their design. This motor can spin continuously about one axis, and has a maximum inclination of 15^o in other directions.

Lee et al. proposed an spherical motor design based on variable reluctance (VR) stepper motor [37]. Figure 7-5 shows the design of this motor. This spherical motor operates by the principle of variable reluctance. When the motor is operating, the stator coils are energized individually. A magnetic field is established which creates magnetic energy in the air gaps. The magnetic energy is a function of the relative position of the rotor and stator. The motion of the VR spherical motor is generated as the rotor tends to move to a position such that the energy in the air gap is minimized.

A PM based spherical stepper motor is designed and built by Stein et al. from Johns Hopkins University [36]. Their work focuses on the mathematical optimization of the magnetic pole configuration and control schemes. Figure 7-6 shows the stator and rotor assemblies of the spherical stepper motor they developed.

A permanent magnet synchronous type spherical motor is proposed by Yano in

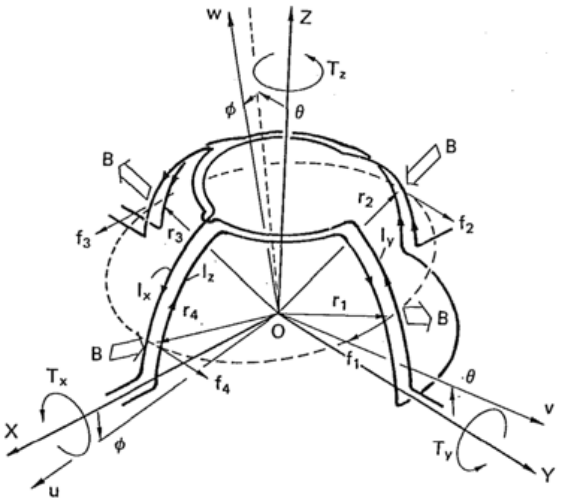

Figure 7-4: The winding configuration of the spherical DC motor presented by Kaneko et al. Figure taken from [9].

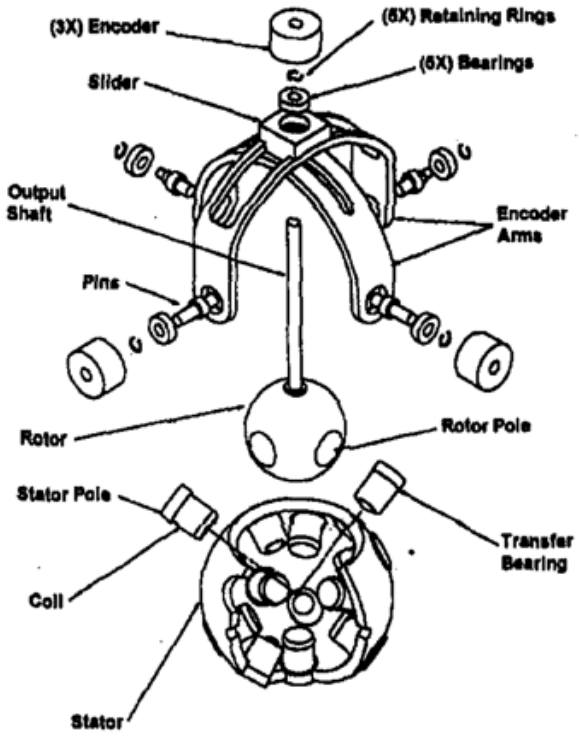

Figure 7-5: The design of the variable reluctance spherical stepper motor by Lee et al. Figure taken from [37].

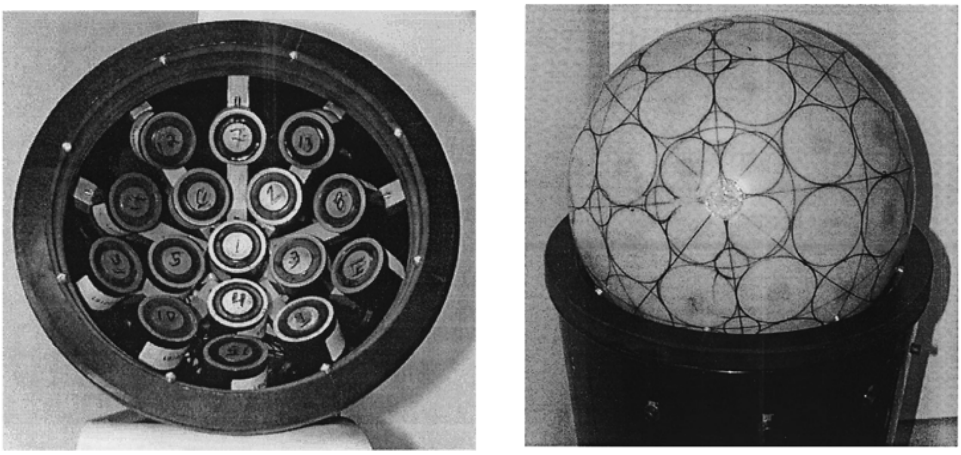

(a)Stator assembly (b) Rotor assembly.

Figure 7-6: Spherical PM stepper motor designed by Stein et al. Figure taken from [36].

[34]. Figure 7-7 shows a picture of their motor implementation. There are two concentrated windings A and B. By driving the two coils with AC current, a torque can be generated around the mechanical shaft.

Another spherical PM synchronous motor design with all three rotational degrees of freedoms is the ESA reaction sphere described in Onillon et al. [14]. Figure 7-8 shows the design of this reaction sphere. The distribution of magnetic poles on the sphere follows the vertices's of the regular polyhedrons. The rotor has 8 poles, and the stator has 20 poles. This is a spherical motor with all driving directions.

Toyami et al. have developed a spherical motor by ultrasonic motor's technology [38]. This motor uses a different driving principle: its torque is generated by ultrasonic vibration. Figure 7-9 shows a schematic for its design. Comparing with its electromagnetic based counterparts, this motor wins for its high torque density and fast response, and has a good potential for many special low speed applications. However, contact mechanics in the motor will likely limit its lifetime.

Above is a brief study on the literatures on the development of spherical motor. This is still an active area with many ongoing research carrying on. With the advance in control and computation tools, we believe that more powerful spherical motors designs will be carried out and one day it may be widely used in industry.

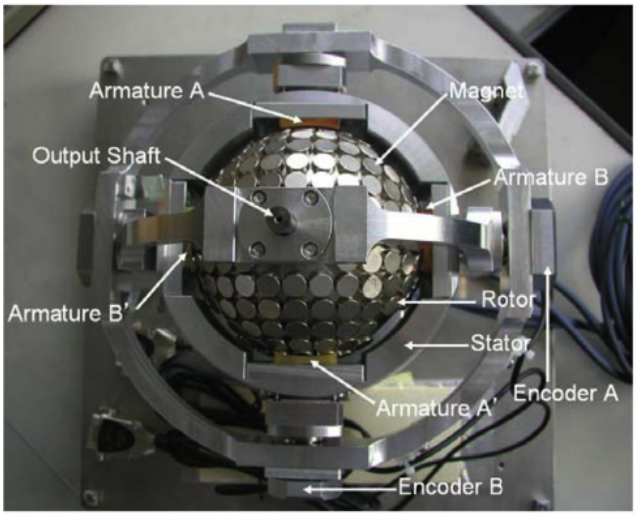

Figure 7-7: The AC synchronous spherical motor by Yano et al. Figure taken from [34].

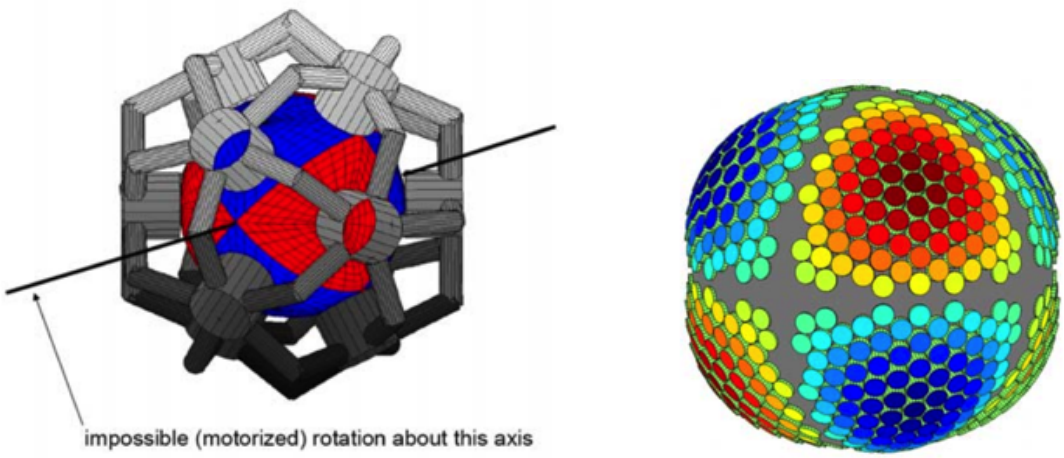

(a)Stator design. (b) Rotor design.

Figure 7-8: Reaction sphere designed presented by Onillon et al. Figure taken from [14].

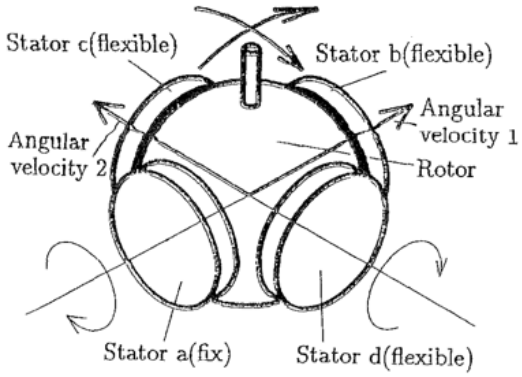

Figure 7-9: The untrasonic spherical motor by Toyami et al. Figure taken from [38].

7.2 Discussion and design concepts

In this section, we will briefly discuss about these motor principles for spherical motor application and whether they are suitable for a high-speed reaction sphere application. We will also present several magnetic design concepts for spherical motors, mainly for reaction sphere application.

7.2.1 Motor driving principles

In this part of the thesis, we will discuss several motor driving principles, and evaluate their advantages and disadvantages for a reaction sphere design.

Reaction spheres require the 3D motor to produce torque in all the three degrees-of-freedom and have unlimited angular range. Characteristics of high speed, moderate torque, smooth running are preferred, and the torque production, or motor angular speed of the 3D motor, needs to be actively controlled.

The motor types which we will evaluate in this section include DC motor, induction motor, PM synchronous motor,hysteresis motor, reluctance motor. We also listed two new motor types by combination of different basic motor types: induction-hysteresis hybrid motor and PM-hysteresis hybrid motor.

DC motor

A so-called DC motor typically has a stationary set of magnets in the stator and an armature with a series of two or more windings of wire wrapped in the slots around iron pole pieces with the ends of the wires terminating on a commutator. This kind of motor is commonly used in many applications when servos are required due to its advantages such as low initial cost and simple control of motor speed. This simplicity in control is greatly favorable for a 3D spherical motor that involves sophisticated magnetic designs and speed control is required.

However, brushed DC motors are surely not suitable for reaction spheres development because it requires regular maintenance and its low life-span for high intensity uses. The reaction sphere is for satellite use, therefore regularly replacing the brushes and springs is almost impossible.

Induction motors

An induction motor is an AC asynchronous motor in which the electric current in the rotor needed to produce torque is induced by electromagnetic induction from the magnetic field of the stator winding. Three-phase squirrel-cage induction motors are widely used in industrial drives because they are rugged, reliable and economical.

The vector control scheme makes the speed control of induction machines accessible, even under sensorless conditions. This also enables this motor to be used for a 3D spherical motor design. In a 3D spherical motor, torque generation is required in all directions, therefore either wound type or squirrel-cage type rotor will not be suitable, since they all regulate the eddy current in certain direction.

One possible design for an all-degree-of-freedom actuator using induction design is the spherical motor built by Hollis et al. in [32]. In this design, the rotor is a two-layer spherical shell, with its outer layer made of conductive material such as copper, and its inner layer made of ferromagnetic material. This rotor design enables eddy current in all directions in the conductive shell, and further making torque generation in all directions to be possible.

The major limit to this kind of spherical motor that prevents it being directly used for a reaction sphere is its driving efficiency and torque ability. Since eddy current is used for torque generation, there will be copper loss induced, making this motor not as effective as some other motor types. Besides, in this design the effective area on the rotor surface is very small, which is not good for the torque ability of this spherical motor. Moreover, in the spherical motor design introduced above, the direction of the eddy currents are not regulated. As a result, not all eddy currents contribute to the torque production, and some may induce vibrations. Significant works in designing the magnetic configuration and control schemes are required to improve the performance of this spherical motor before it can be used for a high speed reaction spheres.

Permanent magnet motors

A permanent magnet (PM) motor is a kind of synchronous motor. It consists of a multi-pole rotor with permanent magnets, and a wound stator to generate a rotational magnetic field.

Permanent magnet synchronous motors have several distinct advantages: high efficiency, high power factor, good torque density, and linear current to force relation. These characteristics of the PM motor makes them being widely used for small motor applications. The major limitation of PM motors, aside from the high costs of NdFeB magnets, is the fact that PM motors do not have self-starting torque under open-loop drive. During the starting period, the magnets may generate an oscillatory torque, which reduces the motor's starting ability. In industrial applications, these motors are usually assisted with cage windings so that they can run in induction mode during starting.

Among many spherical motor designs that we have studied in the previous section, many of them are of PM motor type, such as the JHU spherical stepper [36] (if driven with AC excitation) and the ESA reaction sphere [14].

However, many optimizations are needed to make these motors work as a reaction sphere. First is the cogging torque of PM motor. In space applications, vibrations

will induce jitter. Therefore in the motor design the cogging torque of PM motor needs to be addressed. When the stator has teeth and slots to constrain the magnetic field, the interaction between the permanent magnets in the rotor and these structure will produce a ripple in torque production when the motor is operating. This torque is undesirable, especially for precision applications such as the actuator for satellite attitude control.

Another challenge to the PM motor being used for space application is its relatively complicated rotor structure and the corresponding rotor strength. All the prior designs of spherical PM motors that we have studied demonstrate sophisticated rotor structures, this may lead to imbalance of mass in the rotor. Besides, since for high speed electric machines the speed limitation is often the centrifugal stress of the rotor. If the magnets are mounted on the surface of the rotor, as designs in JHU spherical stepper [36] and the ESA reaction sphere [14], the rotor's strength may be relatively low and will become a major limitation for motor speed.

Hysteresis motors

Hysteresis motor is a kind of asynchronous/synchronous AC motor, which uses the magnetic hysteresis of the rotor material for torque production. Hysteresis motors have a lot of good properties: simple structure, self-start, smooth operation, and allows high rotor strength. All these properties makes this motor to be promising in many applications where high speed, quiet operation motor is needed.

To the best of our knowledge, there is no spherical motor developed that uses hysteresis drive, and this thesis presents the first project that explores the possibility for a hysteresis motor for reaction sphere applications.

The rotor of the spherical hysteresis motor need to be a sphere of uniform magnetically hard material, either as a solid sphere or a spherical shell. This rotor has a simple and balanced structure, and will have good rotor stress limits since solid material is used for the rotor construction. However, significant consideration is needed for the magnetic pole design for this motor.

Reluctance motor

A reluctance motor is a type of electric motor that induces non-permanent magnetic poles on a ferromagnetic rotor. Torque is generated through the phenomenon of magnetic reluctance. This kind of motor can deliver very high power density at low cost, making them ideal for many applications. Its disadvantages are the high torque ripple induced by the rotor's saliency.

One literature reported a variable reluctance type spherical motor [37]. However when this type of motor is being considered for the design of a reaction sphere, its inherent nonlinearity will make the servo control very challenging. Special consideration will needed to take care of this difficulty. Besides, it large torque ripple may makes this motor not very suitable for the application of reaction sphere, where quite and smooth motor operation is desired.

Induction + hysteresis motor

In the discussions above, we evaluated several classical motor driving principles. In this study, we found that the advantages and limitations of several motor types are sometimes complimentary. Therefore there is a chance to combine different motor concepts to let the advantages of one motor type to compensate the drawbacks of another one, and result in a motor that have a good overall performance for a typical application. In this thesis let us call this kind of motor "hybrid motors".

One possibility of these hybrid motor designs is a combination of induction motor and hysteresis motor. The rotor of this hybrid motor can use a two-layer spherical shell design similar to the rotor design for induction type that we discussed before. The outer layer of the spherical shell should be made of conductive material such as copper, and the inner layer can be made out of magnetically hard ferromagnetic material. In this way, the spherical motor will become a combination of induction motor and a hysteresis motor. The torque generation of this spherical motor uses these two principles: the eddy current mainly in the outer shell and the magnetic hysteresis in the inner shell. During the start up of the spherical motor, the hysteresis torque

generated by the magnetization of the ferromagnetic core and the induction torque generated by the eddy currents, mainly in the conductive shell, are working together to help the sphere accelerates. As the sphere's speed gets close to the synchronous speed, the hysteresis torque can bring the sphere to the synchronous operation, and the eddy current in the outer shell decays. As a result, this hybrid motor is a synchronous motor.

To the best of our knowledge, no literature has addressed this kind of hybrid motor design and its performance. Experiments and simulations are needed to evaluate the performance before it goes further for a 3D spherical motor development. However, by speculating based on our understandings, we believe that this hybrid motor drive can inherit the advantages of a hysteresis motor, namely, self-start, quite operation, and simple and balanced rotor design, and can have a better linearity and torque ability. Besides, comparing with a pure induction motor, we expect this kind of hybrid motor can have a better efficiency, since the eddy currents decay when this spherical motor reaches synchronous speed, therefore the iron loss due to eddy current will be eliminated when the spherical motor operating in steady state.

The challenge for designing a spherical motor with this driving principle is the same with a pure induction motor and a pure hysteresis motor, that is, how should we configure the winding patterns and the magnetic poles. This is a challenging and interesting problem, and some discussions and design concepts that address this question are presented in the next section.

Hysteresis + PM motor

Another possible hybrid motor design that has a potential for a high-speed spherical motor development is a combination between permanent magnet motor and hysteresis motor. To our knowledge, this motor design is propose by Rahman et al. in [42] for electric vehicles application. Figure 7-10 shows a cross-section diagram of the PM-hysteresis motor designed by Rahman. The rotor of the motor is a piece of a cylindrical ring-shape hysteresis material, with NdFeB permanent magnet inserted in the pole arc segments inside the inner surface of the hysteresis ring.

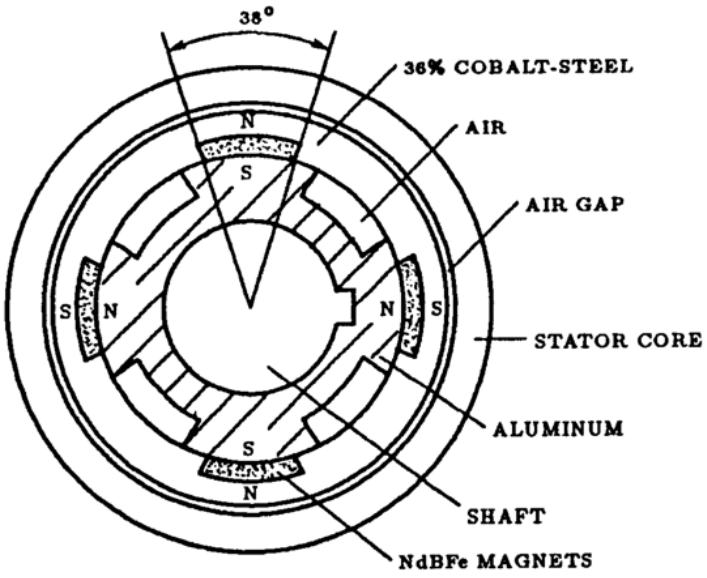

Figure 7-10: A cross-section of the hybrid hysteresis and permanent magnet motor proposed by Rahman et al. Figure taken from [42].

Experimental test results of this hybrid motor are presented in the paper [42]. According to the author, this hybrid motor demonstrated better torque performance than a pure hysteresis motor of the same dimension. It also demonstrated self-start ability, which does not apply for a pure permanent magnet synchronous motor.

Based on the result presented in the reference, we think that this hybrid motor may have the potential to demonstrate good performance for an application of reaction wheel or a reaction sphere. The torque generation of this hybrid motor is based on the principles of both fundamental motor types. When the motor is starting up, the motor torque consists of the hysteresis torque, eddy current torque, and an oscillatory torque produced by the permanent magnets. The motor can have self-start ability when the accelerating torque is larger than the oscillatory torque and frictions. At the synchronous speed, the motor torque is comprised of the hysteresis and permanent magnet torques. It has been shown in the paper that the hysteresis torque has a smoothing effect to the cogging torque, therefore this hybrid motor demonstrated much smoother operation comparing with its PM counterpart. For the rotor's structure, with the permanent magnets lying in the inner surface of the hysteresis rotor, the smoothness of the rotor outer surface is not impaired. Also, in

this design, the hysteresis ring basically acts as a retaining ring of the rotor surface-mounted permanent magnets, which is good for high speed application since the strength of the rotor won't suffer from the rotor's structure.

Compared with some other motor concepts, the hybrid motors are much less developed. Much more study are needed to reach a good design of this hybrid motor. There is a huge design space where a lot of optimizations are needed to reach a good motor design of this kind. More discussion about the magnetic poles are presented in the next section.

7.2.2 Magnetic design concepts

In this section we present a discussion on magnetic designs for spherical motors. In this thesis, the magnetic designs for spherical motors, mainly in magnetic pole distributions and stator geometry, are classified into three categories. They are: (a) combination of linear motors, (b) Stator of salient and distributed poles, and (c) meshed distribution of motor windings. In this section, these types of motor designs are introduced accordingly.

A combination of linear motors

In this section, the 3-axis spherical motor design by combining linear motors is discussed. In this design, several curved linear stator segments are placed around the spherical rotor. Each stator segment can generate a shear force on the sphere in the direction of the segment, and therefore the rotor sphere can be driven about all axes. Figure 7-11 shows such a spherical motor design with different stator segments configurations. This concept follows the spherical induction motor design by Hollis et al. [32].

In a 3D spherical motor, torque generation should be available in all directions. There are three rotational degrees-of-freedom for the spherical rotor. As a result, at least three torque directions are needed to span the space. Ideally, the total torque generated to the rotor will be a linear combination of the torques generated by the

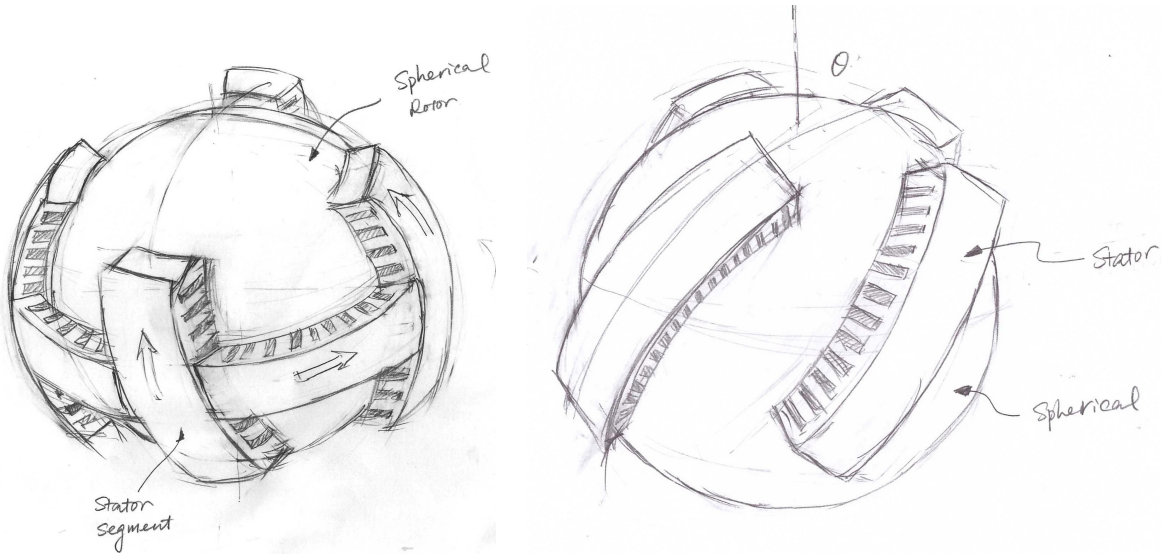

Figure 7-11: Possible stator segments configurations uses a linear combination of linear motors.

stator pieces individually. Therefore a minimum of three stator segments are needed.

In this motor design, the torques are only available in the directions along the stator segments. As a result, a rotor with determined magnetic pole distribution may not be suitable. To our understanding, this kind of spherical motor design may apply to induction or hysteresis type of motors.

This is a very straight forward magnetic design to produce torques to the rotor sphere in all directions, and the experiment results of this design that shows in reference [32] verified its effectiveness. However, when the motor need to operate in high speed or need to be used in precision applications, the speed/torque capacity of this motor and its more subtle dynamics need to be taken into consideration.

There is an drawback of this motor design: the effective area on the rotor for torque generation is very small. Only the area on the rotor surface that are interacting with the stator segments are working for the torque generation. As a result, the torque density of this spherical motor may not be satisfying. We can increase the effective area by using more stator segments. However, if the stator pieces get too close to each other, the magnetic fields generated by different stator pieces may interfere with each other, and thus generate disturbance torques to the rotor. Figure 7-12 shows a flux

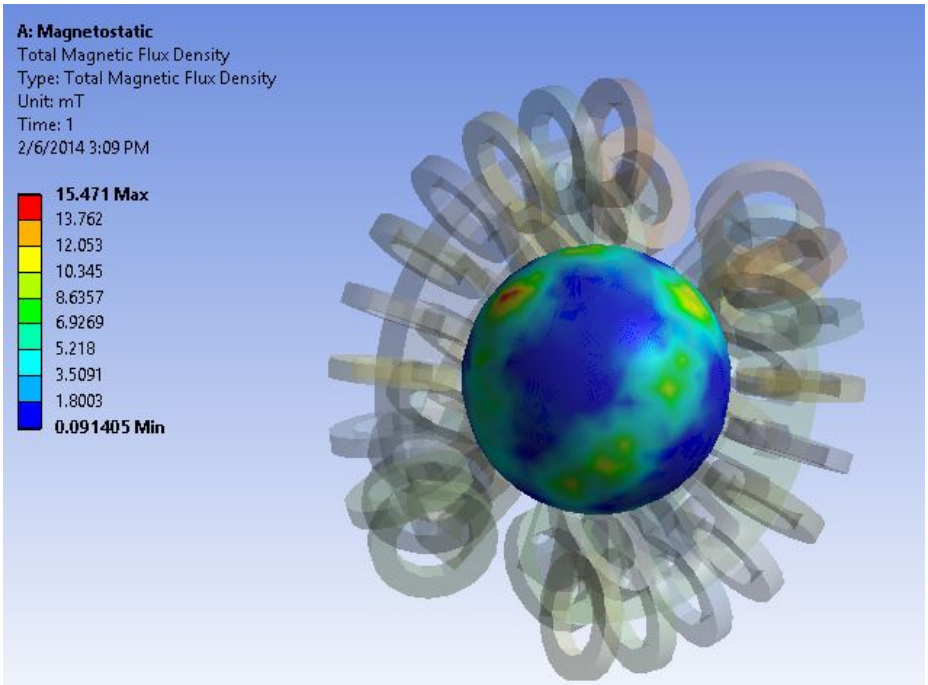

Figure 7-12: Flux distribution of spherical motor with linear stator segments. Calculated by 3D finite element method.

distribution in such a motor design calculated by 3D finite element analysis. Through this field calculation result we can see that the stator pieces are close to each other in the end of the stator segments, and the magnetic field generated by different pole pieces are having some interaction at this positions. Through field calculation for different design parameters, we found that using a smaller pole pitch in the winding design can extenuate the field disturbance.

Distributed salient stator poles

The second kind of spherical motor stator design uses distributed salient stator poles and concentrated windings. Figure 7-13 shows a cartoon of this kind of motor design. In this figure, the clear blue parts are the steel cores. Red parts are showing the coils surround the magnetic poles, and the golden part is the rotor sphere. In this design, every magnetic pole is surrounded by coil windings. By controlling the current in these coils, magnetic field can be generated. This stator design resembles the stators for commonly used DC-brushless motors, with its poles distributed in 3D.

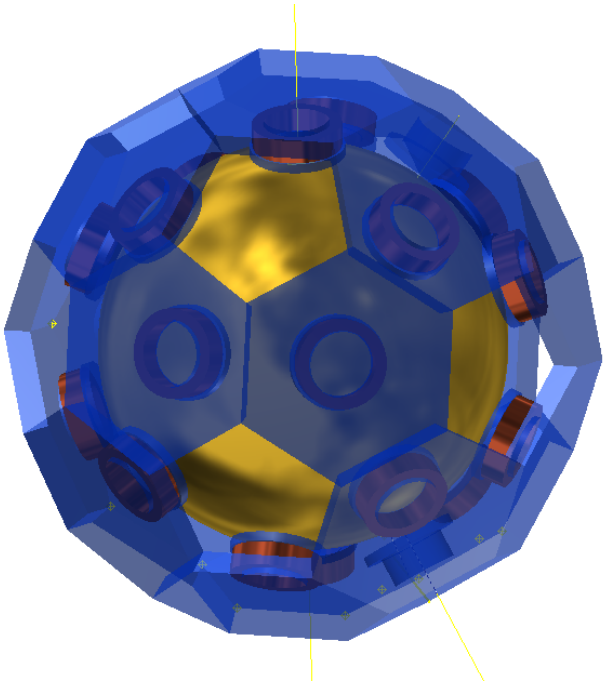

Figure 7-13: A spherical motor design with concentrated windings. Magnetic poles are distributed on the inner face of a sphere. The sphere in the middle is the rotor.

Several spherical motors developed before are of this category. In the ESA reaction sphere [14], a stator of 20 magnetic poles distributed on the spherical surface. The stator pole positions are placed on the vertices of a dodecahedron, and air core coils are used in their design in order to reach a analytical expression for torque. The JHU spherical stepper [36] and the sphreical PM motor developed by Yano [34] also follows this stator design, with their stator coils assisted by ferromagnetic cores to reduce flux leakage.

This magnetic design can be versatile. To reach a smooth motor performance, it is desirable to increase the number of poles to reach a smaller pole pitch. Whenever the poles covers the sphere surface and are distributed so that torques in all directions are available, this stator can generated torques in all direction.

All the aforesaid spherical motor designs reported in literatures that of this magnetic design are PM motor. It is suitable for those motors with the magnetic poles fixed on the rotors. When this stator design is used for PM spherical motors, the pole-pitch matching is required. More research in this direction is needed to develop

the pole-pitch rule for spherical PM motor that resembles the pole-pitch rule for cylindrical PM motors.

Meshed windings for spherical motor

The last spherical motor design concept is the spherical motor realized by meshed windings.

As we have mentioned before, for a induction or hysteresis machine, a stator design with an uniform air gap and windings embedded in the slots is desired to improve motor efficiency and reduce torque ripple. This fact motivates us to think about such a stator design for spherical induction and hysteresis machines. A prior trial in this direction is the spherical motor with two degrees of freedoms reported by Dehez et al. in [41]. Figure 7-2 shows a diagram of the 2-DOF induction spherical motor they developed. In this design, a piece of induction stator segment with windings in two orthogonal directions is used to realize torque production about two axes. This spherical induction motor wins in its torque production ability: compared with the design of a motor uses only a combination of linear stator segments, it has a much larger effective surface area on rotor. In this thesis let us call this stator segment design as "meshed winding", namely, the windings that embedded in the stator slots forms a mesh, thus torque can be generated in multiple directions.

In Dehez's design, the spherical motor can only generate torque in two rotational directions. However, with meshed winding method, it is possible to design stators that can generate torques in all three directions and thus enable the spherical motor to become an all-DOF actuator. Figure 7-14 shows a diagram of a design concept of meshed winding spherical motor inspired by the design by Dehez. This spherical motor can be either induction type or hysteresis type. Figure (a) shows a piece of stator segment with meshed windings in three directions. When coils are distributed in the slots are energized, torques can be generated in three directions. With 8 of this stator segment placed surround a spherical motor at the sections shows in Figure (b), torques in the directions shown by the arrows can be generated.

A meshed winding motor enables the induction or hysteresis type spherical motor

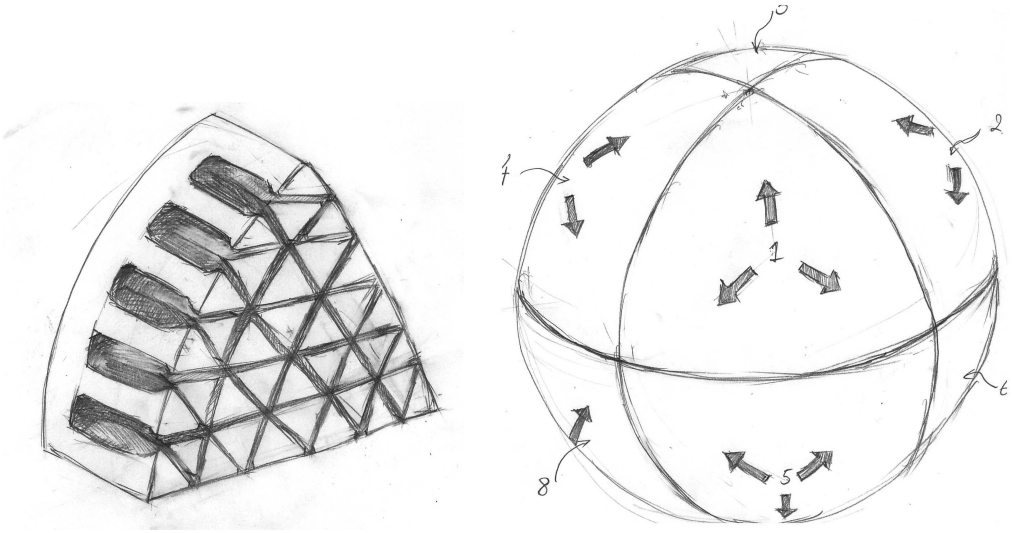

(a) (b)

Figure 7-14: A magnetic design concept for 3D spherical motor with distributed windings. (a) a stator segment with windings in the slots. (b) Positions to place the stator segments. The sphere is split into 8 quarters. With each of these positions placed a stator segment, torques in the directions shown by the arrows can be generated.

to have a larger effective rotor area for torque production than that implemented by a combination of linear stator segments. However, it requires a much more complicated stator structure, especially for stator core application, electrical steel laminations or powder material is needed to limit eddy current. Nowadays the 3D printing technology is growing in an amazing speed and now it already allows us to make parts of complicated geometries out of metal materials [44]. With the cost of manufacturing such a part keep reducing, we are looking forward to one day in the near future that this technology to enable much more flexible designs.

Out-runner spherical motor

In the world of single axis electric machines, there are many out-runner motors around, especially of permanent magnet type (or DC brushless). This type of motor spins its outer shell around its windings, and are widely used for many applications especially when direct drive is required, since they eliminate the extra weight, complexity, inefficiency and noise from a gearbox. Then a natural question to ask will be, is it

possible to generalize these advantages to spherical motors and thus design a spherical out-runner motor?

An out-runner spherical motor infinite moving range does not allow cable connections between outside and inside of the spherical rotor, this prevent it to be used for reaction sphere application. However, a spherical out-runner motor has many other special applications. One of them is the spherical rolling robot. This is an active research direction in the field of mobile robots due to its advantages of highly maneuverable, good collision recover ability, and adaption for multiple terrain. Besides, since they can be designed to be totally sealed, they are ideal for hazardous environments. Reference [45] gives a review on the recent progress on spherical mobile robots. However, to the best of our knowledge, there has no direct drive spherical robot being reported. An out-runner spherical motor of infinite moving range can be a great candidate for the drive for such a mobile robot.

If the out-runner spherical motor is designed to have a limited moving range, then connections between the inside and outside are allowed. This enables it to be used for many other applications such as robot joints.

Two design concepts for a out-runner spherical motor are presented in Figure 7-15 and 7-16. Figure 7-15 shows a spherical motor design uses a combination of linear motor segments for torque generation. Only a half of the rotor shell is drawn in this figure. If we have the stator side fixed to one link and the rotor shell is connected to another link, then this motor can be used for a robot joint, which can move in a certain range of angular positions. If it is used for an spherical motor with no limit on motion range, then the rotor need to be a full spherical shell. Of course, since no wired connections are allowed between inside and outside, all other systems, including controller, power electronics, sensors are needed to be placed inside.

Figure 7-16 shows a out-runner spherical motor that implemented by the design with distributed salient magnetic poles, where Figure (a) shows the stator design with 20 magnetic poles distributed evenly on a sphere, and Figure (b) shows the spherical shell shape rotor with magnetic poles on its surface.

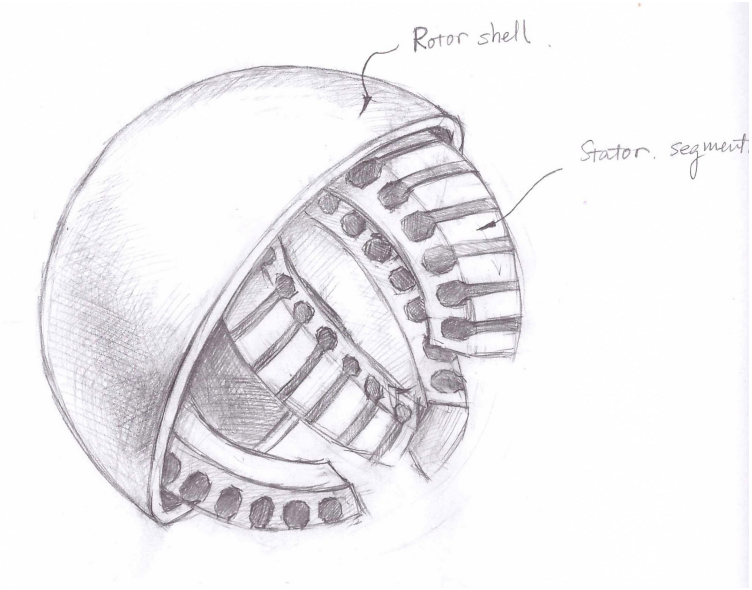

Figure 7-15: Outer runner spherical motor design.

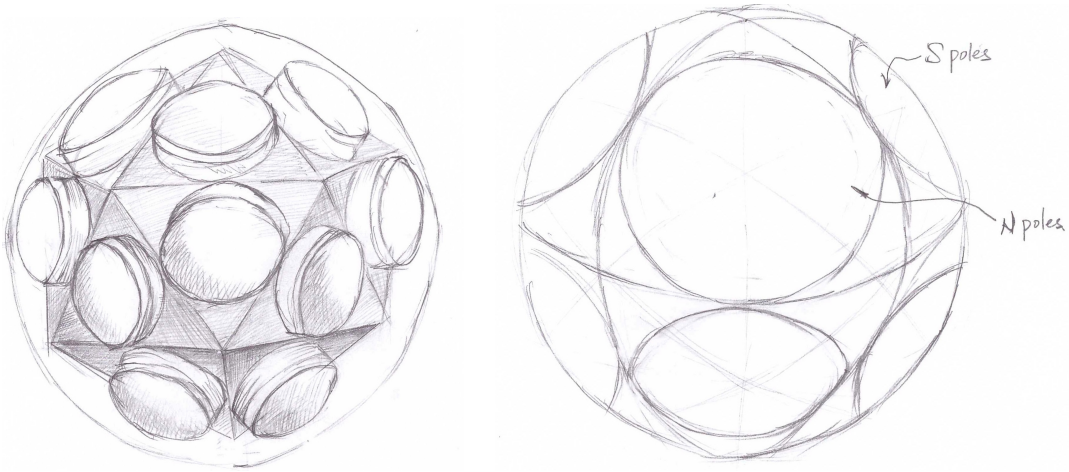

Figure 7-16: Outer runner spherical motor design.

7.3 Summary

This chapter summarizes our considerations and initial design concepts spherical motors for a three-axis reaction sphere. In this chapter, a literature review on the design of spherical motors is presented first. These motor designs can be classified into different into different types by its driving principles. After that, several motor driving principles are evaluated and a discussion about them for reaction sphere is presented. At last, several motor magnetic designs for spherical motors are presented. This study provides a basis for further explorations for the development of a high-speed magnetically suspended three-axis spherical motor for reaction sphere application.

Chapter 8

Conclusion and Future Work

8.1 Conclusion

In summary, this thesis provides preliminary research for a magnetically suspended reaction sphere driven by hysteresis machines. The primary contribution of this thesis include:

1. Designed, built, and tested a magnetically suspended reaction sphere with one-axis hysteresis drive (1D-MSRS) (Chapter 2).

2. Analyzed single degree-of-freedom magnetic suspension with PM flux biased actuator (Chapter 3).

3. Presented a complete analytical model for the bearing function for a bearingless motor. Designed control for reaction sphere's lateral suspension under all excitation conditions (Chapter 4).

4. Simulated motor operation of 1D-MSRS with a equivalent circuit model of hysteresis motor and verified simulation with 1D-MSRS test results (Chapter 5).

5. Developed a speed control method for hysteresis motors for hunting suppression and minimize speed rise time and demonstrated effectiveness in attenuating speed oscillation while increasing sphere's acceleration (Chapter 6).

6. Studied spherical motor design for reaction sphere application. Proposed several spherical design concepts (Chapter 7).

The tested performance of the 1D-MSRS are summarized and compared with the specifications of MW200 in Table 8.1.

Table 8.1: Specifications for MicroWheel 200 (MW200) Reaction Wheel from Microsat Systems Canada Inc.

Specification	MSCI MW200	1D-MSRS
Size	$100 \times 90 \times 90$ mm	$120 \times 120 \times 110$ mm
Mass	1.0 kg (assembly for one wheel)	0.63 kg (rotor)+0.42 kg (Stator + suspension electromagnet)
Imbalance	Static: < 0.2 mg.m; Dynamic: < 0.03 mg.m^2	zero due to rotor's spherical symmetry and magnetic suspension
Torque capacity	30 mNm	8.15 mNm
Angular momentum capacity	0.18 Nms	0.23 Nms (running synchronously at 150 Hz / 9000 rpm)
Motor power consumption	0 rpm: 3.0 W; average: 7 W;	Operating in steady state at 1800 rpm: 3.44 W

Data in Table 8.1 shows that that the torque capacity of 1D-MSRS is smaller than that of MW200 reaction wheel. The reasons, to our understanding, are threefold. First, hysteresis motors are not winning in their torque ability comparing to their permanent magnet motor counterparts. Second, D2 steel is not the best rotor material for hysteresis motors. We believe that if material with better hysteresis property is selected, higher torque can be achieved. Third, in the design of the 1D-MSRS, the effective surface area on the rotor for torque production is small.

Comparing with the baseline performance of MSCI MW200 reaction wheel, the 1D-MSRS demonstrated smaller imbalance and larger angular momentum capacity. In fact, the imbalance of the 1D-MSRS can achieve zero because the uniformity of rotor material and the spherical symmetry of rotor, and the improvement in momentum capacity is because the 1D-MSRS is running at higher speed. We believe that the sphere can reach a even higher synchronous speed when running in vacuum, where air drag can be eliminated. Besides, the 1D-MSRS demonstrated low motor power consumption when operating in steady state (here the power for weight compensation is not included). This is a direct result of magnetic suspension which eliminated mechanical frictions. The above comparisons demonstrated a good potential of hysteresis motors for high speed reaction spheres or reaction wheels' applications, especially when they are assisted with magnetic suspension.

8.2 Future works

Looking into the future, we outline here some suggested directions for future explorations.

8.2.1 3D magnetically suspended reaction sphere

The project presented in this thesis is a preliminary research for magnetically suspended reaction sphere in 3D, thus a natural future research path is the design for a 3D spherical motor with good performance. The discussion about motor driving principles and magnetic designs, as well as the potential challenges are discussed in

8.2.2 Magnetically suspended reaction wheel with hysteresis drives

In this thesis, we demonstrated that hysteresis motor based 1D-MSRS has a larger per-unit momentum storage, simpler rotor construction that allows higher rotation speed and lower vibrations compared with the commercial reaction wheels. One of the major limits of the hysteresis motor is its hunting dynamics. In this thesis, we presented one effective scheme to suppress this unfavorable dynamics. Based on these results, we believe that hysteresis motors have good potential for high-speed reaction wheels application, especially when they are assisted with magnetic bearings. More explorations into this direction may result in better solution for reaction wheels with larger momentum storage, smaller power consumption and less vibrations.

8.2.3 Better bearing and motor function combination design

In Chapter 4, we demonstrated that for bearingless motors, except for permanent magnet type, there is always a minimum current value in the motor windings in order to maintain the bearing function. As a result, the motor need a power dissipation even when no torque generation is needed. This fact makes the bearingless motor not very energy efficient in low torque operation, and thus makes it not suitable for spacecraft application where energy is expansive. To resolve this problem, better bearing and motor function combination designs are needed.

Bibliography

[1] Irene A Budianto and John R Olds. Design and deployment of a satellite constellation using collaborative optimization. *Journal of spacecraft and rockets*, 41(6):956–963, 2004.

[2] Bill Bialke. High fidelity mathematical modeling of reaction wheel performance. *Guidance and control 1998*, pages 483–496, 1998.

[3] Terry Marshall, Tracy Gunderman, and Fred Mobley. Reaction wheel control of the msx satellite. In *Guidance and Control 1991*, volume 1, pages 119–138, 1991.

[4] L Porter Davis, JF Wilson, RE Jewell, and JJ Roden. Hubble space telescope reaction wheel assembly vibration isolation system. *NASA Marshall Space Flight Center, Huntsville, Alabama*, 9, 1986.

[5] Toshio Fukada, Hidemi Hosokai, and Nobuyuki Yajima. Flexibility control of solar battery arrays: 3rd report vibration and attitude control with consideration of the dynamics of a reaction wheel as an actuator. *Bulletin of JSME*, 29(255):3121–3125, 1986.

[6] Mohammad Imani Nejad. *Self-bearing motor design & control.* PhD thesis, Mechanical Engineering, Massachusetts Institute of Technology, 2013.

[7] MicroWheel 200 (MW200) reaction wheel. Technical report, Microsat Systems Canada Inc., 2001.

[8] William H Isely. Magnetically supported and torqued momentum reaction sphere, US Patent 4,611,863, September 16 1986.

[9] K Kaneko, I Yamada, and K Itao. A spherical dc servo motor with three degrees of freedom. *Journal of dynamic systems, measurement, and control*, 111:398–402, 1989.

[10] George J Vachtsevanos and Kent R Davey. Spherical motor particularly adapted for robotics, US Patent 4,739,241, April 19 1988.

[11] Kok-Meng Lee, Hungsun Son, Jeffry Joni, et al. Concept development and design of a spherical wheel motor (swm). In *IEEE International Conference on Robotics and Automation*, volume 4, page 3652. IEEE; 1999, 2005.

[12] W Wang, J Wang, GW Jewell, and D Howe. Design and control of a novel spherical permanent magnet actuator with three degrees of freedom. *IEEE/ASME Transactions on Mechatronics*, 8(4):457–468, 2003.

[13] John Doty. Reaction sphere for spacecraft attitude control, wo 2010117819 a1, 2010.

[14] E Onillon, O Chételat, L Rossini, L Lisowski, S Droz, and J Moerschell. Reaction sphere for attitude control. In *Proc. 13th European Space Mechanisms and Tribology Symposium*, 2009.

[15] S Miyairi and T Kataoka. A basic equivalent circuit of the hysteresis motor. *Elect. Engng. Japan (USA)*, 85:41–50, 1965.

[16] Benjamin Richard Teare. Theory of hysteresis-motor torque. *Electrical Engineering*, 59(12):907–912, 1940.

[17] A Chiba, DT Power, and MA Rahman. Characteristics of a bearingless induction motor. *IEEE Transactions on Magnetics*, 27(6):5199–5201, 1991.

[18] Xiaodong Lu et al. *Electromagnetically-driven ultra-fast tool servos for diamond turning*. PhD thesis, Mechanical Engineering, Massachusetts Institute of Technology, 2005.

[19] PA12: A power operation amplifier. Technical report, Apex Microtechnologies, 2012.

[20] Herbert C Roters. *Electromagnetic devices*. Wiley, 1944.

[21] David Meeker. Finite element method magnetics (FEMM). Technical report, A Windows finite element solver for 2D and axisymmetric magnetic, electrostatic, heat flow, and current flow problems with graphical pre-and post-processors, 2006.

[22] David Lippincott Trumper. *Magnetic suspension techniques for precision motion control*. PhD thesis, Electrical Engineering and Computer Science, Massachusetts Institute of Technology, 1990.

[23] PK Hermann. A radial active magnetic bearing having a rotating drive. *London Patent*, 1(500):809, 1974.

[24] Akira Chiba, Tadashi Fukao, Osamu Ichikawa, Masahide Oshima, Masatugu Takemoto, and David G Dorrell. *Magnetic bearings and bearingless drives*. Elsevier, 2005.

[25] AE Fitzgerald, Charles Kingsley, and Stephen Umans. *Electric Machinery*. Ed, 1983.

[26] MA Copeland and GR Slemon. An analysis of the hysteresis motor i-analysis of the idealized machine. *IEEE Transactions on Power Apparatus and Systems*, 82(65):34–42, 1963.

[27] M Azizur Rahman. Analytical models for polyphase hysteresis motor. *IEEE Transactions on Power Apparatus and Systems*, (1):237–242, 1973.

[28] D O'Kelly. Theory and performance of solid-rotor induction and hysteresis machines. In *Proceedings of the Institution of Electrical Engineers*, volume 123, pages 421–428. IET, 1976.

[29] JJ Nitao, ET Scharlemann, and BA Kirkendall. Equivalent circuit modeling of hysteresis motors. Technical report, Lawrence Livermore National Laboratory (LLNL), Livermore, CA, 2009.

[30] *Magnetic hysteresis*. wiley, 1999.

[31] Arthur Earl Bryson. *Applied optimal control: optimization, estimation and control*. CRC Press, 1975.

[32] Masaaki Kumagai and Ralph L Hollis. Development and control of a three dof spherical induction motor. In *2013 IEEE International Conference on Robotics and Automation (ICRA)*, pages 1528–1533. IEEE, 2013.

[33] HyoYoung Kim, HyunChang Kim, and DaeGab Gweon. Magnetic field analysis of a vcm spherical actuator. *Sensors and Actuators A: Physical*, 195:38–49, 2013.

[34] Tomoaki Yano, Yoshiaki Kubota, Toru Shikayama, and Takeo Suzuki. Basic characteristics of a multi-pole spherical synchronous motor. In *Micro-NanoMechatronics and Human Science, 2007. MHS'07. International Symposium on*, pages 383–388. IEEE, 2007.

[35] Liang Yan, I-Ming Chen, and Chee Kian Lim. *Design, Modeling and Experiments of 3-DOF Electromagnetic Spherical Actuators*. Springer, 2011.

[36] Gregory S Chirikjian and David Stein. Kinematic design and commutation of a spherical stepper motor. *IEEE/ASME Transactions on Mechatronics*, 4(4):342–353, 1999.

[37] Kok-Meng Lee, Raye A Sosseh, and Zhiyong Wei. Effects of the torque model on the control of a vr spherical motor. *Control engineering practice*, 12(11):1437–1449, 2004.

[38] Shegeki Toyama, Shigeru Sugitani, Zhang Guoqiang, Yasutaro Miyatani, and Kazuto Nakamura. Multi degree of freedom spherical ultrasonic motor. In *Proceedings. 1995 IEEE International Conference on Robotics and Automation*, volume 3, pages 2935–2940. IEEE, 1995.

[39] Kent R Davey and George J Vachtsevanos. Spherical motor particularly adapted for robotics, US Patent 4,739,241, April 19 1988.

[40] Kent Davey, George Vachtsevanos, and Richard Powers. The analysis of fields and torques in spherical induction motors. *IEEE Transactions on Magnetics*, 23(1):273–282, 1987.

[41] Bruno Dehez, G Galary, D Grenier, and Benoît Raucent. Development of a spherical induction motor with two degrees of freedom. *IEEE Transactions on Magnetics*, 42(8):2077–2089, 2006.

[42] M Azizur Rahman. A permanent magnet hysteresis hybrid synchronous motor for electric vehicles. *IEEE Transactions on Industrial Electronics*, 44(1):46–53, 1997.

[43] NIKOLA TESLA. Electro-magnetic motor, US Patent 381,968, May 1 1888.

[44] Hod Lipson and Melba Kurman. *Fabricated: The new world of 3D printing*. John Wiley & Sons, 2013.

[45] Vincent A Crossley. A literature review on the design of spherical rolling robots. *IEEE Transactions on Magnetics*, 2006.